Direct Dark Matter Detection Phenomenology

by

Jayden L. Newstead

A Dissertation Presented in Partial Fulfillment
of the Requirements for the Degree
Doctor of Philosophy

Approved April 2016 by the
Graduate Supervisory Committee:

Lawrence M. Krauss, Chair
Richard Lebed
Cecilia Lunardini
Philip Mauskopf

ARIZONA STATE UNIVERSITY

May 2016

ABSTRACT

The identity and origin of dark matter is one of the more elusive mysteries in the fields of particle physics and cosmology. In the near future, direct dark matter detectors will offer a chance at observing dark matter non-gravitationally for the first time. In this thesis, formalisms are developed to analyze direct detection experiments and to quantify the extent to which properties of the dark matter can be determined. A range of non-standard assumptions about the dark matter are considered, including inelastic scattering, isospin violation and momentum dependent scattering. Bayesian inference is applied to realistic detector configurations to evaluate parameter estimation and model selection ability.

A complete set of simplified models for spin-0, spin-$\frac{1}{2}$ and spin-1 dark matter candidates are formulated. The corresponding non-relativistic operators are found, and are used to derive observational signals for the simplified models. The ability to discern these simplified models with direct detection experiments is demonstrated. In the near future direct dark matter detectors will be sensitive to coherent neutrino scattering, which will limit the discovery potential of these experiments. It was found that eleven of the fourteen non-relativistic operators considered produce signals distinct from coherent scattering, and thus the neutrino background does not greatly affect the discovery potential in these cases.

ACKNOWLEDGMENTS

A PhD is not carried out in a vacuum. I would like to acknowledge the many people who have contributed to it in their own way.

Firstly, I would like to thank my advisor and mentor Lawrence Krauss. Your guidance and ideas have given shape to my, dare I say, nascent career as a physicist. You have certainly prevented these years from being a dull part of my life. I also owe thanks to my committee members: Richard Lebed, Cecilia Lunardini and Philip Mauskopf. To Rich, I owe you a special thanks for your QFT class and subsequent discussions. I aspire to your level of rigor. Beyond my committee, a warm thank you goes to Tanmay Vachaspati for many discussions of physics over coffee.

The bulk of the content in this dissertation is formed from fruitful collaborations with others. I would like to thank James Dent, Subir Sabharwal, Russell TerBeek, Francesc Ferrer, Thomas Jacques, Louis Strigari and Bhaskar Dutta for their hard work and ideas. An especially deep thank you goes to my close collaborator and friend James Dent, I can only hope to achieve your level of productivity while remaining a dedicated father.

To my parents, Liz and Calvin, you cultivated my intellectual side and instilled in me the spirt of questioning. Mum, you always walked the line of being proud and encouraging, while not indulging me into complacency. I could not ask for a more kind and supportive mother. Dad, you always encouraged me to think big with your questions of clocks moving at near the speed of light. I now reap what the two of you have sowed.

These five years in a foreign city would surely have been less fun if it were not for the many friends who temporarily called it home. For the many beers (Hank, Jeff, Francis and Ryan), BBQ's (Hank and Bryce), scotches (Hank and Francis), hikes (Owen, Lauren, Jeff and *not* Hank), half marathons (Jeff and Owen) and distractions

in the office (Yao, Subir, Saugata and definitely Hank). I thank you all dearly, and I will look back on my time at ASU with fondness and warmth.

Lastly, to my wife Nadia, I cannot put into words all the ways in which you have contributed not only to this work, but to my life. We are each less than half of a greater whole. Together, I feel confident in tackling whatever life has to throw at us.

TABLE OF CONTENTS

Page

CHAPTER Page

CHAPTER Page

LIST OF TABLES

LIST OF FIGURES

Figure Page

Chapter 1

INTRODUCTION

The mystery of dark matter has vexed scientists for decades. While hints of a problem with missing mass were published as early as the 1930's, it wasn't until the 1970's that the existence of dark matter was firmly established. In the intervening forty years abundant evidence for dark matter and its non-baryonic origin has been accumulated. Yet we are still no closer to knowing exactly what the dark matter is made of. This dissertation studies and extends techniques for extracting properties of the dark matter from experiments performed on Earth.

The progress of our understanding of the universe has been one of ever-increasing humility. We inhabit an ordinary planet orbiting around a typical star, which is one of 200 billion in the Milky Way. Furthermore, the Milky Way is just one in billions of galaxies in an observable universe that is at least 45 billion light years across. While Immanuel Kant did correctly predict that galaxies were their own 'island universes' (distinct from the Milky Way) in the 18th century, in as late as the 20th century there was still serious debate whether the Milky Way was the only galaxy in the universe. Other galaxies were observable, but without powerful telescopes they were simply not recognized for what they were. It was not until 1929 that Edwin Hubble was able to calculate the distance to nearby galaxies by observing individual stars within them. Hubble found that the distances were far too great for the stars to be part of the Milky Way. Further observations by Hubble found that many galaxies were receding from us, with a velocity proportional to their distance from the Milky Way - a phenomenon now attributed to the expansion of the universe. This led to the idea that at some point in the distant past all galaxies must have been

at the same point in space - it appeared as though the universe had a beginning. This dense and hot beginning is known as the big bang, currently estimated to have occured 13.8 billion years ago. In 1964, Penzias and Wilson accidentally discovered the cosmic microwave background radiation (CMBR), the slowly-cooling remnant of the big bang. Follow-up observations of the CMBR found that its temperature is 2.73K and is almost perfectly isotropic, in conflict with the assumption that distant regions of the universe are not causally connected. This observation provides strong motivation for a period of rapid inflation in the very early universe. In the early 1990's the RELIKT and COBE satellites measured deviations from perfect isotropy at around one part per 10^5. Measuring the power spectrum of anisotropies in the CMBR enabled cosmology to become a precise science. This, however, led to some confusion, as these and other measurements conflicted with the infered age of the universe [1]. Then in 1998, groups led by Brain Schmidt and Saul Perlmutter used supernovae to observe the accelerated expansion of the universe [2, 3], proving the universe had a non-zero cosmological constant. Together these observations played a critical role in the formation of the standard cosmological model, ΛCDM (Lambda, the cosmological constant and CDM for cold dark matter). Currently, the state of the art measurements from the Planck satellite have determined that the universe is 68.5% dark energy, 26.5% dark matter and 5% baryonic matter [4].

Despite baryonic matter being the smallest component of the universe, it is the most well understood. The history of our understanding of ordinary matter is long, and initial attempts to explain how matter behaves were primitive. However, while describing matter with the four classical elements of antiquity (earth, air, fire and water) may have been naive, the underlying concept of reductionism has been remarkably successful. From there it was a small philosophical jump to atomism, though

experimental evidence would have to wait a few millenia. After Dalton explained chemical reactions in terms of atoms in the early 19th century, particle theory started to take off. Within 100 years, electrons, protons and neutrons were discovered. Further scrutiny revealed protons and neutrons were not fundamental, but instead made of complex states of quarks and gluons. It is unclear where this Russian-doll puzzle will end, but there is reason to believe that more discoveries await those who probe more deeply. The ability to probe the microscopic world is driven by access to higher energy scales. This access is owed to the technological development humanity has experienced throughout the last century, which has enabled scientists to undertake ambitious projects such as the Large Hadron Collider (LHC). In 2012 the ATLAS and CMS experiments at the LHC discovered the Higgs boson, predicted 40 years ago, completing the Standard Model of particle physics. While the Standard Model is the most precisely tested theory of nature, it does not explain dark matter or dark energy and so only describes a meager 5% of the universe.

1.1 Evidence for Dark Matter

The evidence for dark matter is only gravitational in nature, its presence inferred through indirect observations. The first such observation was made by Fritz Zwicky in the 1930's, who observed the Coma cluster of galaxies and found that the galaxies therein did not appear to obey the virial theorem. Zwicky hypothesized that there was 'dunkle materie' (dark matter) that made up the difference [5]. The precision of Zwicky's observations was low, and more robust evidence didn't come until 1970 when Vera Rubin and Ken Freeman measured rotation curves of galaxies [6, 7]. They found that gas moved faster at large radii than expected, Freeman remarked that additional mass, distributed very differently to visible mass, must therefore exist in

these galaxies. Further rotation curve measurements firmly established the existence of dark matter within all galaxies. To explain these observations, dark matter must be distributed in a large halo (many times the size of the disk) around galaxies and generally account for more than 50% of its total mass.

An alternative (but still gravitational) probe of the dark matter is through gravitational lensing. When a distant galaxy is lensed by an intervening cluster of galaxies, it is possible to get a measurement of the mass of the cluster. While this method comes with its own systematic errors, it provides an independent, alternative method to the virial method pioneered by Zwicky. It is found that around 85% of the mass of the galaxy clusters is in dark matter [8], this is higher than within galaxies, and is more representative of the universe as a whole. A striking example of the dominance of dark matter within clusters is the bullet cluster, shown in Fig. 1.1. The bullet cluster consists of two colliding galaxy clusters which are in the process of merging. Presently it can be observed that while much hot gas has collided, the majority of the mass in these clusters (due to dark matter) passed through the collision unaffected. This observation provides compelling evidence that the dark matter is non-baryonic and does not have an appreciable self-interation. Critics of the 'dissociative merger' interpretation of the bullet cluster point out that it is a sample size of one, and perhaps it could be explained by other means. Therefore a group, the Merging Cluster Collaboration, has begun searching for similar dissociative mergers and have currently identified seven more examples [9].

On the largest scales currently accessible to observation, the CMBR, the gravitational effects of the dark matter can also be observed. By the epoch of recombination, the dark matter had long since decoupled and started to collapse into a clumpy dis-

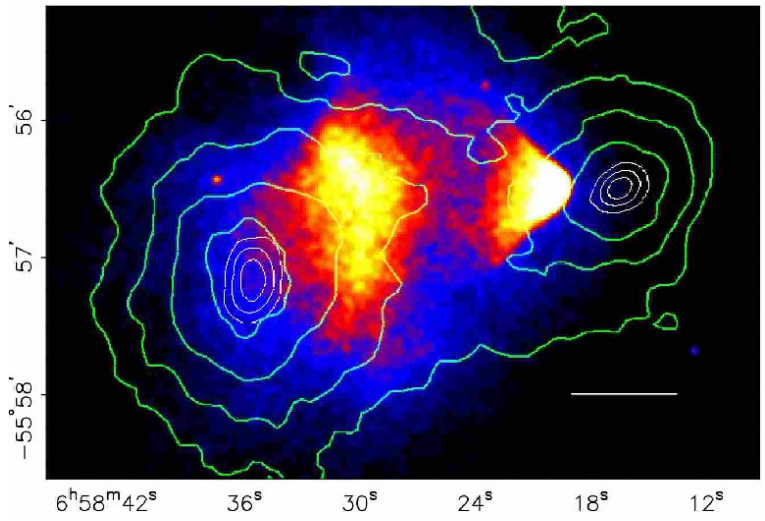

Figure 1.1: The bullet cluster, with the projected total mass shown in green contours (lensing data) and the plasma shown in color (x-ray data) [8].

tribution. At this point in the history of the universe the dark matter dominated the energy density and thus provided a significant gravitational potential background for the matter and radiation components of the energy density. The gravitational potential has 2 effects on the observed CMBR: first, it causes a modulation of the density of the plasma, and secondly, it provides a gravitational well out of which the photons of the CMBR must climb (known as the Sacks-Wolf effect). The net effect is that different regions of the universe become transparent at different times. Since this occurs on an expanding background, it leads to an increased cosmological red shift for areas with higher dark matter density. Given that the temperature of the photons decreases linearly with expansion/red-shift, the temperature of the CMBR changes slightly at different points on the sky. This was most recently illustrated by the Planck satellite, see Fig. 1.2. These effects dominate on larger angular scales, and so measuring the first few peaks of the power spectrum prodives a robust determination of the total dark matter content of the universe. In particular the relative heights of the first few peaks quantify the baryonic matter to dark matter ratio, which is in good agreement with results from big-bang nucleosynthesis.

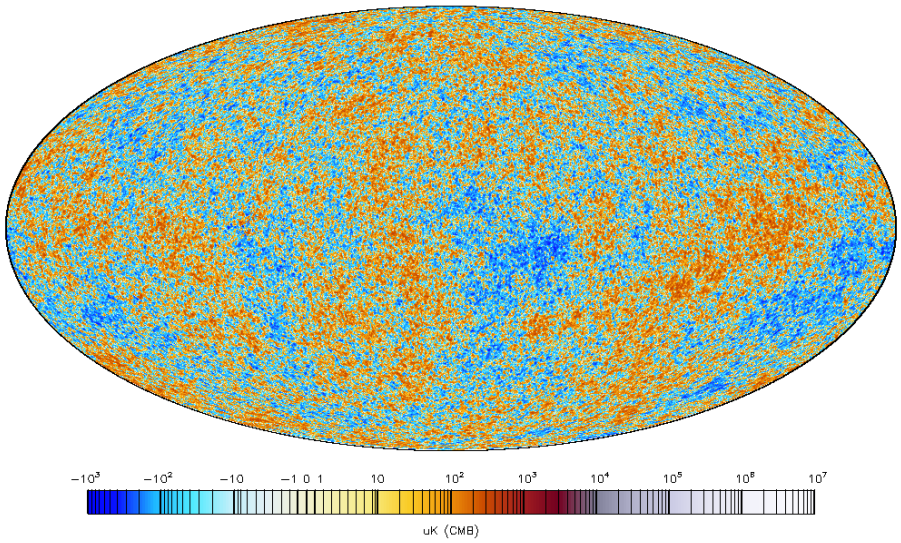

Figure 1.2: The CMBR sky, as observed by the Planck satellite, credit: ESA.

The above three observations probe the dark matter on three distinct scales, the galactic, inter-galactic, and cosmic scale. This is not a comprehensive list, but it highlights that the phenomena of missing, non-baryonic mass is independent of the scale being observed. Given the above observations, dark matter must be a stable and neutral particle (or have a very small charge). The only particles with these properties are the neutrinos. While neutrinos are appropriately elusive particles, their mass is too small to be the dark matter (current limits on the sum of neutrino masses are: $\Sigma m_{\nu_i} < 0.18$ eV [10]). Their low mass means that they are always relativistic, making them a poor candidate for (cold) dark matter. Therefore, new candidate particles have been proposed to explain the dark matter, for example, WIMPs (weakly interacting massive particles), axions, and sterile neutrinos. Each of these particles extend the Standard Model in different ways, while still reproducing the observed cosmic distribution of dark matter. This dissertation will focus on WIMP dark matter.

1.2 WIMP Dark Matter

A simple and compelling paradigm for the dark matter is that it consists of a weakly interacting massive particle (WIMP), which was thermally produced in the early universe. A sufficiently massive WIMP will have decoupled from the primoridal plasma, leaving behind a relic which we observe to be the dark matter. The abundance, n_t, of such a particle can be calculated from the Boltzmann equation in an expanding universe with Hubble constant H, giving

$$\frac{dn}{dt} = \langle \sigma v \rangle (n_{\rm eq}^2 - n^2) - 3Hn, \tag{1.1}$$

where $\langle \sigma v \rangle$ is the thermally averaged annihilation cross section. This equation is commonly written in terms of the entropy-weighted abundance $Y = \frac{n}{s}$, and inverse temperature $x = \frac{m}{T}$,

$$\frac{dY}{dx} = \frac{1}{3H}\frac{ds}{dx}\langle \sigma v \rangle (Y^2 - Y_{\rm eq}^2). \tag{1.2}$$

As the temperature of the universe decreases below the WIMP mass, Y_{eq} goes to zero. The abundance then sharply decreases as WIMPs continue to annihilate until there is only one WIMP per comoving volume. To find the relic abundance of WIMPs, the integration can be approximated, or performed numerically (e.g. Figure 1.3). The present day relic is then, as a fraction of the critial density,

$$\Omega_{\rm DM} h^2 = \frac{m s_0 Y_0 h^2}{\rho_0^{crit}} \sim 2.8 \times 10^8 Y_0 \frac{m}{\rm GeV}. \tag{1.3}$$

To obtain the observed abundance of dark matter ($\Omega_{\rm DM} h^2 = 0.11$ [4]) with a 50 GeV WIMP, the required cross section is

$$\langle \sigma v \rangle \sim 2.4 \times 10^{-23} {\rm cm}^2/{\rm s} \sim 0.1 c \frac{(\lambda/.1)^4 (m_x/50{\rm GeV})^2}{16\pi (M/500{\rm GeV})^4}. \tag{1.4}$$

Thus the scale of the interaction, M, must be of order the weak scale to reproduce the observed relic abundance. This coincidence is known as the WIMP miracle.

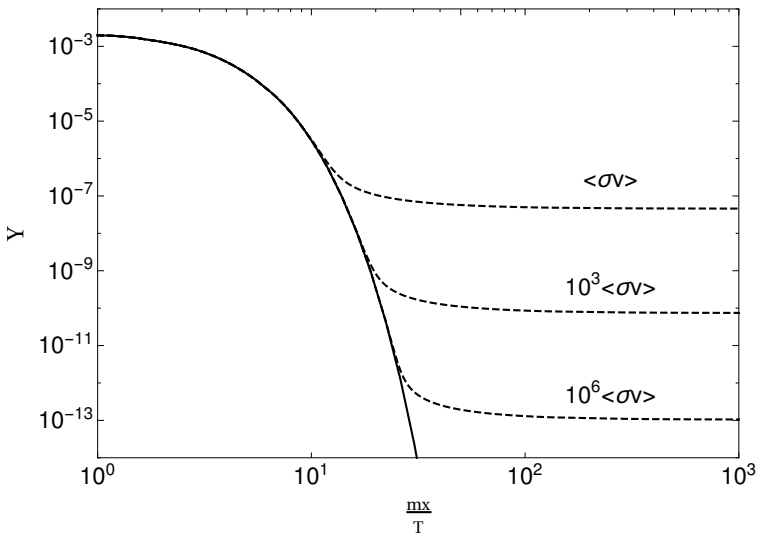

Figure 1.3: Numerical solution to Boltzmann equation for a WIMP of mass 50GeV, showing the decreasing particle abundance when the cross section is increased.

1.2.1 Dark Matter Experiments

To discern the nature of the observed dark matter, experiments must be conducted to detect it. Experimentalists have three avenues for probing the dark matter:

1. Create dark matter in an accelerator such as the Large Hadron Collider. Colliders are ideal for studying particle properties, but one must also confirm that the particle being created is the same particle responsible for the dark matter observed in the universe.

2. Detect a signature of dark matter decay or annihilation in the galactic halo. This method could provide a smoking gun signal, but two problems arise; dark matter may not annihilate or decay, and discerning a signal from the astrophysical background is difficult.

3. Exploit the flux of dark matter through the Earth by detecting nuclear recoils in a controlled environment. Such experiments are called 'direct detection' experiments and are the subject of this dissertation.

Of the three detection methods, the best chance at unambiguously discovering the particle nature of dark matter lies with direct detection. That said, each method has its own complementary strengths, and each can provide vital clues about the nature of the dark matter. For example: direct detection and collider searches are not very sensitive to WIMP-lepton interactions, while indirect detection searches remain unaffected. Alternatively, asymmetric dark matter models can greatly suppress indirect detection signals, but leave the direct detection and collider searches unaffected. Where one experiment has a blind spot, another may not; thus, having a thorough understanding of the complementarity of the various experimental approaches will be required to solve the dark matter puzzle.

1.2.2 Direct Detection of Dark Matter

In 1985 it was proposed that dark matter in the galactic halo could be detected by observing its interaction with the nucleus of an atom [11, 12]. There are three channels through which the nuclear recoils can be observed; phonon/heat production, scintillation light, or charges from ionization. Detectors often use two of the channels to help differentiate signal from background. Given that the local density and relative velocity of WIMPs is approximately 0.3 GeV/cm^3 and $\mathcal{O}$(200km/s), the flux of WIMPs is $\sim 6 \times 10^6 \left(\frac{1\text{GeV}}{m}\right)/\text{cm}^2/\text{s}$. Thus all material in this region of the galaxy is subjected to $\sim \frac{\sigma}{1\text{pb}}$ WIMP-nucleus collisions per kilogram per day. While in principle any material could be used to search for these nuclear recoils, in practice,

detector materials are limited to a small set of elements. As of 2016, the state-of-the-art detectors are made of liquid xenon (the Large Underground Xenon experiment, LUX [13]) or crystalline germanium (the Cryogenic Dark Matter Search, CDMS [14]). Xenon detectors typically use charge and light channels while germanium detectors make use of phonon and charge channels. Other detectors made from silicon, argon, sodium-iodide and fluorocarbons also exist, but are currently less sensitive.

Given the low signal event rate, the central challenge of direct detection experiments is the reduction of the background event rate, which limits their sensitivity. To this end, detectors are placed deep underground in naturally low radiation environments. For example, the Soudan mine in the USA houses the CDMS experiment[1], which is just over 2000mwe[2] underground. Given the practical length of an experiment is less than a decade, the limiting factor in sensitivity is the detector size. Detector technology has matured, and experiments such as Xenon-1t are currently scaling up their designs to have over a tonne of active mass. These detectors will be sensitive to a single WIMP interaction in a tonne of detector over the course of 3 months of operation [15]. This level of sensitivity is now approaching the level where a WIMP interacting with the SM through the higgs boson could now be discovered. This is an important milestone at the heart of the WIMP miracle.

Beyond discovering a signal of the dark matter in direct detection experiments, it is desirable to extract the properties of the particle responsible for it, e.g., its mass. The complexity of these experiments makes it hard to collect information about the

[1] which will soon be moved to the deeper SNOLAB mine in Canada.

[2] mwe = meters water equivalent, a unit which expresses the depth of water which provides the same level of shielding from cosmic rays.

nuclear recoils. Generally, only the amount of energy that the WIMP deposits in the detector is measured. Some detectors can measure directional information, but this comes at a cost of overall sensitivity, see for example DRIFT [16]. An additional complication comes from the velocity distribution of the WIMPs in the halo, which is not well constrained. Given that much of the information about the collision is unknown (incoming/outgoing WIMP velocity, scattering angle), the inverse problem of inferring WIMP properties from just the energy deposited is nontrivial. With the possibility of dark matter being discovered in the coming years, it is important to construct methods for extracting as much information as possible from any detection.

1.2.3 Outline

This thesis is based around three publications to which the author contributed significantly, each paper forming one of the following three chapters. Chapter 2 is based on [17], which contains a review of the standard formalism for analysing direct detection experiments. The goal of this paper was to explore the impact a ton-scale detector could have on measuring WIMP properties, under various assumptions of the underlying WIMP model. It was found that the more assumptions relaxed, the harder it was to extract WIMP properties. However, the addition of a second detector with a different target material is able to mitigate this. While the goal of this paper was to analyse WIMP scattering with minimal assumptions/model dependence, only spin-independent scattering was considered, which is a significant limitation of the study.

With the goal of providing a more general model-independent analysis of direct detection, the space of possible interactions needs to be expanded to include other forms of scattering beyond spin-independent. Given the recent appearance of nonrelativistic

effective field theory (NR-EFT) methods for direct detection [18], it was first desirable to know which operators were actually relevant to dark matter. Chapter 3 (based on [19]) provides a general analysis of direct detection experiments based on simplified models of dark matter. It was found that not all EFT operators could be generated, and thus these EFT's might be too general, i.e., they contain interactions which cannot be easily produced by UV-complete models. Additionally, experimental rates were calculated, and it was found that direct detection experiments can, in principle, distinguish certain interactions. However, it remains unclear how plausible this would be, using a realistic detector configuration.

Chapter 4 extends chapter 3 by applying a statistical formalism to quantify how discernable the simplified models actually are, the goal being to determine how many events are required to distinguish different interactions (and in turn how large a detector would need to be). As previously found in the literature, it was found that it is highly crucial to have more than one detector target to achieve distinguishabililty between interactions. Using two plausible future detector configurations, it was determined that $\mathcal{O}(1000)$ events are required for robust model selection.

Neutrino coherent scattering will provide an irreducible background to the next generation of direct detection experiments. This places a lower limit on the WIMP interaction strength which can be probed. However, if the WIMP interacts through non-standard interactions, it might be discernable from the neutrino background. Chapter 5 is based on [20], which explores the neutrino floor in the context of NR-EFT. Using the EFT interactions explored in chapters 3 and 4, we find that many operators will not suffer greatly from the neutrino background.

Finally, chapter 6 concludes and provides an outlook on the field of direct dark matter detection, with a discussion of future work.

Chapter 2

SCIENTIFIC REACH OF TON-SCALE DIRECT DARK MATTER DETECTION

2.1 Introduction

Weakly interacting massive particles (WIMPs), among the favored candidates for dark matter, have thus far not been conclusively detected in experiments sensitive to WIMP scattering with nuclei. A new generation of larger and more diverse detectors is under development, which motivates a consideration of the physics reach of these experiments in order to guide in their design, and also to focus on which uncertainties will be most significant in constraining the conclusions one may derive from any purported detection [21, 22, 23, 24, 25, 26, 27, 28, 29, 30]. As these detectors become more complex and more expensive, the biggest design effort should reside in ensuring that astrophysical and particle physics degeneracies that will confuse the interpretation of any signal observed by the detectors are reduced as much as possible. What is required is a realistic, comprehensive numerical tool to model the detectors and the relevant physics, and one which can be easily modified as design parameters develop and new astrophysical and particle physics constraints evolve. We have recently set out to complete such a task.

The DARWIN (DARk matter search WIth Noble liquids) project involves a proposed multi-ton detector, based on noble-liquid time projection chamber technology that has been demonstrated with xenon [31] and argon targets [32]. These are complementary targets, since they are well separated in atomic mass, leading to peak sensitivities at different dark matter masses. (For an in-depth description of the DARWIN detector see [33, 34, 35]). While the effect of complementarity has been studied for

a number of target combinations [22, 23, 24, 25, 27, 28], DARWIN is currently the furthest developed proposal for a direct detection experiment with multiple targets. In this paper we report on the results obtained from the development of a numerical tool that allows a rapid exploration of proposed signals using the most up to date particle physics constraints, astrophysical constraints, and background data, including possible isospin violation, inelastic interactions (in the WIMP sector), different dark matter phase space estimates, and solar neutrino and other detector backgrounds. We explore degeneracies between different sources of confusion, and point out which areas of experimental and theoretical investigation are likely to be most fruitful if one wants to best exploit co-located detectors containing different noble liquids.

We find that for WIMP masses less than around 200 GeV, the use of two targets can reduce mass and cross section degeneracies and enhance discrimination in the mass-cross section plane, relative to increasing the exposure of either individual target, in agreement with [22].

2.2 Particle Physics and Astrophysics Inputs

2.2.1 General Formalism

The primary quantity of interest in direct detection experiments is the differential event rate. In our initial analysis we will focus on WIMPs with spin-independent interactions, in part for simplicity and in part to connect with most of the previous detector development literature, which has focused on this scenario. In a future work we will extend this analysis to include the impact of possible spin dependence (see for example [36, 37, 38, 39, 40]) upon the physics reach of DARWIN and similar detectors.

With respect to the recoil energy E_R, the differential rate per nuclei per unit time is

$$\frac{dR}{dE_R} = \frac{\rho_\chi}{m_\chi m_N} \int_{|\mathbf{v}|>v_{min}} |\mathbf{v}| f(\mathbf{v}) \frac{d\sigma}{dE_R} d^3\mathbf{v}, \tag{2.1}$$

where ρ_χ is the local dark matter density, and m_χ, m_N are the WIMP and nucleus masses, respectively. The integral averages over the velocity distribution of WIMPs, $f(\mathbf{v})$, weighted by the differential cross section $\frac{d\sigma}{dE_R}$. Kinematically the minimum velocity, v_{min}, that can contribute to a recoil of energy E_R is [25]

$$v_{min} = \frac{1}{\sqrt{2E_R m_N}} \left(\frac{E_R m_N}{\mu_{\chi N}} + \delta \right), \tag{2.2}$$

where $\mu_{\chi N}$ is the WIMP-nucleus reduced mass and δ is an inelastic scattering parameter ($\delta = 0$ recovers the elastic case). (We note that inelastic scattering is not a property of most WIMP models, but this possibility has been raised [41], and thus we include it here for completeness.) While we are interested in the energy spectrum of the recoils, the full rate can be obtained by integrating this over the range of recoil energies that the detector is sensitive to. The standard approach is to write the cross section in terms of the WIMP-nucleon cross section at zero momentum transfer, σ_0, and the nuclear form factor, $F^2(E_R)$,

$$\frac{d\sigma}{dE_R} = \frac{m_N}{2v^2 \mu_{\chi N}^2} \sigma_0 F^2(E_R). \tag{2.3}$$

The WIMP-nucleon cross section can be written in terms of contributions from neutron and proton scattering, $\sigma_0 = \frac{4\mu_{\chi N}^2}{\pi}[Z f_p + (A-Z) f_n]^2$, where A and Z are the atomic mass and number of the detector material, $\sigma_{\chi n} = \frac{4\mu_{\chi n}^2}{\pi} f_n^2$ and $\sigma_{\chi p} = \frac{4\mu_{\chi p}^2}{\pi} f_p^2$. Setting the proton and neutron masses to be equal, an appropriate approximation at the level of accuracy of relevance here, allows one to write $\sigma_{\chi n} = \left(\frac{f_n}{f_p}\right)^2 \sigma_{\chi p}$, such that the factor $\frac{f_n}{f_p}$ neatly incorporates isospin violating interactions. Eq. 2.1 then becomes

$$\frac{dR}{dE_R} = \frac{\sigma_{\chi p}}{2 m_\chi \mu_{\chi p}^2} \left(Z + \frac{f_n}{f_p} (A - Z) \right)^2 F^2(E_R) \mathcal{G}(v_{min}), \tag{2.4}$$

where we have defined

$$\mathcal{G}(v_{min}) = \rho_\chi \int_{|\mathbf{v}|>v_{min}} \frac{f(\mathbf{v})}{|\mathbf{v}|}\, d^3\mathbf{v}. \tag{2.5}$$

Using this formalism, the astrophysical and particle physics/nuclear physics inputs are each contained in separate terms, allowing us to examine each in turn.

2.2.2 Particle and Nuclear Physics Parameters

Isospin and Inelasticity

We have assumed here a simple spin-independent scattering amplitude which means that at low energy the scattering cross section on a nucleus is a simple constant times some product of nuclear charges squared. While this simplifies the analysis greatly there nevertheless remain two important unknowns related to the specific particle physics parameters of the WIMP sector. The first involves the WIMP couplings to different quarks, which at low energies gets translated into possible isospin violations in the WIMP scattering cross section. The second involves the (at present, less generic) scenario of excitations in the WIMP sector, which would produce possible inelasticity in the WIMP cross section, parameterized by the quantity δ mentioned earlier. When the isospin factor is not unity or the inelastic parameter is non-zero, the spectrum is modified, as shown in Fig. 2.1. The isospin factor only affects the magnitude of the recoil rate, while the inelastic parameter severely modifies the shape of the recoil spectrum, as can be seen from Eq. 2.4. The result is that experiments sensitive to the shape of the recoil spectrum are able to determine the value of the inelastic parameter but not the isospin factor, which therefore suffers a degeneracy with the cross section.

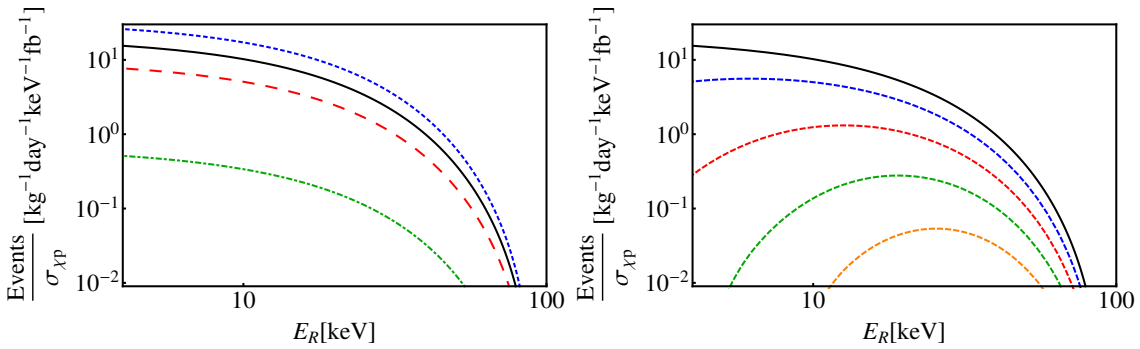

Figure 2.1: The differential event rate per femtobarn of cross section for various values of the isospin violating factor (*left*) and the inelastic parameter (*right*), for a WIMP with $m_\chi = 100$ GeV in a Xenon target, compared to a benchmark WIMP model with the same mass (solid line). A Maxwell-Boltzmann phase-space distribution and the Helm form factor have been assumed (see later sections). *Left:* From top to bottom, $f_n/f_p = \{1.5, 1, 0.5, -1\}$. *Right:* From top to bottom, $\delta = \{0, 25, 50, 75, 100\}$ keV.

Form Factors

The nuclear form factor encodes the energy dependence of the WIMP-proton cross section, allowing us to derive limits on the cross section at zero momentum transfer. In the lowest order Born approximation, the form factor is the Fourier transform of the nuclear mass distribution. Approximating the nuclei as spherically symmetric we have

$$F(q) = \int_0^\infty \rho(r) \frac{\sin(qr)}{qr} 4\pi r^2 dr, \tag{2.6}$$

where q is the momentum transfer. The mass distribution of nuclei is not well known, and instead it is generally assumed that the nuclei's mass distribution is approximately the same as its charge-distribution. The most commonly used fits to the charge distribution are the two and the three parameter Fermi distributions (2PF/3PF),

$$\rho_{\text{2PF}}(r) = \frac{1}{1 + \exp(\frac{r-c}{z})}, \tag{2.7}$$

$$\rho_{\text{3PF}}(r) = \frac{1 + w\frac{r^2}{c^2}}{1 + \exp(\frac{r-c}{z})}, \tag{2.8}$$

where the normalization is obtained by requiring $F(q=0)=1$. Unfortunately these distributions do not have analytic Fourier transforms. Instead it is common to use the analytic Helm form factor, obtained by convolving a constant, spherical charge distribution with a 'fuzzy' skin. The Helm form factor is given by [42]

$$F(q) = 3\frac{\sin(qr_n) - qr_n\cos(qr_n)}{(qr_n)^3}\exp\left[\frac{-(qs)^2}{2}\right], \tag{2.9}$$

where the skin thickness $s \approx 0.9$ fm and we use [43]

$$r_n^2 = \left((1.23A^{1/3} - 0.6)^2 + \frac{7}{3}\pi^2(0.52)^2 - 5\left(\frac{s}{\text{fm}}\right)^2\right)\text{fm}^2. \tag{2.10}$$

Using the parameters given in Table 2.1, the 2PF and 3PF form factors for argon and xenon are compared with the Helm form factor in Fig. 2.2. Given the agreement of the form factors over the relevant WIMP search region of both detectors, we can choose to use the Helm form factor with minimal loss of precision. Furthermore, it has been shown that small deformations from the assumption of spherical symmetry of the nucleus do not cause any substantial changes to the form factor at low energies [44, 45].

Table 2.1: Parameters for the charge distributions of argon and xenon

	2PF	3PF
^{40}Ar [46]	$c = 3.53$ fm $z = 0.542$ fm	$c = 3.73 \pm 0.05$ fm $z = 0.62 \pm 0.01$ fm $w = -0.19 \pm 0.04$ fm
^{132}Xe [47, 48]	$c = 3.646$ fm $z = 0.523$ fm	$c = 5.487$ fm $z = 0.557$ fm $w = 0.219$ fm

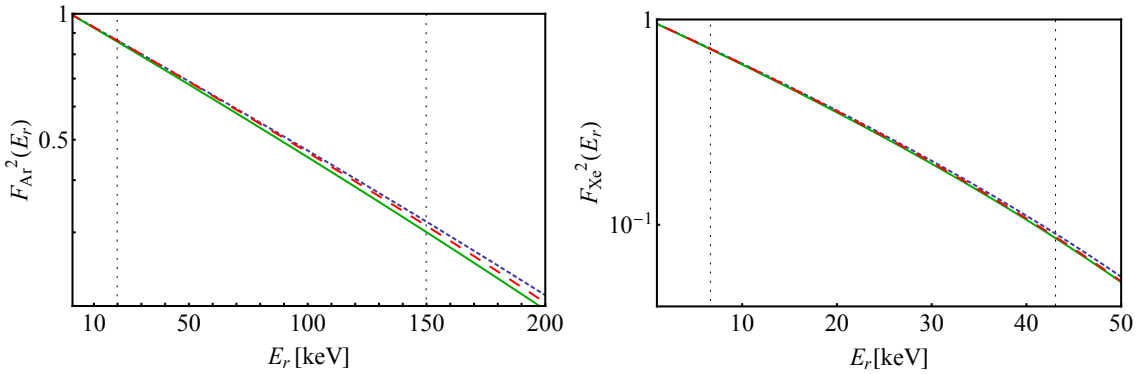

Figure 2.2: The Helm (red, dashed), 2PF (blue, fine dashed) and 3PF (green, solid) form factors for *left:* argon-40 *right:* xenon-132 over the energy range relevant to WIMP scattering. The vertical lines show the WIMP search region for each detector.

2.2.3 Astrophysical Parameters: Dark Matter Phase Space Considerations

The velocity distribution of the WIMPs in the galactic halo is a large source of uncertainty in the calculation of the differential event rate [49, 50, 51, 52, 53]. Fortunately, while significant uncertainties still remain, there has been significant progress coming from both observational and numerical studies of dark matter in our galaxy.

In considering the impact of the WIMP velocity distribution in the halo on the differential recoil spectrum, we must first transform into the rest frame of the Earth to find the local DM velocity $\mathbf{v}$,

$$\mathbf{v} = \mathbf{v}' - \mathbf{v}_e = \mathbf{v}' - (\mathbf{v}_0 + \mathbf{v}_\odot + \mathbf{v}_\oplus), \tag{2.11}$$

where $\mathbf{v}'$ is the DM velocity in the Galactic rest frame, and the Earth's velocity $\mathbf{v}_e$ is made up of the galactic rotational velocity, $\mathbf{v}_0$, the Sun's peculiar velocity, $\mathbf{v}_\odot$, and the Earth's orbital velocity about the sun, $\mathbf{v}_\oplus$. The small annual modulation due to $\mathbf{v}_\oplus$ is not considered in this work, and the Sun's peculiar velocity is taken to be $\mathbf{v}_\odot = (10.0, 5.23, 7.17)$ km/s [54], where the direction of the three elements of the vector are radially inwards towards the center of the galaxy, in the direction of v_0,

and upwards from the plane of the galaxy respectively. The choice of v_0 is discussed at the end of this subsection.

The standard halo model assumes a singular isothermal sphere of WIMPs, corresponding to a Maxwell-Boltzmann (MB) distribution of velocities,

$$f_{\rm MB}(\mathbf{v}') = \frac{1}{v_0^3 \pi^{3/2}} \exp\left[-\frac{\mathbf{v}'.\mathbf{v}'}{v_0^2}\right]. \tag{2.12}$$

While the singular isothermal sphere is not a good fit to the galactic density profile, the MB velocity distribution actually leads to somewhat conservative predictions [55]. The advantage of using the MB distribution is that it has an analytical solution to the integral in Eq. 2.5. After converting the integral into an integral of the MB distribution over the speed $v \equiv |\mathbf{v}|$ and the angle between $\mathbf{v}$ and $\mathbf{v}_e$, θ, one finds

$$\begin{aligned} \int \tfrac{f(\mathbf{v})}{|\mathbf{v}|} d^3\mathbf{v} = \int_{v_{min}}^{v_{max}} \int_{-1}^{1} 2\pi v f(v, \cos\theta) d\cos\theta dv = \\ \tfrac{1}{2v_e}\left(\mathrm{erf}(\tfrac{v_e - v_{min}}{v_0}) + \mathrm{erf}(\tfrac{v_e + v_{min}}{v_0}) - \mathrm{erf}(\tfrac{v_e - v_{max}}{v_0}) - \mathrm{erf}(\tfrac{v_e + v_{max}}{v_0})\right), \end{aligned} \tag{2.13}$$

where v_{esc} is the galactic escape velocity at the Earth's position. Formally we should truncate the distribution at v_{esc} in the galactic frame before integrating, but setting $v_{max} = v_{esc} + v_e$, the above formula is accurate to a few parts per million.

More realistic velocity distributions can be obtained if one assumes a spherically symmetric spatial distribution and isotropic velocity dispersion of WIMPs in the galactic halo. Specifically, we consider the Hernquist [56], Navarro, Frenk and White (NFW) [57], Burkert [58] and Einasto [59, 60] profiles. The NFW profile became the canonical profile for some time, and we include it for direct comparison with the literature. The Einasto profile is similar to the NFW at large radii, but avoids the large central cusp at the Galactic center. The Burkert profile is believed to provide a good description of the DM density profile in dwarf galaxies, and the Hernquist profile has the advantage of an analytic formula for the DM phase-space distribution, as we shall describe shortly.

In the case of a spherically symmetric velocity dispersion, the velocity distribution can be determined from the gravitational potential according to Eddington's formula [61],

$$F_h(\mathcal{E}) = \frac{1}{\sqrt{8}\pi^2}\left(\int_0^{\mathcal{E}} \frac{d^2\rho_\chi(r)}{d\Psi^2}\frac{d\Psi}{\sqrt{\mathcal{E}-\Psi}} + \frac{1}{\sqrt{\mathcal{E}}}\left(\frac{d\rho_\chi(r)}{d\Psi}\right)_{\Psi=0}\right). \tag{2.14}$$

Here the relative potential $\Psi(r)$ and the relative energy $\mathcal{E}$ are defined as

$$\Psi(r) = -\Phi(r) \text{ and} \tag{2.15}$$

$$\mathcal{E} = -E = \Psi(r) - E_k, \tag{2.16}$$

where Φ is the gravitational potential, and E and E_k are the total and kinetic energy respectively. The gravitational potential Φ can be found from Poisson's equation using any of the density profiles we consider. While Φ is the total gravitational potential, we neglect the effect of baryons, as their effect on the evolution of the DM density is unsettled; See e.g. Kuhlen et al. (2013) [62] and references therein. We plan to investigate this effect in a future work. Seeking to determine the local dark matter density, Catena and Ullio [51] used a Bayesian approach to constrain the 7 (8 for Einasto) parameters needed to model the Milky Way. These parameters are: our distance from the center of the galaxy; two dark matter halo parameters (the virial mass and a dimensionless virial scale, plus a halo profile shape parameter for Einasto); three baryonic parameters; and a parameter to encode the anisotropy of halo stars (see Ref. [51] for definitions). The analytic phase-space distribution for the Hernquist profile can be obtained using Eq. 2.14 in combination with the density profile and potential,

$$\rho_H(r) = \frac{M_{\rm MW}a}{2\pi r(r+a)^3}, \tag{2.17}$$

$$a = \frac{\sqrt{G_N\, M_{\rm MW} R_0} - R_0 v_0}{v_0}, \tag{2.18}$$

$$\Phi = -\frac{G_N\, M_{\rm MW}}{r + a}, \tag{2.19}$$

where R_0 is the distance from the Sun to the center of the Galaxy and M_{MW} is the mass of the Milky Way, giving [56]

$$f(q) = \frac{(8q^4 - 8q^2 - 3)\, q\sqrt{1-q^2}\,(1-2q^2) + 3\sin^{-1}(q)}{(1-q^2)^{5/2}}, \tag{2.20}$$

$$q = \sqrt{\frac{a\epsilon}{G_N\, M_{\rm MW}}}, \tag{2.21}$$

$$\epsilon = \frac{G_N\, M_{\rm MW}}{a + R_0} - \frac{1}{2}\left(\mathbf{v}'.\mathbf{v}'\right). \tag{2.22}$$

We adopt a value of $v_0/R_0 = 29.45$ km/s/kpc [63]. M_{MW} is determined from ρ_χ and v_0 following the technique in Hernquist (1990) [56]. Finally, while the effect of microhalos on direct detection experiments has been shown to be minimal [64], N-body simulations of galactic halos do show a departure on small scales from the standard smooth isothermal model. Thus, we also consider here the results of the Via Lactea numerical simulation [49], for comparison with the analytic model estimates.

For an illustrative comparison of how uncertainties in these distributions affect the WIMP scattering rate, each of the distributions is integrated by Eq. 2.5 and the results are shown in Fig. 2.3 and Fig. 2.4. The MB, Herquist and Via Lactea distributions use the standard astrophysical assumptions of $v_0 = 220 \pm 20$ km s^{-1}, $v_{esc} = 544^{+64}_{-46}$ km/s[1] and $\rho_\chi = 0.3 \pm 0.1$ GeV/cm^2 [65]. Note that there is considerable variation in the favoured values of v_0 and ρ_χ (see [66, 67, 65]). The large uncertainties we adopt cover most of the proposed range of these parameters. Also note that other halo models are designed to more accurately model the details of the data and thus have a smaller range of quoted uncertainties in the phase space distribution.

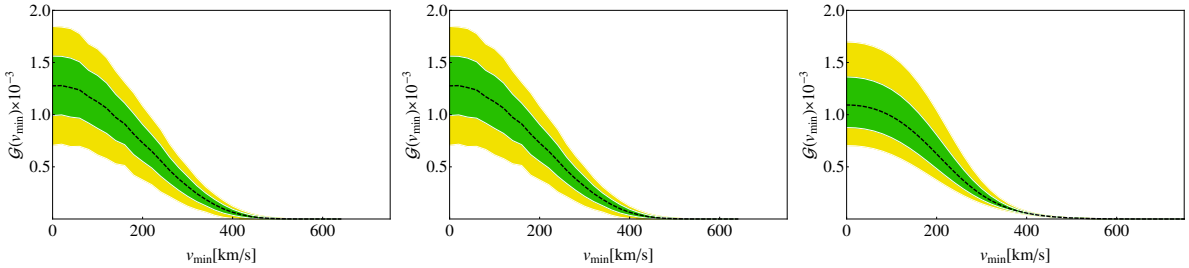

Figure 2.3: Numerical results of Eq. 2.5 for, from left: MB, Hernquist and Via Lactea profiles. The black dashed curve shows the mean value, while the green and yellow regions show one- and two-sigma errors. Note the errors here are larger than in Fig. 2.4 since only v_0, ρ_χ and v_{esc} (and for Hernquist, R_0, distance to center of the galaxy) are used to constrain these models.

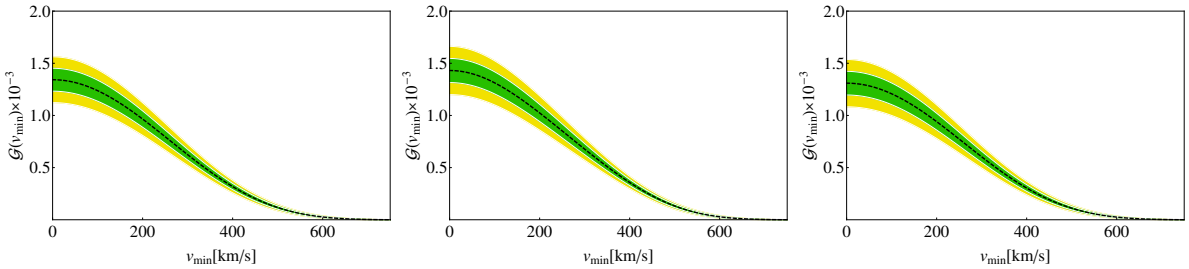

Figure 2.4: Numerical results of Eq. 2.5 for each of the velocity distributions from [51]. From left: NFW, Burkert and Einasto profiles. The black dashed curve shows the mean value, while the yellow and green regions show one- and two-sigma errors.

2.2.4 Backgrounds

Ultimately, it is the background rate that sets the lower limit of observable signal rates, so that significant attention must be paid to both shielding the detector from unwanted radioactive backgrounds, and also to devising methods to distinguish between possible signal and background events, in particular to distinguish candidate WIMP events which involve single scatter nuclear recoils from multiple scatter nuclear events and electronic recoils.

The XENON100 detector was able to achieve a pre-discrimination background rate of 5.3×10^{-3} dru (events/kg/day/keV$_{\text{n.r.}}$) [31]. For the future xenon component of the DARWIN detector and argon DarkSide-50 detector, the pre-discrimination electronic background goal is 10^{-6} dru (not including the solar neutrino background)

and $\mathcal{O}(1)$ dru respectively. In both cases the background is assumed to be constant in energy, and the radioactive nuclear recoil background is subdominant.

Liquid scintillators discriminate nuclear and electronic recoils via prompt vs. delayed signal cuts and/or pulse shape analysis. While the electronic recoil background in argon detectors is currently much larger, electronic recoils in argon can be discriminated at a rate of 1 part in 10^7 [32], compared with 2.5 parts in 10^3 for xenon. To provide a coincident detection and maximize complementarity, the argon detector must be as sensitive as the xenon detector, requiring a factor of 100 reduction in the argon background, which could be achieved through the use of low radioactivity argon [68].

Beyond intrinsic detector backgrounds, there is one ultimate background that is irremovable, and puts a lower limit on the scattering cross section sensitivity of WIMP dark matter detection experiments of the type considered here. This is the solar neutrino background, which comes in at a level of $\sigma = 10^{-48}\text{cm}^2$. In particular, elastic scattering of solar pp-neutrinos from electrons provides a flat background which cannot be feasibly screened. While electronic recoils can be discriminated and rejected, at some level, below that level the remaining spectrum (see Fig. 2.5) is irreducible. This corresponds to a rate of 1.8×10^{-4} events/tonne/day in the xenon WIMP search region [35]. To obtain a rate for argon detectors one must scale the xenon spectrum by $\frac{Z_{Ar}A_{Xe}}{Z_{Xe}A_{Ar}} = 1.096$. Due to the considerations described in the previous paragraph, however, this will be a sub-dominant component of the background in argon.

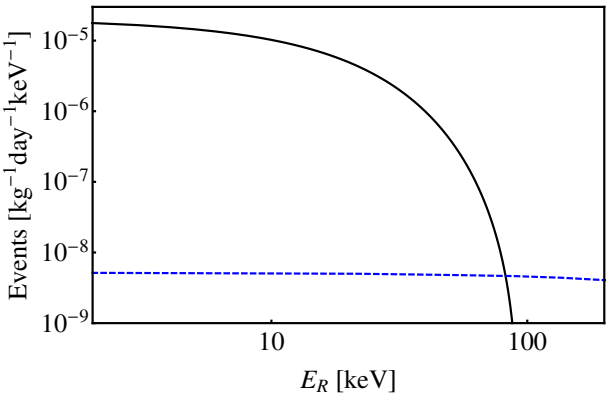

Figure 2.5: The differential event rate in a xenon detector for a 100GeV WIMP with $\sigma_{\chi p} = 3 \times 10^{-46}$ cm^2 using standard astrophysical assumptions (black solid) and the irreducible (after 99.75% rejection) neutrino backgrounds (blue dashed) [35]

2.3 Projected Sensitivity

2.3.1 Projected Experimental Upper Limits

To estimate the sensitivity of future experiments we construct 90% exclusion limits using the profile likelihood method on a representative 'Asimov' dataset [69, 70]. This method utilizes the test statistic,

$$q_\sigma = \begin{cases} -2\log(\lambda(\sigma)) & \sigma \geq \hat{\sigma} \\ 0 & \sigma < \hat{\sigma} \end{cases}$$

where λ is the profile likelihood ratio,

$$\lambda(\sigma) = \frac{\mathcal{L}(\sigma, \hat{\hat{\theta}})}{\mathcal{L}(\hat{\sigma}, \hat{\theta})}. \tag{2.23}$$

Here θ represents all of the uncertain parameters that enter the likelihood, $\hat{\sigma}$ and $\hat{\theta}$ denote that the likelihood has been maximized with respect to those parameters and $\hat{\hat{\theta}}$ denotes the likelihood has been maximized for the given σ. The likelihood function is a product of the probabilities of having observed A_i events, given the expected E_i events, for a given energy bin,

$$\mathcal{L}(\sigma, \theta) = \prod_{i=1}^{N} P(E_i(\sigma, \theta), A_i). \tag{2.24}$$

Table 2.2: These detector parameters are motivated by current experiments and expected performance of future detectors [32, 71, 72]. The backgrounds are assumed to be constant in energy.

	Xenon	Argon
Nuclear recoil acceptance	40%	50% at 35keV, 100% >60 keV
Total background (post-discrim.)	6×10^{-9} dru	2.3×10^{-9} dru
WIMP search region	6.6-43 keV	20-150 keV

The expected number of events E_i is the sum of both the expected DM recoil events and the background events in that energy bin. We define the WIMP search regions to be 6.6-43 keV for xenon and 20-150 keV for argon; the regions are split up into bins of width 5 keV (in lieu of smearing). The detector parameters are summarized in Table 2.2.

Typically, the XENON collaboration expose their detector for the length of time expected to produce single background event [31]. With this in mind, the solar neutrino background limits exposure to around 10 tonne-years in xenon. The limits obtained for several exposures of xenon and argon compared to the final XENON100 limits are shown in Fig. 2.6 (left). Note that to achieve comparable sensitivity, a larger fiducial volume of argon is necessary compared with xenon. Unless the neutrino background can be unambiguously subtracted or otherwise discriminated (e.g. via the use of directional information as described in [73]), these limits approximately represent the floor to the sensitivity of the current xenon liquid scintillator design. Fig. 2.6 (center and right) shows the effect of the uncertainty of the phase-space density on a 10 tonne-years xenon exposure. The NFW, Einasto and Burkert profiles enforce more stringent limits because they favor a local WIMP density of $\rho_\chi = 0.4$ GeV cm^{-3} [51]. Thus the standard MB assumptions are conservative in comparison to these more realistic profiles.

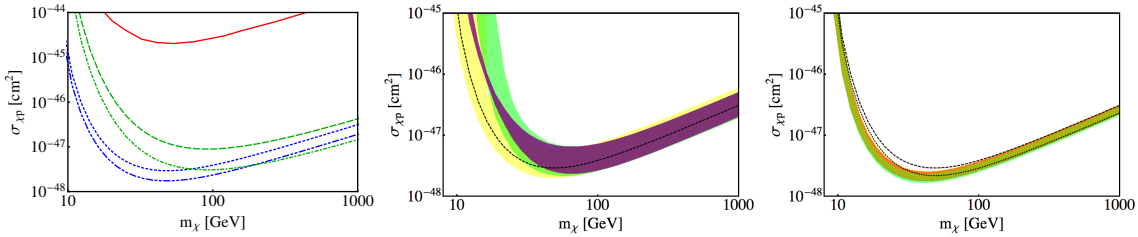

Figure 2.6: *Left:* comparison of exclusion limits for a 10 (blue, dotted) and 20 (blue, dot-dot-dashed) tonne-years xenon exposure, 20 (green, dashed) and 30 (green, dot-dashed) tonne-years argon exposure, and the current best limits set by XENON100 (red, solid) [31] (standard astrophysical assumptions). *Center:* the effect of astrophysical uncertainties on a 10 tonne-years xenon exposure with neutrino-only backgrounds for different WIMP halo profiles compared to MB with standard assumptions (black dashed): MB (yellow), Herquist (green), Via Lactea II (purple) and *right:* Einasto (yellow), NFW (red), Burkert (green) and MB with $\rho_\chi = 0.4$ GeV cm^{-3} (dotted).

2.3.2 Signal Simulation and Parameter Reconstruction

After specifing a WIMP model:

- WIMP mass m_χ,
- proton cross section $\sigma_{\chi p}$,
- isospin violating factor $\frac{f_n}{f_p}$, and
- inelastic parameter δ,

we generate an Asimov dataset of recoil events according to the differential event rate Eq. 2.4. The simulated events are binned as defined in the previous section and the MultiNest sampler [74] is used to reconstruct the WIMP model parameters (or a subset therein). MultiNest returns the full posterior probability distribution via Bayes theorem,

$$\mathcal{P}(\theta, D|I) = \frac{\mathcal{L}(D|\theta, I)\pi(\theta, I)}{\epsilon(D, I)}, \tag{2.25}$$

where the likelihood function is as previously defined in Eq. 2.24, and π and ϵ are the prior probabilities and Bayesian evidence respectively. The types of priors used are

given in Table 2.3. We then marginalize the posterior probability over all parameters except WIMP mass and proton cross section. Except where otherwise noted, the inelastic and isospin violating parameters were fixed to $\delta = 0$ keV and $\frac{f_n}{f_p} = 1$ and not allowed to vary in the reconstruction.

Table 2.3: The chosen priors for the WIMP sampling parameters and the standard astrophysical parameters, motivated by [75, 76, 77], errors denote 1-sigma intervals.

Parameter	Range	Prior
m_χ	$1 - 2000$ GeV	log
$\sigma_{\chi p}$	$10^{-48} - 10^{-42}$ cm^2	log
$\frac{f_n}{f_p}$	-4 $-$ 4	linear
δ	$0 - 100$ keV	linear
v_0	220 ± 20 km/s	Gaussian
v_{esc}	544 ± 40 km/s	Gaussian
ρ_χ	0.3 ± 0.1 GeV/cm^2	Gaussian

To test the complementarity of a xenon and argon detector, WIMP events with $\sigma_{\chi p} = 3 \times 10^{-46}$ cm^2 and masses of 20, 100 and 500 GeV were simulated for xenon and xenon plus argon detector configurations. The resulting detector reconstructions are shown in Fig. 2.7 (left). The Helm form factor and MB distribution were used (with uncertainties marginalized). The results show, with the detectors working together, that complementarity does provide a small improvement across the whole mass range, but most significantly at 100GeV (approximately the crossover between the different detector sensitivities). It is interesting to contrast this with the improvement gained by increasing the exposure of the xenon detector alone, either through increasing the exposure time or fiducial volume also shown in Fig. 2.7 left. This allows us to compare the increase in sensitivity due to the complementarity between the targets versus the improvement due to the increased exposure. We can see that by using the

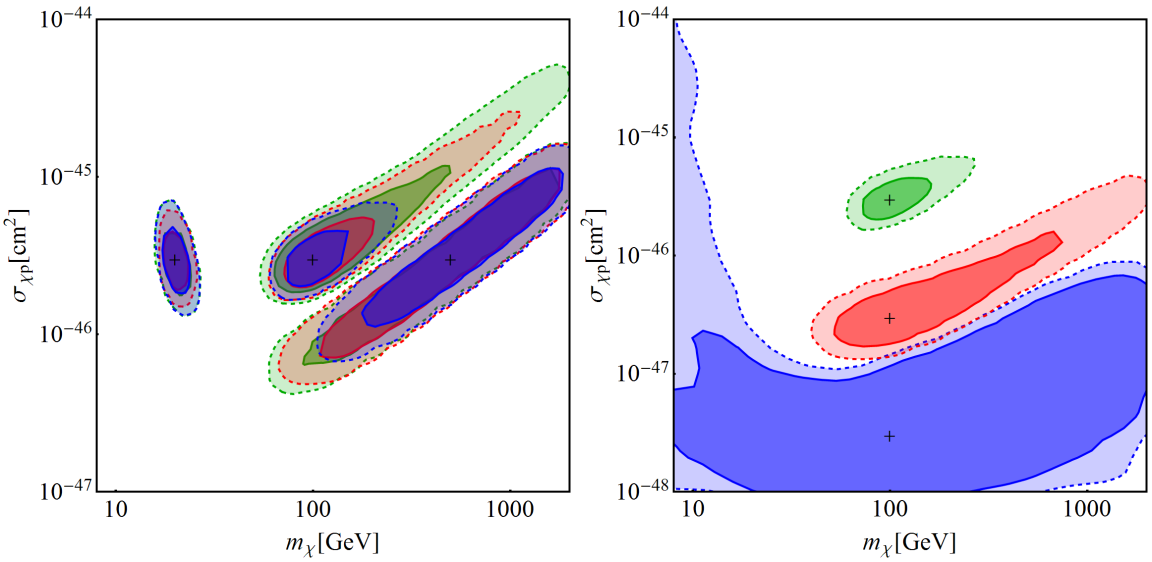

Figure 2.7: One- and two-sigma credible regions of the marginal posterior probabilities for simulations of WIMPs with *left:* $\sigma_{\chi p} = 3 \times 10^{-46}$ cm^2, and masses 20GeV, 100GeV and 500GeV, for exposures of 10 tonne-years xenon (green), 20 tonne-years xenon (red) and 10 tonne-years xenon plus 20 tonne-years argon (blue). *Right:* $\sigma_{\chi p} = 3 \times 10^{-46}$ cm^2 (green), $\sigma_{\chi p} = 3 \times 10^{-47}$ cm^2 (red) and $\sigma_{\chi p} = 3 \times 10^{-48}$ cm^2 (blue) for an exposure of 10 tonne-years xenon plus 20 tonne-years argon. The '+' indicates the simulated model.

two detectors there is an improvement in the 2σ error in the reconstructed mass, but at 1σ the improvement is very minor. Note that where degeneracies exist (e.g. the $m_\chi = 500$ GeV reconstruction in Fig. 2.7) or statistics are low (e.g. the $\sigma_{\chi p} = 3 \times 10^{-48}$ cm^2 reconstruction of Fig. 2.7 right) the apparent cutoff of the credible regions at the edges of the graphs are artifacts of our mass and cross section priors ($M \leq 2$ TeV, $\sigma \geq 10^{-48}$ cm^2).

In the case of isospin violating interactions, we still simulate a WIMP with $\frac{f_n}{f_p} = 1$, but now allow the value to vary during the reconstruction, assuming that $\frac{f_n}{f_p}$ has not been experimentally determined in advance. Due to the degeneracy between isospin violation and a change in the cross section, allowing $\frac{f_n}{f_p}$ to vary effectively increases the uncertainty in inferred cross section (see Fig. 2.8 left). The addition of a second detector has the potential to break this degeneracy; however, in practice

the astrophysical uncertainties make this impossible. The inclusion of the argon detector greatly improves mass reconstruction, but has a limited effect on reducing the uncertainty in the inferred cross section (see Fig. 2.8 left and right). Also, we once again see that there is not much improvement in reconstruction when using two different detector targets compared with doubling the size of the xenon detector. However, it is possible that with the addition of more detectors of different target material, one can at least infer the sign of $\frac{f_n}{f_p}$ [25].

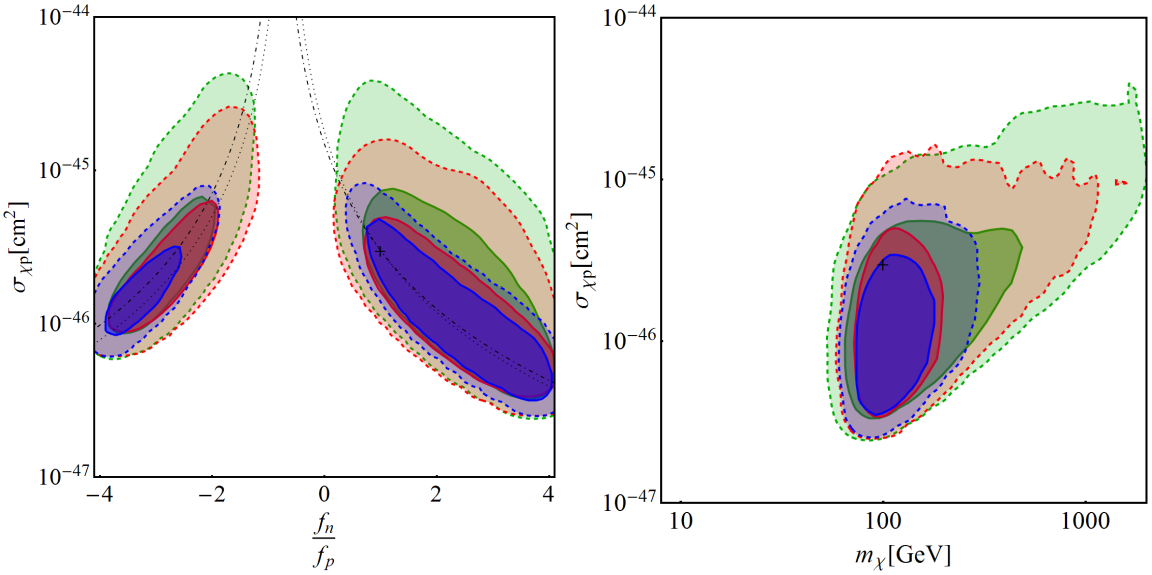

Figure 2.8: One- and two-sigma credible regions of the marginal posterior probabilities for simulations of WIMPs with $\sigma_{\chi p} = 3 \times 10^{-46}$ cm^2, $m_\chi = 100$ GeV, $\frac{f_n}{f_p} = 1$ and $\delta = 0$ keV. In both figures the isospin violating parameter $\frac{f_n}{f_p}$ is allowed to vary during reconstruction. The dotted and dot-dashed curves show the degeneracy between $\sigma_{\chi p}$ and $\frac{f_n}{f_p}$ for argon and xenon respectively. Shown are exposures of 10 tonne-years xenon (green), 20 tonne-years xenon (red) and 10 tonne-years xenon plus 20 tonne-years argon (blue). (*Left*): Reconstruction in the $\sigma_{\chi p} - \frac{f_n}{f_p}$ plane. (*Right*): Reconstruction in the $\sigma_{\chi p} - m_\chi$ plane (note that the spikes are due to sampling error in the reconstruction).

Although a less generic physical possibility, the addition of a non-zero inelastic scattering probability greatly increases the uncertainty in the reconstruction, since the event rate is decreased in this scenario. The event rate is diminished to such an

extent that for $\delta = 100$ keV, there are no inelastic events visible for a 100GeV WIMP with $\sigma_{\chi p} = 3 \times 10^{-46}$ cm^2. Events are observable for $\delta = 50$ keV, and here the complementarity of the two detectors provides a small improvement in the reconstruction (see Fig. 2.9 left), compared with doubling the xenon exposure. Fixing $\delta = 0$ during simulation while allowing it to vary during reconstruction gives a modest increase in the uncertainty in the reconstruction compared to assuming a specific value of δ, shown in Fig. 2.9 right. The second detector plays a stronger role in the reconstruction of the value of δ, providing a substantially stronger constraint on δ than obtained by doubling the size of the Xenon component, shown in Fig. 2.10.

Combining these two effects, if we assume neither $f_n/f_p = 1$ nor $\delta = 0$ keV in the reconstruction, then the WIMP properties can only weekly be constrained. Fig. 2.11 left shows that similarly to the individual cases, f_n/f_p and δ are only weekly constrained with individual detectors, while there is a strong improvement in the reconstruction of δ once data from the two detectors are combined. Interestingly, large values of δ seem to prefer positive values of f_n/f_p. Fig. 2.11 right shows that little information can be obtained about the WIMP mass or cross section under these relaxed assumptions. In particular, the reconstruction of the cross section is substantially worse than under the standard assumptions of Fig. 2.7 left.

2.4 Conclusions

Given the current understanding of possible WIMP candidates for dark matter, the greatest difficulty in extracting dark matter properties in direct detection experiments arises from astrophysical uncertainties–in particular the underlying phase space distribution in our halo. The existence of two different detector targets, each with similar overall sensitivity but different sorts of systematic uncertainties, will certainly aid in differentiating any claimed signal from possible background, but the question

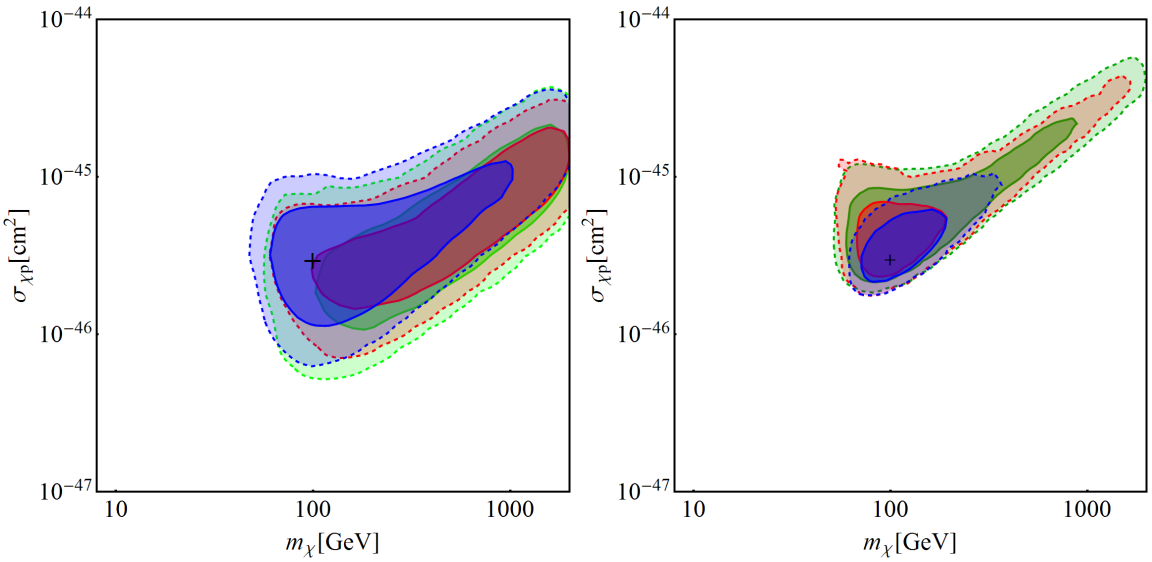

Figure 2.9: One- and two-sigma credible regions of the marginal posterior probabilities for simulations of WIMPs with the same values of m_χ, $\sigma_{\chi p}$ and $\frac{f_n}{f_p}$ as in Fig. 2.8. In both figures the inelastic scattering parameter δ is allowed to vary during reconstruction. Shown are exposures of 10 tonne-years xenon (green), 20 tonne-years xenon (red) and 10 tonne-years xenon plus 20 tonne-years argon (blue). (*Left*): $\delta = 0$ keV during simulation, allowed to vary during reconstruction. (*Right*): $\delta = 50$ keV during simulation, allowed to vary during reconstruction.

arises as to what extent degeneracies in mass and cross section reconstruction can be further reduced in the event of separate signals in the two detectors.

The DM direct-detection simulation and reconstruction program we have developed addresses this question, in addition to exploring the dominant sources of uncertainty in the expected signal, with some surprising results. In particular, the complementarity between xenon and argon targets only modestly improves the ability to remove the degeneracies affecting mass and cross section determinations, and for dark matter particles in excess of around 200 GeV the allowed range in mass-cross section space begins to blow up. While a number of particle physics parameters produce sub-dominant uncertainties in reconstructing dark matter parameters from an observed signal, the possibility of isospin violation in particular can dramatically increase the uncertainty in derived parameters. Additional (or a different combina-

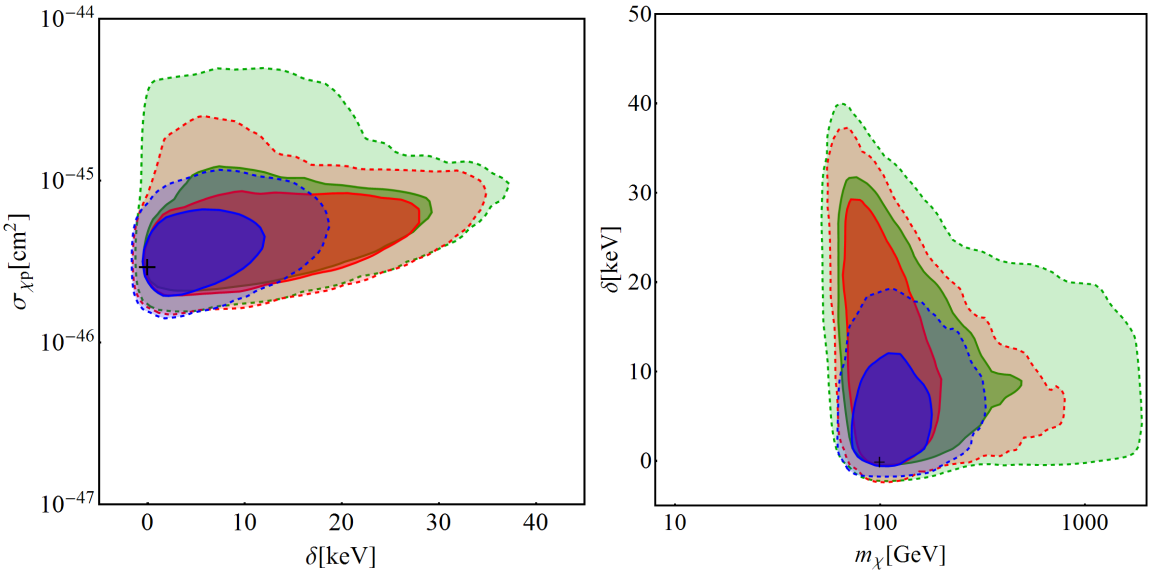

Figure 2.10: One- and two-sigma credible regions of the marginal posterior probabilities for simulations of WIMPs with the same parameters as in Fig. 2.8. In both figures the inelastic scattering parameter is fixed to $\delta = 0$ keV during simulation and allowed to vary during reconstruction. Shown are exposures of 10 tonne-years xenon (green), 20 tonne-years xenon (red) and 10 tonne-years xenon plus 20 tonne-years argon (blue). (*Left*): Reconstruction in the $\sigma_{\chi p} - \delta$ plane. (*Right*): Reconstruction in the $\delta - m_\chi$ plane.

tion of) detector targets would be needed to try to disentangle the effects of isospin violation from a reduction in cross section. Improved constraints in halo parameters would assist greatly in reconstruction efforts as well.

While possible spin-dependent effects in WIMP scattering will further complicate the reconstruction effort, they will also provide another handle on distinguishing signals from background and exploiting the complementarity of different target nuclei. Future improvements in our program will determine to what extent the two competing effects will alter the ability to determine WIMP properties based on signals in direct detection experiments.

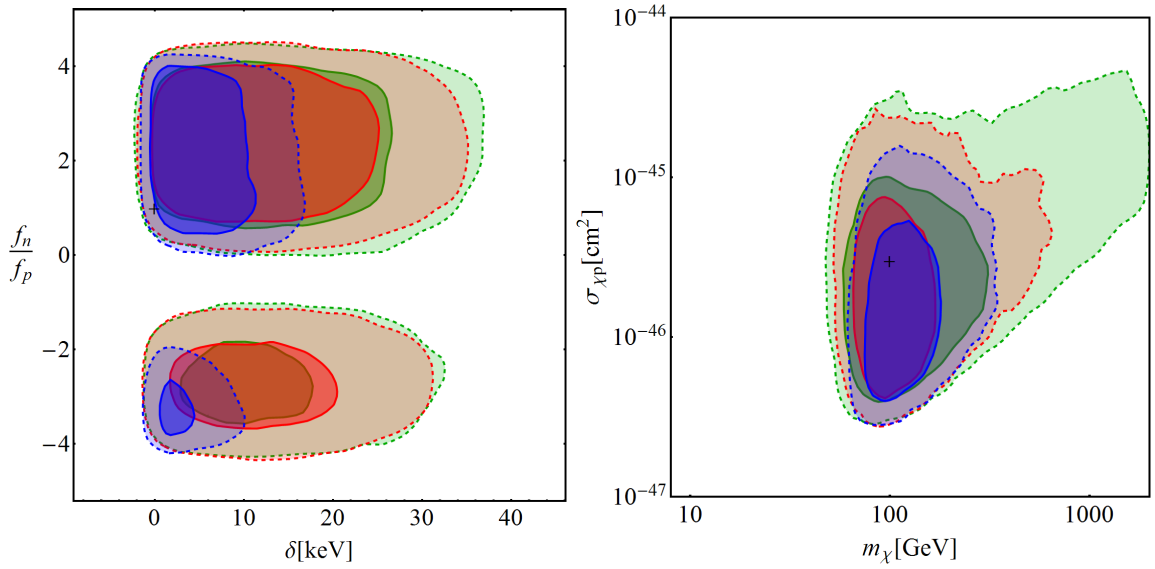

Figure 2.11: One- and two-sigma credible regions of the marginal posterior probabilities for simulations of WIMPs with the same parameters as in Fig. 2.8. In both figures, both $\frac{f_n}{f_p}$ and δ are fixed to the values in Fig. 2.8 during simulation and allowed to vary during reconstruction. Shown are exposures of 10 tonne-years xenon (green), 20 tonne-years xenon (red) and 10 tonne-years xenon plus 20 tonne-years argon (blue). (*Left*): Reconstruction in the $\frac{f_n}{f_p} - \delta$ plane. (*right*): Reconstruction in the $\sigma_{\chi p} - m_\chi$ plane.

Chapter 3

A GENERAL ANALYSIS OF DARK MATTER DIRECT DETECTORS

We derive a complete set of non-relativistic operators, their coefficients, and nuclear matrix elements relevant for direct detection rates and recoil spectra for scattering on various target nuclei. We begin with a general set of simplified dark matter models for spin-0, spin-$\frac{1}{2}$, and spin-1 dark matter candidates, composed of Lorentz invariant and renormalizable Lagrangians. This allows us to explore what high energy physics constraints might be obtainable from direct detection experiments, what degeneracies exist, which operators are ubiquitous and which are unlikely or sub-dominant. We find that there are operators which are common to all spins as well operators which are unique to spin-$\frac{1}{2}$ and spin-1. In addition we demonstrate how recoil energy spectra can distinguish fundamental microphysics if multiple target nuclei are used. Our work provides a complete roadmap for taking generic fundamental dark matter theories and calculating rates in direct detection experiments. This provides a useful guide for experimentalists designing experiments and theorists developing new dark matter models.

3.1 Introduction

The existence of non-baryonic dark matter has been inferred from measurements including galactic rotation curves [78], large scale structure surveys [79, 80, 81], X-ray observations [82], gravitational lensing [83, 84], and cosmic microwave background anisotropy measurements [85], spanning cosmological eras from the present day to the remote past. This widespread and robust data has led to cold dark matter models with a cosmological constant, labeled ΛCDM becoming entrenched as the standard cosmological model.

Nevertheless, this impressive array of observations has only been sensitive to the *gravitational* influence of dark matter and constrained its relic abundance, leaving its particle nature as one of the most important open questions in physics. The search for dark matter includes indirect astrophysical searches ([86, 87, 88, 89, 90]), collider production efforts (for some examples of dark matter searches at the LHC, see [91, 92, 93, 94, 95]) which will examine new territory soon with LHC run 2 which will commence this year, and attempts to observe dark matter interactions with Standard Model (SM) particles via dark matter-nucleus scattering processes in direct detection experiments, to which we now turn.

The search for dark matter via direct detection goes back at least three decades [12, 11] and has been particularly vigorous over the last decade or so with experiments such as LUX [96], Xenon100 [31], CDMS II (Ge) [97], CDMS I (Si) [98], DAMA/LIBRA [99], COGENT [100], and CRESST [101] pushing ever deeper into weakly interacting dark matter mass and scattering cross-section parameter space, but has thus far failed to yield a convincing signal. In the near future detectors such as Super CDMS [102] (which has recently released its first results on low mass dark matter searches [14, 103]), XENON1T [72], and DARWIN [35] are expected to push the limits of direct detection orders of magnitude below the current levels.

In order to connect observations to microphysical models one needs a general framework within which to interpret the observations of direct detection experiments. For quite some time the prevailing method of analyzing dark matter-nucleus interactions has been to assume that dark matter is a weakly interacting massive particle (WIMP), and then to categorize the interactions as elastic and isospin conserving and either spin-independent or spin-dependent [12]. For some well studied models of dark matter, such as the weakly interacting Majorana neutralino found in supersymmetry models, this assumption is reasonable.

With an absence of observed dark matter signals, there has of late been a surge in interest in exploring more general types of interactions between dark matter and nuclei. Generalizations include inelastic and momentum dependent interactions, which may arise due to additional structure in the dark sector including excited dark matter states, or dark gauge bosons giving rise to electric and magnetic form factors [41, 104, 105, 106, 107, 108, 109, 110].

The formalism of choice for many of these investigations is relativistic effective field theory, which provides a model independent framework to analyse dark matter-SM interactions [111, 112, 113]. It has been shown that these effective theories break down when applied to high-momentum transfer experiments, such as the LHC [114]. Therefore analyses moved beyond this framework and have moved to what are labeled as 'simplified models' instead [115, 116, 117]. Simplified models are field theories which extend the SM by a single dark matter particle and a single mediator particle which allows the WIMP to communicate with quarks and/or leptons. The newly added dark matter content is assumed to be a singlet under the SM gauge groups (we will consider some cases where the particles mediating the interaction have SM charge). In this context it is then possible to calculate collider amplitudes valid at the high energies of interest in such experiments. Given this simple dark sector, one can write down an exhaustive list of every combination of WIMP and mediator spins, and all possible tree level interactions. These simplified models have now gained popularity for analyzing indirect detection signals [118, 119], allowing connections to be made with the growing body of literature which make use of them.

Another step towards placing dark matter-nucleus interactions on a general footing has been accomplished recently by utilizing a non-relativistic effective field theory (EFT) approach [120, 18, 121, 122]. Since the interactions in direct detection scenarios are assumed to take place due to an incoming dark matter particle with a typical

velocity $\mathcal{O}(100\text{km/s})$, the recoil momenta in such an interaction will be $\mathcal{O}(\lesssim 100\text{keV})$. The particle masses involved, including the nucleons of roughly GeV scale, the dark matter particles, which typically range from the GeV region to several orders of magnitude above, and mediators that can also be quite heavy compared to the typical interaction momenta, produce a situation where an EFT treatment is quite natural.

In order to circumvent as much model dependence as possible, one can construct general interactions which obey Galilean invariance, T-symmetry, and Hermiticity. These operators will take the standard effective four-particle interaction form, reminiscent of Fermi's original model of weak interactions. The non-relativistic interactions can be shown to be functions of only four parameters including the nucleon spin S_N, the dark matter spin S_χ, the momentum transfer, $\vec{q}$, and a kinematic variable $\vec{v}^\perp$ which is a function of the relative incoming $(\vec{v}_{\chi,in} - \vec{v}_{N,in})$ and outgoing velocities $\vec{v}_{\chi,out} - \vec{v}_{N,out}$

$$\vec{v}^\perp = \frac{1}{2}\left(\vec{v}_{\chi,in} - \vec{v}_{N,in} + \vec{v}_{\chi,out} - \vec{v}_{N,out}\right) = \vec{v}_{\chi,in} - \vec{v}_{N,in} + \frac{\vec{q}}{2\mu_N} \tag{3.1}$$

which obeys $\vec{v}^\perp \cdot \vec{q} = 0$. It was demonstrated in [18] that there exist fifteen such non-relativistic interactions which arise from twenty possible bi-linear combinations of dark matter and nucleons.

The formalism developed in [18] is unique in being the only analysis to comprehensively develop the nuclear physics of direct detection experiments. From this general framework it is now apparent that there are interactions beyond the standard spin independent/dependent type. The origins of these 'new' interactions are not necessarily exotic and it has been shown, in the context of relativistic EFT, how many of them can be generated [123].

What has been lacking to date however, is a completely general and comprehensive treatment that connects high energy microphysics with low-energy effective nuclear

matrix elements in a model independent way. It is possible, for example, that the various interactions listed in [18] can give rise to degeneracies where different fundamental dark matter Lagrangians, describing dark matter and interaction mediators of various spins, can produce the same interaction types. This will obviously pose problems for attempts to discern the properties of dark matter when interpreting the results of experimental data. Furthermore, dark matter may not be spin-$\frac{1}{2}$, which creates a need for extending the parametric framework from the four descriptors listed above. In particular, as we shall show, this allows the existence of new non-relativistic operators to appear in the low energy effective theory.

Motivated by the above we present here a general relativistic analysis covering a broad spectrum of particle and interaction types, starting from the microphysics, which will enable one to link experiment with fundamental theory while incorporating the new nuclear responses described in [18].

In this work we build upon the NR-EFT description by examining simplified models which incorporate the most general renormalizable Lagrangians for scalar, spinor, and vector dark matter interacting with nucleons via scalar, spinor, and vector mediators, consistent with Lorentz invariance and hermiticity while imposing stability of the dark matter candidates. We integrate out the heavy mediator and obtain effective relativistic interaction Lagrangians. Next, we take the non-relativistic limit of these Lagrangians, and identify them with the NR operators from [18], which are reproduced below, in Table 1. Using these, we identify which electroweak nuclear responses are excited by a given fundamental interaction model and determine the relative importance of various models within the context of direct detection experiments consisting of xenon and germanium targets by exploring the relative magnitude of coefficients of these operators, and also their energy dependence.

The paper is organized as follows; in section 3.2 the EFT formalism of [18] is summarized, in section 3.3 we build the generalized relativistic Lagrangians and in section 3.4 we outline the signatures and distinguishability of these models in the context of direct detection experiments, providing a framework for both experimentalists and theorists to base their future analyses.

3.2 Effective Field Theory of Direct Detection

Conventionally, coherent WIMP-nucleus scattering has been considered to come from two types of interactions; spin-independent (SI) and spin-dependent (SD). SI interactions couple to the charge/mass of the nucleus while SD couples to the spin. The nuclear cross section is generally written in terms of the nucleon cross section at zero momentum transfer, σ_0, and a form factor, $F(q)$, to take into account the loss of coherence over the finite size of the nucleus,

$$\frac{d\sigma}{dE_r} = \frac{M}{2\pi\mu_{\chi M}v^2}\left(\sigma_0^{SI}F_{SI}^2(q) + \sigma_0^{SD}F_{SD}^2(q)\right). \tag{3.2}$$

where M is the mass of the target nucleus and $\mu_{\chi M}$ is the WIMP-nucleus reduced mass. This picture has recently been shown to be incomplete, as it is also possible for the WIMP to couple to the nucleus through additional nuclear responses [18]. Working in the language of a non-relativistic (NR) effective field theory Fitzpatrick et al. identified 15 operators to characterize the ways in which a WIMP can couple to the various nuclear responses. These operators are constructed from combinations of non-relativistic vectors which respect Galilean invariance, T symmetry and which are Hermitian. We list them in table 5.1. The Hermitian vectors are:

$$i\frac{\vec{q}}{m_N},\ \vec{v}^{\perp} = \vec{v} + \frac{\vec{q}}{2\mu_N},\ \vec{S}_\chi,\ \vec{S}_N, \tag{3.3}$$

where $\vec{q} = \vec{p'} - \vec{p} = \vec{k} - \vec{k'}$ is the momentum transfer, $\vec{v}$ is the velocity of WIMP with respect to the nucleus of the detector, μ_N is the reduced mass of the system and $\vec{S}_\chi$

and $\vec{S}_N$ are the WIMP and nuclear spins respectively. Throughout the paper, we denote by $\vec{p}$ and $\vec{p'}$ the incoming and outgoing WIMP momenta and by $\vec{k}$ and $\vec{k'}$ the incoming and outgoing nuclear momenta respectively. Energy-momentum conservation implies the orthogonality condition $\vec{q} \cdot \vec{v}^{\perp} = 0$. Here we will briefly outline the procedure employed in [18] in going from the NR operators to the final differential WIMP-nucleus cross section.

Table 3.1: List of NR effective operators described in [18]

$\mathcal{O}_1$	$1_\chi 1_N$
$\mathcal{O}_2$	$(\vec{v}^{\perp})^2$
$\mathcal{O}_3$	$i\vec{S}_N \cdot (\frac{\vec{q}}{m_N} \times \vec{v}^{\perp})$
$\mathcal{O}_4$	$\vec{S}_\chi \cdot \vec{S}_N$
$\mathcal{O}_5$	$i\vec{S}_\chi \cdot (\frac{\vec{q}}{m_N} \times \vec{v}^{\perp})$
$\mathcal{O}_6$	$(\frac{\vec{q}}{m_N} \cdot \vec{S}_N)(\frac{\vec{q}}{m_N} \cdot \vec{S}_\chi)$
$\mathcal{O}_7$	$\vec{S}_N \cdot \vec{v}^{\perp}$
$\mathcal{O}_8$	$\vec{S}_\chi \cdot \vec{v}^{\perp}$
$\mathcal{O}_9$	$i\vec{S}_\chi \cdot (\vec{S}_N \times \frac{\vec{q}}{m_N})$
$\mathcal{O}_{10}$	$i\frac{\vec{q}}{m_N} \cdot \vec{S}_N$
$\mathcal{O}_{11}$	$i\frac{\vec{q}}{m_N} \cdot \vec{S}_\chi$
$\mathcal{O}_{12}$	$\vec{S}_\chi \cdot (\vec{S}_N \times \vec{v}^{\perp})$
$\mathcal{O}_{13}$	$i(\vec{S}_\chi \cdot \vec{v}^{\perp})(\frac{\vec{q}}{m_N} \cdot \vec{S}_N)$
$\mathcal{O}_{14}$	$i(\vec{S}_N \cdot \vec{v}^{\perp})(\frac{\vec{q}}{m_N} \cdot \vec{S}_\chi)$
$\mathcal{O}_{15}$	$-(\vec{S}_\chi \cdot \frac{\vec{q}}{m_N}) \left((\vec{S}_N \times \vec{v}^{\perp}) \cdot \frac{\vec{q}}{m_N} \right)$

In general one can write down the non-relativistic interaction Lagrangian as

$$\mathcal{L}_{NR} = \sum_{\alpha=n,p} \sum_{i=1}^{15} c_i^\alpha \mathcal{O}_i^\alpha, \tag{3.4}$$

where the coefficients c_i^α are given by the microphysics of the interaction and in general one could allow for isospin violation by having different couplings to neutron and proton inside the nucleus. This can be rewritten in 2-component isospin space as

$$\mathcal{L}_{NR} = \sum_{\tau=0,1} \sum_{i=1}^{15} c_i^\tau \mathcal{O}_i t^\tau \tag{3.5}$$

where t^0 and t^1 are the identity matrix and the Pauli matrix σ^3 respectively. The nucleus is composed of nucleons, and these can individually interact with the WIMP. This is incorporated by considering the operator $\mathcal{O}(j)$ as an interaction between a single nucleon, j, and the WIMP, and then summing over the nucleons.

$$\sum_{\tau=0,1} \sum_{i=1}^{15} c_i^\tau \mathcal{O}_i t^\tau \rightarrow \sum_{\tau=0,1} \sum_{i=1}^{15} c_i^\tau \sum_{j=1}^{A} \mathcal{O}_i(j) t^\tau(j) \tag{3.6}$$

where A is the atomic mass number given by the total number of neutrons and protons. One can do the same reduction with $\vec{v}^\perp$,

$$\begin{aligned} \vec{v}^\perp &\rightarrow \{\vec{v}_\chi - \vec{v}_N(i), i = 1, ..., A\} \\ &\equiv \vec{v}_T^\perp - \{\dot{\vec{v}}_N(i), i = 1, ..., A-1\} \end{aligned} \tag{3.7}$$

where $\vec{v}_\chi$ and $\vec{v}_N(i)$ are the symmetrized combination of incoming and outgoing velocities for the WIMP and nucleons respectively. $\vec{v}_T^\perp$ (here T stands for target, i.e., the nuclear center-of-mass) is defined as

$$\vec{v}_T^\perp = \vec{v}_\chi - \frac{1}{2A} \sum_{i=1}^{A} [\vec{v}_{N,in}(i) + \vec{v}_{N,out}(i)] \tag{3.8}$$

This allows for a decomposition of the nucleon velocities into internal velocities $\dot{\vec{v}}_N(i)$ that act only on intrinsic nuclear coordinates and 'in' and 'out' velocities that evolve as a WIMP scatters off the detector. As an example, the dot product between $\vec{v}_N^\perp$ and $\vec{S}_N$ can be rewritten as

$$\vec{v}^\perp \cdot \vec{S}_N \rightarrow \sum_{i=1}^{A} \frac{1}{2} [\vec{v}_{\chi,in} + \vec{v}_{\chi,out} - \vec{v}_{N,in}(i) - \vec{v}_{N,out}(i)] \cdot \vec{S}_N(i) \tag{3.9}$$

$$= \vec{v}_T^\perp \cdot \sum_{i=1}^{A} \vec{S}_N(i) - \left\{ \sum_{i=1}^{A} \frac{1}{2} [\vec{v}_{N,in}(i) + \vec{v}_{N,out}(i)] \cdot \vec{S}_N(i) \right\}_{int} \tag{3.10}$$

The second term in the curly brackets is internal to the nucleus and acts as an operator on the 'in' and 'out' nucleon states. $\vec{v}_{N,in}$ can be replaced by $\vec{p}_{N,in}/M$ acting on the incoming state, which can in turn be replaced by $i\overleftarrow{\nabla}/M$, and similarly $\vec{p}_{N,out}/M$ by $-i\overrightarrow{\nabla}/M$ on the outgoing nuclear state. Finally, since the nucleus is non-zero in size and individual nucleons locally interact with the WIMP, nuclear operators built from $\mathcal{O}_i$ are accompanied by an additional spatial operator $e^{-i\vec{q}\cdot\vec{x}(i)}$ where $x(i)$ is the location of the i^{th} nucleon inside the nucleus.

Starting from Eqn. 3.6 and using the substitution rules for $\vec{v}^{\perp}$ and including a factor of $e^{-i\vec{q}\cdot\vec{x}_i}$, the interaction Lagrangian can be written as a sum of five distinct terms (nuclear electroweak operators) that only act on internal nucleon states. Their coefficients, on the other hand, act on WIMP 'in' and 'out' states. The WIMP-nucleus interaction can then be written as

$$\sum_{\tau=0,1}\left\{l_0^\tau S + l_0^{A\tau} T + \vec{l}_5^\tau\cdot\vec{P} + \vec{l}_M^\tau\cdot Q + \vec{l}_E^\tau\cdot\vec{R}\right\}t^\tau(i) \tag{3.11}$$

where

$$\begin{aligned}
S &= \sum_{i=1}^{A} e^{-i\vec{q}\cdot\vec{x}_i} \\
T &= \sum_{i=1}^{A}\frac{1}{2M}\left[-\frac{1}{i}\overleftarrow{\nabla}_i\cdot\vec{\sigma}(i)e^{-i\vec{q}\cdot\vec{x}_i} + e^{-i\vec{q}\cdot\vec{x}_i}\vec{\sigma}(i)\cdot\frac{1}{i}\overrightarrow{\nabla}_i\right] \\
\vec{P} &= \sum_{i=1}^{A}\vec{\sigma}(i)e^{-i\vec{q}\cdot\vec{x}_i} \\
\vec{Q} &= \sum_{i=1}^{A}\frac{1}{2M}\left[-\frac{1}{i}\overleftarrow{\nabla}_i e^{-i\vec{q}\cdot\vec{x}_i} + e^{-i\vec{q}\cdot\vec{x}_i}\frac{1}{i}\overrightarrow{\nabla}_i\right] \\
\vec{R} &= \sum_{i=1}^{A}\frac{1}{2M}\left[\overleftarrow{\nabla}_i\times\vec{\sigma}(i)e^{-i\vec{q}\cdot\vec{x}_i} + e^{-i\vec{q}\cdot\vec{x}_i}\vec{\sigma}(i)\times\overrightarrow{\nabla}_i\right]
\end{aligned} \tag{3.12}$$

and

$$
\begin{aligned}
l_0^\tau &= c_1^\tau + ic_5^\tau \vec{S}_\chi \cdot \left(\frac{\vec{q}}{m_N} \times \vec{v}_T^\perp\right) + c_8^\tau(\vec{S}_\chi \cdot \vec{v}_T^\perp) + ic_{11}^\tau \frac{\vec{q}\cdot\vec{S}_\chi}{m_N} \\
l_0^{A\tau} &= -\frac{1}{2}\left[c_7^\tau + ic_{14}^\tau\left(\vec{S}_\chi \cdot \frac{\vec{q}}{m_N}\right)\right] \\
\vec{l}_5 &= \frac{1}{2}\left[c_3^\tau i\frac{\left(\vec{q}\times\vec{v}_T^\perp\right)}{m_N} + c_4^\tau\vec{S}_\chi + c_6^\tau\frac{(\vec{q}\cdot\vec{S}_\chi)\vec{q}}{m_N^2} + c_7^\tau\vec{v}_T^\perp + ic_9^\tau\frac{(\vec{q}\times\vec{S}_\chi)}{m_N} + ic_{10}^\tau\frac{\vec{q}}{m_N}\right) \\
&\quad c_{12}^\tau(\vec{v}_T^\perp \times \vec{S}_\chi) + ic_{13}^\tau\frac{(S_\chi\cdot\vec{v}_T^\perp)\vec{q}}{m_N} + ic_{14}^\tau\left(\vec{S}_\chi\cdot\frac{\vec{q}}{m_N}\right)\vec{v}_T^\perp + c_{15}^\tau\frac{(\vec{q}\cdot\vec{S}_\chi)(\vec{q}\times\vec{v}_T^\perp)}{m_N^2}\Bigg] \\
\vec{l}_M &= c_5^\tau\left(i\frac{\vec{q}}{m_N}\times\vec{S}_\chi\right) - \vec{S}_\chi c_8^\tau \\
\vec{l}_E &= \frac{1}{2}\left[c_3^\tau\frac{\vec{q}}{m_N} + ic_{12}^\tau\vec{S}_\chi - c_{13}^\tau\frac{(\vec{q}\times\vec{S}_\chi)}{m_N} - ic_{15}^\tau\frac{(\vec{q}\cdot\vec{S}_\chi)\vec{q}}{m_N^2}\right]
\end{aligned}
\tag{3.13}
$$

The WIMP-nucleus amplitude, $\mathcal{M}$, can then be succinctly written as

$$
\mathcal{M} = \sum_{\tau=0,1}\langle j_\chi, M_\chi; j_N, M_N|\left\{l_0^\tau S + l_0^{A\tau}T + \vec{l}_5^\tau\cdot\vec{P} + \vec{l}_M^\tau\cdot Q + \vec{l}_E^\tau\cdot\vec{R}\right\}t^\tau(i)|j_\chi, M_\chi; j_N, M_N\rangle.
\tag{3.14}
$$

By using spherical decomposition, the internal nuclear operators S, T, P, Q and R can be further rewritten in terms of standard nuclear electroweak responses as follows:

$$
\begin{aligned}
\mathcal{M} &= \sum_{\tau=0,1}\langle j_\chi, M_{\chi f}; j_N, M_{Nf}|\left(\sum_{J=0}\sqrt{4\pi(2J+1)}(-i)^J\left[l_0^\tau M_{J0;\tau} - il_0^{A\tau}\frac{q}{m_N}\tilde{\Omega}_{J0;\tau}(q)\right]\right. \\
&\quad + \sum_{J=1}\sqrt{2\pi(2J+1)}(-i)^J\sum_{\lambda\pm1}(-1)^\lambda\left\{l_{5\lambda}^\tau[\lambda\Sigma_{J-\lambda;\tau}(q) + i\Sigma'_{J-\lambda;\tau}(q)]\right. \\
&\quad \left.-i\frac{q}{m_N}l_{M\lambda}^\tau[\lambda\Delta_{J-\lambda;\tau}(q)] - i\frac{q}{m_N}l_{E\lambda}^\tau[\lambda\tilde{\Phi}_{J-\lambda;\tau}(q) + i\tilde{\Phi}'_{J-\lambda;\tau}(q)]\right\} \\
&\quad \left.+\sum_{J=0}^{\infty}\sqrt{4\pi(2J+1)}(-i)^J\left[il_{50}^\tau\Sigma''_{J0;\tau}(q) + \frac{q}{m_N}l_{M0}^\tau\tilde{\Delta}''_{J0;\tau}(q) + \frac{q}{m_N}l_{E0}^\tau\tilde{\Phi}''_{J0;\tau}(q)\right]\right)|j_\chi, M_{\chi i}; j_N, M_{Ni}\rangle
\end{aligned}
\tag{3.15}
$$

Where there is an implicit sum over the nucleons,

$$
\mathcal{O}_{JM;\tau}(q) \equiv \sum_{i=1}^{A}\mathcal{O}_{JM}(q\vec{x}_i)t^\tau(i),
\tag{3.16}
$$

and the various electroweak responses are defined as

$$
\begin{aligned}
M_{JM}(q\vec{x}) &\equiv j_J(qx)Y_{JM}(\Omega_x) \\
\vec{M}^M_{JL} &\equiv j_J(qx)\vec{Y}_{JLM}(\Omega_x) \\
\Delta_{JM} &\equiv \vec{M}^M_{JJ}(qx_i)\cdot\frac{1}{q}\vec{\nabla}_i \\
\Sigma'_{JM} &\equiv -i\left\{\frac{1}{q}\vec{\nabla}_i\times\vec{M}^M_{JJ}(q\vec{x}_i)\right\}\cdot\vec{\sigma}(i) \\
\Sigma''_{JM} &\equiv \left\{\frac{1}{q}\vec{\nabla}_i M_{JM}(q\vec{x}_i)\right\}\cdot\vec{\sigma}(i) \\
\tilde{\Phi}'_{JM} &\equiv \left[\frac{1}{q}\vec{\nabla}_i\times\vec{M}^M_{JJ}(q\vec{x}_i)\right]\cdot\left[\vec{\sigma}(i)\times\frac{1}{q}\vec{\nabla}_i\right]+\frac{1}{2}\vec{M}^M_{JJ}(q\vec{x}_i)\cdot\vec{\sigma}(i) \\
\Phi''_{JM} &\equiv i\left[\frac{1}{q}\vec{\nabla}_i M_{JM}(q\vec{x}_i)\right]\cdot\left[\vec{\sigma}(i)\times\frac{1}{q}\vec{\nabla}_i\right] \\
\Sigma_{JM} &\equiv \vec{M}^M_{JJ}(q\vec{x}_i)\cdot\vec{\sigma}(i) \\
\tilde{\Omega}_{JM} &\equiv \Omega_{JM}(q\vec{x}_i)+\frac{1}{2}\Sigma''_{JM}(q\vec{x}_i) \\
\tilde{\Phi}_{JM} &\equiv \Phi_{JM}(qx_i)-\frac{1}{2}\Sigma'_{JM}(qx_i) \\
\tilde{\Delta}''_{JM} &\equiv \Delta''_{JM}(qx_i)-\frac{1}{2}M_{JM}(qx_i)
\end{aligned}
\tag{3.17}
$$

where Y_{JM} and $\vec{Y}_{JLM}$ are spherical harmonics and vector spherical harmonics respectively. We are only considering elastic transitions, and assuming parity and CP as symmetries of the nuclear ground state. This eliminates some of the responses, and only $M, \Phi'', \Sigma', \Delta, \Sigma'', \tilde{\Phi}'$ survive. To calculate cross-sections, one needs to square the amplitude, average over initial spins and sum over final spins. The matrix element squared for the nuclear portion of the amplitude has been made available by Fitzpatrick et al. [18], and codes have been supplied to calculate the full amplitude and rate [121].

As we shall describe, in the following analysis we discovered that two additional

NR operators are required to fully describe the scattering of spin-1 WIMPs off nuclei,

$$\mathcal{O}_{17} \equiv \frac{i\vec{q}}{m_N} \cdot \mathcal{S} \cdot \vec{v}_\perp,$$
$$\mathcal{O}_{18} \equiv \frac{i\vec{q}}{m_N} \cdot \mathcal{S} \cdot \vec{S}_N, \tag{3.18}$$

where $\mathcal{S}$ is the symmetric combination of polarization vectors. Appendix A contains the details required to include these new operators in the above formalism.

3.3 Simplified Models for Direct Detection

From a model building perspective, one would like to know how relevant the novel nuclear responses are in interpreting direct detection data. Previous work [123] demonstrated that using only the SI/SD form factors (even with additional momentum dependence taken into account) can lead one to infer wildly incorrect values of the WIMP mass and cross sections.

Here we go further by starting with simplified models at the Lagrangian level, where 'simplified model' means a single WIMP with a single mediator coupling it to the quark sector. This is useful for two reasons; it allows us to better explore which NR operators arise from a broad set of UV complete theories, and also make connection with the growing body of literature which use simplified models for indirect detection and collider searches.

When it comes to interpreting signals, knowing comprehensively how different interactions with different nuclei arise from different UV complete models will allow us to identify degeneracies between competing models. Further, it can also help optimize target selection for maximum discrimination of the UV model parameter space.

In building these simplified models we remain agnostic about the WIMP's spin,

and consider dark matter spins of $0, \frac{1}{2}$ and 1. We do however only consider renormalizable interactions between quarks and WIMPs. To ensure a stable WIMP, we assume that the WIMP is either charged under some internal gauge group or a discrete symmetry group (for example Z_2). However, we assume that this gauge charge is not shared by quarks. We will couple the WIMP to the quarks via a heavy mediator in two distinct ways: charged and uncharged mediators, each with all possible spins consistent with angular momentum conservation. The mediator mass is chosen to be the heaviest scale in the problem (and certainly much greater than the momentum exchange which characterizes the scattering process) so that we can integrate it out (see appendix B for details). This leads to relativistic effective WIMP-nucleon interactions, whose NR limit can then be examined. In the uncharged mediator case we will consider mediators that are neutral under all SM and WIMP gauge charges, while in the charged case, the mediator must have both WIMP and SM gauge charges. Given the above as a guide, our Lagrangian construction is then constrained only by gauge invariance, Lorentz invariance, renormalizability and hermiticity.

A. Uncharged-mediator Lagrangians

1. Scalar Dark Matter

We begin with a spin-0 scalar WIMP, S, which has some internal charge to ensure stability, and $S^\dagger$ is its Hermitian conjugate. To have renormalizable interactions, the neutral mediator can only be a scalar or a vector. We denote the scalar mediator by ϕ and the vector mediator by G^μ with field strength tensor $\mathcal{G}_{\mu\nu}$. Unless otherwise noted, all of the following coupling constants are real and dimensionless.

The most general renormailzable Lagrangian for scalar mediation consistent with

the above assumptions is given by

$$\begin{aligned}\mathcal{L}_{S\phi q} &= \partial_\mu S^\dagger \partial^\mu S - m_S^2 S^\dagger S - \frac{\lambda_S}{2}(S^\dagger S)^2 \\ &+\frac{1}{2}\partial_\mu\phi\partial^\mu\phi - \frac{1}{2}m_\phi^2\phi^2 - \frac{m_\phi\mu_1}{3}\phi^3 - \frac{\mu_2}{4}\phi^4 \\ &+i\bar{q}\not{\partial}q - m_q\bar{q}q \\ &-g_1 m_S S^\dagger S\phi - \frac{g_2}{2}S^\dagger S\phi^2 - h_1\bar{q}q\phi - ih_2\bar{q}\gamma^5 q\phi, \end{aligned} \tag{3.19}$$

where we have suppressed all the SM quark interactions. Similarly, the Lagrangian for vector mediation (up to gauge fixing terms) is

$$\begin{aligned}\mathcal{L}_{SGq} &= \partial_\mu S^\dagger \partial^\mu S - m_S^2 S^\dagger S - \frac{\lambda_S}{2}(S^\dagger S)^2 \\ &-\frac{1}{4}\mathcal{G}_{\mu\nu}\mathcal{G}^{\mu\nu} + \frac{1}{2}m_G^2 G_\mu G^\mu - \frac{\lambda_G}{4}(G_\mu G^\mu)^2 \\ &+i\bar{q}\not{\partial}q - m_q\bar{q}q \\ &-\frac{g_3}{2}S^\dagger S G_\mu G^\mu - ig_4(S^\dagger\partial_\mu S - \partial_\mu S^\dagger S)G^\mu \\ &-h_3(\bar{q}\gamma_\mu q)G^\mu - h_4(\bar{q}\gamma_\mu\gamma^5 q)G^\mu. \end{aligned} \tag{3.20}$$

2. Spin-$\frac{1}{2}$ Dark Matter

If the WIMP has spin-$\frac{1}{2}$ (denoted by χ below), then, as in the scalar WIMP case, mediation will only occur via scalar or vector mediators. The most general renormalizable interactions for the scalar (ϕ) and vector mediator (G_μ) cases respectively are

given below,

$$\begin{aligned}\mathcal{L}_{\chi\phi q} &= i\bar{\chi}\not{D}\chi - m_\chi\bar{\chi}\chi \\ &\quad +\frac{1}{2}\partial_\mu\phi\partial^\mu\phi - \frac{1}{2}m_\phi^2\phi^2 - \frac{m_\phi\mu_1}{3}\phi^3 - \frac{\mu_2}{4}\phi^4 \\ &\quad +i\bar{q}\not{D}q - m_q\bar{q}q \\ &\quad -\lambda_1\phi\bar{\chi}\chi - i\lambda_2\phi\bar{\chi}\gamma^5\chi - h_1\phi\bar{q}q - ih_2\phi\bar{q}\gamma^5 q, \end{aligned} \tag{3.21}$$

$$\begin{aligned}\mathcal{L}_{\chi Gq} &= i\bar{\chi}\not{D}\chi - m_\chi\bar{\chi}\chi \\ &\quad -\frac{1}{4}\mathcal{G}_{\mu\nu}\mathcal{G}^{\mu\nu} + \frac{1}{2}m_G^2 G_\mu G^\mu \\ &\quad +i\bar{q}\not{D}q - m_q\bar{q}q \\ &\quad -\lambda_3\bar{\chi}\gamma^\mu\chi G_\mu - \lambda_4\bar{\chi}\gamma^\mu\gamma^5\chi G_\mu \\ &\quad -h_3\bar{q}\gamma_\mu q G^\mu - h_4\bar{q}\gamma_\mu\gamma^5 q G^\mu. \end{aligned} \tag{3.22}$$

3. Spin-1 Dark Matter

If the WIMP is a massive spin-1 particle, uncharged mediation to the quark sector can occur via a heavy scalar or a vector particle. For the case of vector mediation, there are many possible interactions because the Lorentz indices on the vectors afford a more diverse set of terms. The general interaction Lagrangian for the scalar mediation case is

$$\begin{aligned}\mathcal{L}_{X\phi q} &= -\frac{1}{2}\mathcal{X}^\dagger_{\mu\nu}\mathcal{X}^{\mu\nu} + m_X^2 X^\dagger_\mu X^\mu - \frac{\lambda_X}{2}(X^\dagger_\mu X^\mu)^2 \\ &\quad +\frac{1}{2}(\partial_\mu\phi)^2 - \frac{1}{2}m_\phi^2\phi^2 - \frac{m_\phi\mu_1}{3}\phi^3 - \frac{\mu_2}{4}\phi^4 \\ &\quad +i\bar{q}\not{D}q - m_q\bar{q}q \\ &\quad -b_1 m_X\phi X^\dagger_\mu X^\mu - \frac{b_2}{2}\phi^2 X^\dagger_\mu X^\mu - h_1\phi\bar{q}q - ih_2\phi\bar{q}\gamma^5 q. \end{aligned} \tag{3.23}$$

For the case of vector mediation, there are many possible interactions because the Lorentz indices on the vectors afford a more diverse set of terms. The Lagrangian is given by

$$\begin{aligned}
\mathcal{L}_{XGq} &= -\frac{1}{2}\mathcal{X}^{\dagger}_{\mu\nu}\mathcal{X}^{\mu\nu} + m_X^2 X^{\dagger}_{\mu}X^{\mu} - \frac{\lambda_X}{2}(X^{\dagger}_{\mu}X^{\mu})^2 \\
&\quad -\frac{1}{4}\mathcal{G}_{\mu\nu}\mathcal{G}^{\mu\nu} + \frac{1}{2}m_G^2 G_{\mu}^2 - \frac{\lambda_G}{4}(G_{\mu}G^{\mu})^2 \qquad (3.24) \\
&\quad +i\bar{q}\not{D}q - m_q\bar{q}q \\
&\quad -\frac{b_3}{2}G_{\mu}^2(X^{\dagger}_{\nu}X^{\nu}) - \frac{b_4}{2}(G^{\mu}G^{\nu})(X^{\dagger}_{\mu}X_{\nu}) - \Big[ib_5 X^{\dagger}_{\nu}\partial_{\mu}X^{\nu}G^{\mu} \\
&\quad +b_6 X^{\dagger}_{\mu}\partial^{\mu}X_{\nu}G^{\nu} + b_7\epsilon_{\mu\nu\rho\sigma}(X^{\dagger\mu}\partial^{\nu}X^{\rho})G^{\sigma} + h.c.\Big] \\
&\quad -h_3 G_{\mu}\bar{q}\gamma^{\mu}q - h_4 G_{\mu}\bar{q}\gamma^{\mu}\gamma^5 q \qquad (3.25)
\end{aligned}$$

where, for the Lagrangian to be Hermitian, b_6 and b_7 are complex (this implies a new source of CP violation, which will not be considered further here).

3.3.1 Charged-Mediator Lagrangians

Here we consider the simplest case of mediators that are charged under both the DM internal symmetry group and SM gauge groups. This is motivated by the absence of spin-$\frac{1}{2}$ mediators (s-channel processes) in the previous section. Such a mediator, if neutral, is forbidden by simultaneous requirements of gauge invariance and renormalizability. Dark Matter models with mediators endowed with charges from both DM and SM side have been considered in the literature before [124, 125]. The case of a spin-$\frac{1}{2}$ mediator carrying $SU(3)_c$ is also motivated by studies of heavy quark models. This allows unique interactions as we show below. In particular they necessitate a direct interaction between quarks and WIMPs at the level of the Lagrangian.

1. Scalar Dark Matter

Scalar WIMPs with a charged scalar or vector mediator do not lead to any Lorentz invariant interactions. This is easy to see since both the scalars (or scalar and vector) and the quark are required in the (gauge invariant) interaction, but there is no way to contract the spinor indices consistently if the mediating particle is a scalar or vector. Therefore, the only possibility is that of a spin-1/2 mediator, Q, which acts like a heavy quark. The general renormalizable action is given by

$$\begin{aligned}\mathcal{L}_{SQq} &= \partial_\mu S^\dagger \partial^\mu S - m_S^2 S^\dagger S - \lambda_S (S^\dagger S)^2 \\ &\quad + i\bar{Q}\not{\partial} Q - m_Q \bar{Q} Q \\ &\quad + i\bar{q}\not{\partial} q - m_q \bar{q} q \\ &\quad - (y_1 S \bar{Q} q + y_2 S \bar{Q} \gamma^5 q + h.c.),\end{aligned} \tag{3.26}$$

where y_1 and y_2 are again complex.

2. Spin-$\frac{1}{2}$ Dark Matter

For a spin-1/2 WIMP, both a charged scalar and charged vector mediator exchange can lead to novel interactions. The charged scalar is denoted by Φ and the charged vector by V_μ

$$\begin{aligned}\mathcal{L}_{\chi\Phi q} &= i\bar{\chi}\not{\partial}\chi - m_\chi \bar{\chi}\chi \\ &\quad + (\partial_\mu \Phi^\dagger)(\partial^\mu \Phi) - m_\Phi^2 \Phi^\dagger \Phi - \frac{\lambda_\Phi}{2}(\Phi^\dagger \Phi)^2 \\ &\quad + i\bar{q}\not{\partial} q - m_q \bar{q} q \\ &\quad - (l_1 \Phi^\dagger \bar{\chi} q + l_2 \Phi^\dagger \bar{\chi}\gamma^5 q + h.c.),\end{aligned} \tag{3.27}$$

$$\begin{aligned}\mathcal{L}_{\chi Vq} &= i\bar{\chi}\not{D}\chi - m_\chi\bar{\chi}\chi \\ &\quad -\frac{1}{2}\mathcal{V}^\dagger_{\mu\nu}\mathcal{V}^{\mu\nu} + m_V^2 V^\dagger_\mu V^\mu \\ &\quad +i\bar{q}\not{D}q - m_q\bar{q}q \\ &\quad -(d_1\bar{\chi}\gamma^\mu q V^\dagger_\mu + d_2\bar{\chi}\gamma^\mu\gamma^5 q V^\dagger_\mu + h.c.),\end{aligned} \tag{3.28}$$

where l_1, l_2, d_1 and d_2 are complex.

3. Vector DM

Here again we only have the case of a spin-$\frac{1}{2}$ mediated interaction between vector DM and quarks (again scalar and vector charged mediators aren't possible because they don't lead to Lorentz invariant and renormalizable interactions). The general Lagrangian is given by

$$\begin{aligned}\mathcal{L}_{XQq} &= -\frac{1}{2}\mathcal{X}^\dagger_{\mu\nu}\mathcal{X}^{\mu\nu} + m_X^2 X^\dagger_\mu X^\mu - \frac{\lambda_X}{2}(X^\dagger_\mu X^\mu)^2 \\ &\quad +i\bar{Q}\not{D}Q - m_Q\bar{Q}Q \\ &\quad +i\bar{q}\not{D}q - m_q\bar{q}q \\ &\quad -(y_3 X_\mu\bar{Q}\gamma^\mu q + y_4 X_\mu\bar{Q}\gamma^\mu\gamma^5 q + h.c.),\end{aligned} \tag{3.29}$$

where y_3 and y_4 are complex.

3.4 Non-relativistic Reduction of Simplified Models

After integrating out the heavy mediator we replace quark operators with nucleon operators (see appendix C), take the non-relativistic limit (see appendix B), and match onto the operators given in table 5.1. The results of this calculation are presented in terms of the c_i coefficients from [121], described in section 3.2, facilitating a straightforward computation of amplitudes and rates. The c_i's are given for each of

the WIMP spins in tables 3.2, 3.3 and 3.4. With this general framework in place we can now easily find the leading order NR operators for each distinct WIMP-nucleus interaction. One can imagine a series of minimal scenarios in which a combination of two Lagrangian couplings that give rise to a direct detection signal is non-zero with all others set to zero, and then proceeding in this manner for the entire set. Each of these scenarios is listed with its leading operators in table 3.5 and with all operators generated in table 3.6.

Table 3.2: Non-zero c_i coefficients for a spin-0 WIMP

	Uncharged Mediator	Charged Mediator
c_1	$\frac{h_1^N g_1}{m_\phi^2}$	$\frac{y_1^\dagger y_1 - y_2^\dagger y_2}{m_Q m_S} f_T^N$
c_{10}	$\frac{-ih_2^N g_1}{m_\phi^2} + \frac{2ig_4 h_4^N}{m_G^2}\frac{m_N}{m_S}$	$i\frac{y_2^\dagger y_1 - y_1^\dagger y_2}{m_Q m_S}\tilde{\Delta}^N$

Table 3.3: c_i coefficients for a spin-$\frac{1}{2}$ WIMP

	Uncharged Mediator	Charged Mediator
c_1	$\frac{h_1^N \lambda_1}{m_\phi^2} - \frac{h_3^N \lambda_3}{m_G^2}$	$\left(\frac{l_2^\dagger l_2 - l_1^\dagger l_1}{4m_\Phi^2} + \frac{d_2^\dagger d_2 - d_1^\dagger d_1}{4m_V^2}\right) f_T^N + \left(-\frac{l_2^\dagger l_2 + l_1^\dagger l_1}{4m_\Phi^2} + \frac{d_2^\dagger d_2 + d_1^\dagger d_1}{8m_V^2}\right)\mathcal{N}^N$
c_4	$\frac{4h_4^N \lambda_4}{m_G^2}$	$\frac{l_2^\dagger l_2 - l_1^\dagger l_1}{m_\Phi^2}\delta^N - \left(\frac{l_1^\dagger l_1 + l_2^\dagger l_2}{m_\Phi^2} + \frac{d_2^\dagger d_2 - d_1^\dagger d_1}{2m_V^2}\right)\Delta^N$
c_6	$\frac{h_2^N \lambda_2 m_N}{m_\phi^2 m_\chi}$	$\left(\frac{l_1^\dagger l_1 - l_2^\dagger l_2}{4m_\Phi^2} + \frac{d_2^\dagger d_2 - d_1^\dagger d_1}{4m_V^2}\right)\frac{m_N}{m_\chi}\tilde{\Delta}^N$
c_7	$\frac{2h_4^N \lambda_3}{m_G^2}$	$\left(\frac{l_1^\dagger l_2 - l_2^\dagger l_1}{2m_\Phi^2} + \frac{d_1^\dagger d_2 + d_2^\dagger d_1}{4m_V^2}\right)\Delta^N$
c_8	$-\frac{2h_3^N \lambda_4}{m_G^2}$	$\left(\frac{l_1^\dagger l_2 - l_2^\dagger l_1}{2m_\Phi^2} - \frac{d_1^\dagger d_2 + d_2^\dagger d_1}{4m_V^2}\right)\mathcal{N}^N$
c_9	$-\frac{2h_4^N \lambda_3 m_N}{m_\chi m_G^2} - \frac{2h_3^N \lambda_4}{m_G^2}$	$\left(\frac{l_1^\dagger l_2 - l_2^\dagger l_1}{2m_\Phi^2} - \frac{d_1^\dagger d_2 + d_2^\dagger d_1}{4m_V^2}\right)\mathcal{N}^N - \left(\frac{l_1^\dagger l_2 - l_2^\dagger l_1}{2m_\Phi^2} - \frac{d_1^\dagger d_2 + d_2^\dagger d_1}{4m_V^2}\right)\frac{m_N}{m_\chi}\Delta^N$
c_{10}	$\frac{h_2^N \lambda_1}{m_\phi^2}$	$i\left(\frac{l_1^\dagger l_2 - l_2^\dagger l_1}{4m_\Phi^2} + \frac{d_2^\dagger d_1 - d_1^\dagger d_2}{4m_V^2}\right)\tilde{\Delta}^N - i\frac{l_1^\dagger l_2 - l_2^\dagger l_1}{m_\Phi^2}\delta^N$
c_{11}	$-\frac{h_1^N \lambda_2 m_N}{m_\phi^2 m_\chi}$	$i\left(\frac{l_2^\dagger l_1 - l_1^\dagger l_2}{4m_\Phi^2} + \frac{d_2^\dagger d_1 - d_1^\dagger d_2}{4m_V^2}\right)\frac{m_N}{m_\chi} f_T^N + i\frac{l_1^\dagger l_2 - l_2^\dagger l_1}{m_\Phi^2}\frac{m_N}{m_\chi}\delta^N$
c_{12}	0	$\frac{l_2^\dagger l_1 - l_1^\dagger l_2}{m_\Phi^2}\delta^N$

As described earlier, we find that it is important to consider operators beyond those incorporated into the standard spin-independent and spin-dependent formal-

Table 3.4: c_i coefficients for a spin-1 WIMP

	Uncharged Mediator	Charged Mediator
c_1	$\frac{b_1 h_1^N}{m_\phi^2}$	$\frac{y_3^\dagger y_3 - y_4^\dagger y_4}{m_Q m_X} f_T^N$
c_4	$\frac{4\mathrm{Im}(b_7)h_4^N}{m_G^2} + i\frac{q^2}{m_X^2}\frac{\mathrm{Re}(b_7)h_4^N}{m_G^2} - \frac{q^2}{m_X m_N}\frac{\mathrm{Re}(b_6)h_3^N}{m_G^2}$	$2\frac{y_3^\dagger y_3 - y_4^\dagger y_4}{m_Q m_X}\delta^N$
c_5	$\frac{\mathrm{Re}(b_6)h_3^N}{m_G^2}\frac{m_N}{m_X}$	0
c_6	$\frac{\mathrm{Re}(b_6)h_3^N}{m_G^2}\frac{m_N}{m_X} - i\frac{\mathrm{Re}(b_7)h_4^N}{m_G^2}\frac{m_N^2}{m_X^2}$	0
c_8	$\frac{2\mathrm{Im}(b_7)h_3^N}{m_G^2}$	0
c_9	$-\frac{2\mathrm{Re}(b_6)h_4^N}{m_G^2}\frac{m_N}{m_X} + \frac{2\mathrm{Im}(b_7)h_3^N}{m_G^2}$	0
c_{10}	$\frac{b_1 h_2^N}{m_\phi^2} - \frac{3b_5 h_4^N}{m_G^2}\frac{m_N}{m_X}$	$i\frac{y_4^\dagger y_3 - y_3^\dagger y_4}{m_Q m_X}\tilde{\Delta}^N$
c_{11}	$\frac{\mathrm{Re}(b_7)h_3^N}{m_G^2}\frac{m_N}{m_X}$	$i\frac{y_4^\dagger y_3 - y_3^\dagger y_4}{m_Q m_X}\delta^N$
c_{12}	0	$2i\frac{y_3^\dagger y_4 - y_4^\dagger y_3}{m_Q m_X}\delta^N$
c_{14}	$-\frac{2\mathrm{Re}(b_7)h_4^N}{m_G^2}\frac{m_N}{m_X}$	0
c_{17}	$-\frac{4\mathrm{Im}(b_6)h_3^N}{m_G^2}\frac{m_N}{m_X}$	0
c_{18}	$\frac{4\mathrm{Im}(b_6)h_4^N}{m_G^2}\frac{m_N}{m_X}$	$-2i\frac{y_4^\dagger y_3 - y_3^\dagger y_4}{m_Q m_X}\delta^N$

ism, i.e. simple models exist in which one would infer an incorrect rate in current experiments by not including these effects. Also importantly, not all of the NR operators are actually generated at leading order; for example, the operators $\mathcal{O}_2$, $\mathcal{O}_3$, $\mathcal{O}_{13}$ and $\mathcal{O}_{15}$ are missing at leading order. Note that we only consider renormalizable Lagrangians, higher order non-renormalizable operators, which are presumably further suppressed, could be used to generate anapole interactions [123].

While spin independent interactions are a generic feature of direct couplings to quarks in our charged mediator cases, it is sometimes possbile to suppress them. In the scalar (and vector) WIMP with charged mediator cases, it is possible to suppress the spin independent interaction by ensuring that $|y_1| = |y_2|(|y_3| = |y_4|)$ while keep-

ing their relative phases non-zero (or π). While these non-minimal scenarios require some fine tuning we include it for completeness and label them y_1, y_2 and y_3, y_4.

Aside from scalar WIMPs, each particular spin produces some non-relativistic operators that are unique to that spin. Also, importantly, the operators $\mathcal{O}_1$ and $\mathcal{O}_{10}$ are generic to all spins. In five cases relativistic operators generate unique non-relativistic operators at leading order. Therefore distinguishing WIMP scenarios in these cases reduces to experimentally discerning between these operators (see also [126]). Given the likely low statistics of any detection in upcoming direct detection experiments, sub-leading operators are not likely to contribute enough to provide any further discriminating power.

3.5 Observables

The principle observable in direct detection experiments is the differential event rate. Since the incoming WIMPs originate in the galactic halo, one must average over the WIMP velocity distribution, $f(v)$, which we assume for the purposes of this paper to be Maxwell-Boltzmann,

$$\frac{dR}{dE_R} = N_T \frac{\rho_\chi M}{2\pi m_\chi} \int_{v_{min}} \frac{f(v)}{v} P_{tot} dv \tag{3.30}$$

where we use the value $\rho_\chi = 0.3\text{GeV/cm}^3$ for the local dark matter density, N_T is the number of nuclei in the target and P_{tot} can be calculated from the amplitude $\mathcal{M}$ in Eq. 3.14

$$P_{tot} = \frac{1}{2j_\chi + 1} \frac{1}{2j_N + 1} \sum_{spins} |\mathcal{M}|^2. \tag{3.31}$$

Thoughout this work we use the mathematica package supplied in [121] to calculate rates. To determine the leading order operator which arises from a given relativistic

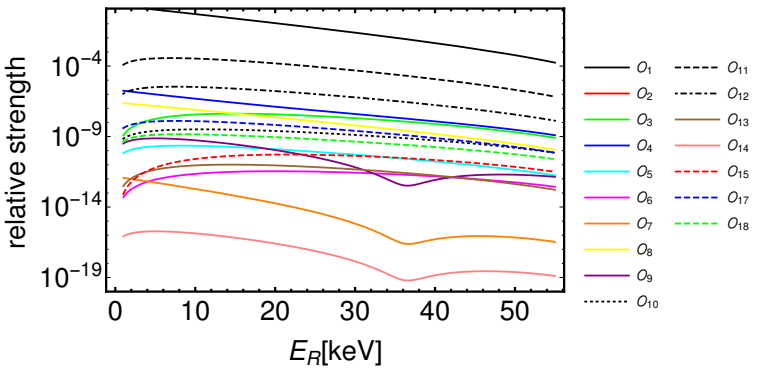

Figure 3.1: The relative strength of event rates of the non-relativistic operators from table 5.1

scenario we first plot the relative rate in xenon-131 for each of the NR operators with the same coefficient and normalized the rate to that of $\mathcal{O}_1$, see Fig. 3.5. Since the operators are zero, first and second order in momentum transfer, q, the relative strengths of the operators span 16 orders of magnitude. This is an important point to keep in mind when finding the leading operator, as sometimes a higher order term from the non-relativistic reduction can dominate. For example in the $b_7^{\mathrm{Re}} h_4$ scenario, expanding to higher order one finds $q^2\mathcal{O}_4$ still dominates over the $\mathcal{O}_6$ and $\mathcal{O}_{14}$ which contain powers of q within the operators.

Since the Lagrangians we have considered are not tied to specific complete and consistent particle physics models, the mediator masses are not fixed in advance and thus specific event rates are not predicted in advance. Clearly one requires a rate that is low enough to evade the current experimental constraints. For example, a 50 GeV WIMP producing 10 events per tonne per year is sufficiently low to evade the bounds from LUX [96].. For demonstration purposes we set the couplings to 0.1 in the various Lagrangians and find a mediator mass that will produce 10 events/t/y in the signal region for xenon ($5-45$keV). The calculated masses are given in table 3.5. It is perhaps telling that the mediator masses span 6 orders of magnitude, from just a few GeV up to a PeV. While it is unlikely that a full model of thermal relic dark matter

could be built around all of these Lagrangians, it is nevertheless a useful metric to estimate the relative strength of the different nuclear responses to each of the operators.

In Figs. 3.2, 3.3, 3.4 and 3.5 we have plotted rates for two common targets. For simplicity and again for demonstration purposes, we only plot the rates for a single isotope of both germanium and xenon. The choice of isotopes, ^{73}Ge and ^{131}Xe, was made to ensure sensitivity to spin-dependent responses. As can be seen in the figures, many operators produce rates with similar recoil energy dependence in the same target, but different nuclei can have very different responses to the various operators [18]. Thus a complementary choice of nuclear targets can provide important discriminating information.

To illustrate this discriminating power we plot the ratio of the rates in xenon and germanium in Fig. 3.5 and 3.6. We choose to only present ratios for the uncharged mediator cases of spinor and vector WIMPs since the other cases produce trival results (all operators being spin independent). To estimate the effect astrophysical uncertainties will have on discriminating between operators, we plot the rate for a range of astrophysical parameters from $v_0 = 200$m/s, and $v_{esc} = 500$m/s (lower) to $v_0 = 240$m/s and $v_{esc} = 600$m/s (upper). The uncertainty in the dark matter density does not appear since we are considering the ratio of rates. Given the vastly different energy dependence of the ratio of rates of each scenario the astrophysical errors do not completely inhibit their identification. Furthermore, operators $\mathcal{O}_9$ and $\mathcal{O}_{14}$, produced in scenarios $h_4 b_7^{\mathrm{Re}}$ and $h_4 b_6^{\mathrm{Re}}$ respectively, remain indistingushable when considering the ratio of rates. While it appears that in principle almost every operator is discernible, in practice isotopically impure targets and low statistics will further complicate the situation and provide limits on practical discrimination.

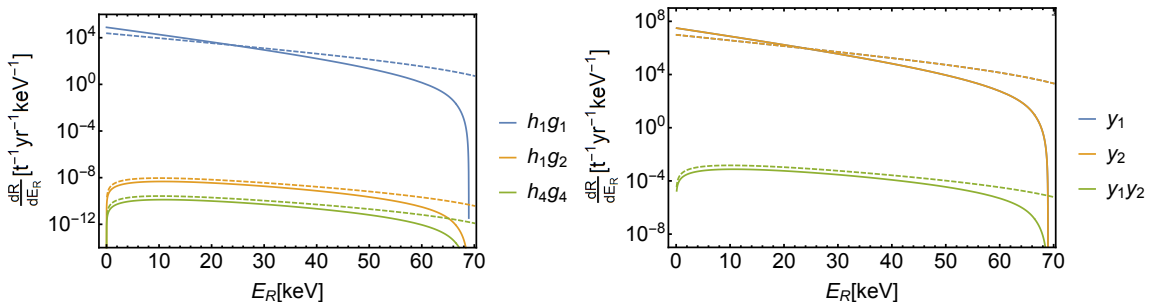

Figure 3.2: Rates for a 50GeV spin-0 WIMP in xenon (solid) and germanium (dashed) with uncharged (left) and charged mediators (right), assuming mediator mass of 1TeV and $\mathcal{O}(1)$ coupling constants.

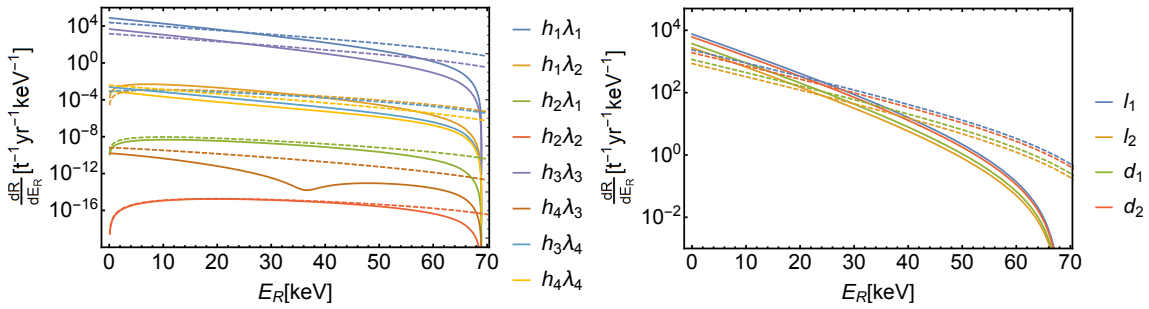

Figure 3.3: Rates for a 50GeV spin-$\frac{1}{2}$ WIMP in xenon (solid) and germanium (dashed) with uncharged (left) and charged mediators (right), assuming mediator mass of 1TeV and $\mathcal{O}(1)$ coupling constants.

3.6 Conclusion

The analysis we have given here builds on previous analyses to provide, in generality, a roadmap to use event rates in direct dark matter detectors to constrain fundamental dark matter models. We have outlined the steps needed to go from fundamental Lagrangians, first to relativistic operators, then reduce these to non-relativistic operators, and finally produce nuclear matrix elements. In the process several significant facts have been elaborated.

- Not all possible non-relativistic operators contributing to nuclear matrix elements in direct detection will arise from simple UV complete dark matter models.

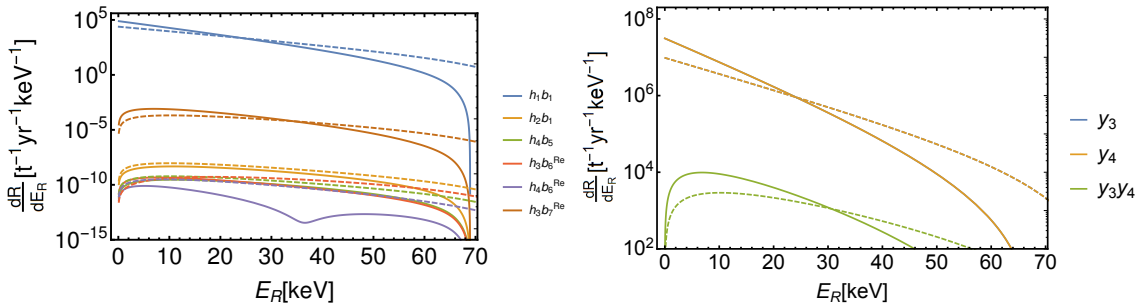

Figure 3.4: Rates for a 50GeV spin-1 WIMP in xenon (solid) and germanium (dashed) with uncharged (left) and charged mediators (right), assuming mediator mass of 1TeV and $\mathcal{O}(1)$ coupling constants.

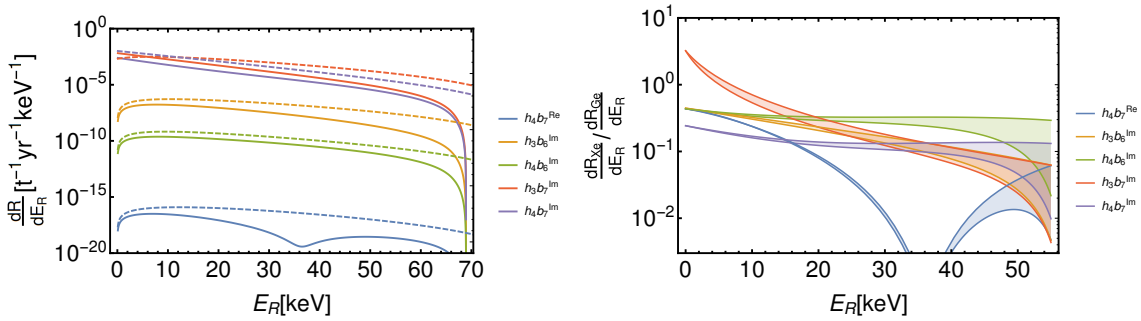

Figure 3.5: Rates (left) for a 50GeV spin-1 WIMP in xenon (solid) and germanium (dashed) with uncharged mediators and imaginary couplings, assuming mediator mass of 1TeV and $\mathcal{O}(1)$ coupling constants. Also shown is the ratio of rates in xenon and germanium (right).

- Aside from scalar WIMPs each particular spin produces some non-relativistic operators that are unique to that spin.
- Two non-relativistic operators, $\mathcal{O}_1$ and $\mathcal{O}_{10}$, are ubiquitous and arise for all WIMP spins we have explored.
- In 5 scenarios relativistic operators generate unique non-relativistic operators at leading order.
- Two new non-relativistic operators not previously considered arise at low energies if spin-1 WIMP dark matter is allowed for.
- While the different operators that can contribute to event rates in detectors using specific elements or isotopes cannot be distinguished on the basis of their impact on the differential event rates in these detectors, they can produce rad-

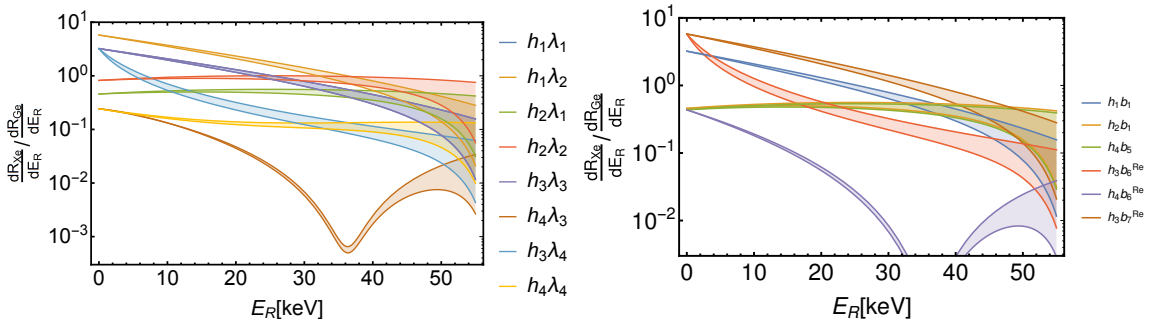

Figure 3.6: Ratio of rates in xenon and germanium, illustrating the discriminating power of having multiple nuclear targets. For a 50GeV spin-$\frac{1}{2}$ WIMP with uncharged mediator (left) and a 50GeV spin-1 WIMP with uncharged mediator (right), the shaded regions show the upper and lower bounds due to the astrophysical parameters

ically different energy dependence for scattering off different nuclear targets. Thus, a complementary use of different target materials will be necessary to reliably distinguish between different particle physics model possibilities for WIMP dark matter.

While current detectors have only yielded upper limits, with new generations of larger detectors with greater energy resolution and lower thresholds coming online, the search for WIMP dark matter has never been so vibrant and promising. The tools we have provided here should help experimenters to probe the most useful parameter space, to interpret any non-zero signals in terms of constraints on fundamental models, and should allow theorists who build fundamental models to frame predictions in an accurate and simple way so that they might be directly compared with experiment.

Table 3.5: Leading order operators which can arise from the relativistic Lagrangians considered in this work, the column '$\mathcal{L}$ terms' gives the non-zero couplings for that scenario. Each row represents a possible leading order direct detection signal. A '*' indicates that the mediator is charged. The 'Eqv. M_m' column gives the mediator mass required for each scenario to produce $\sim$10 events $t^{-1}yr^{-1}keV^{-1}$ in xenon, with couplings set to 0.1.

WIMP spin	Mediator spin	$\mathcal{L}$ terms	leading NR operator	Eqv. M_m
0	0	h_1, g_1	$\mathcal{O}_1$	13 TeV
0	0	h_2, g_1	$\mathcal{O}_{10}$	14 GeV
0	1	h_4, g_4	$\mathcal{O}_{10}$	8 GeV
0	$\frac{1}{2}^*$	y_1	$\mathcal{O}_1$	3.2 PeV
0	$\frac{1}{2}^*$	y_2	$\mathcal{O}_1$	3.2 PeV
0	$\frac{1}{2}^*$	y_1, y_2	$\mathcal{O}_{10}$	41 GeV
$\frac{1}{2}$	0	h_1, λ_1	$\mathcal{O}_1$	12.7 TeV
$\frac{1}{2}$	0	h_2, λ_1	$\mathcal{O}_{10}$	293 GeV
$\frac{1}{2}$	0	h_1, λ_2	$\mathcal{O}_{11}$	14 GeV
$\frac{1}{2}$	0	h_2, λ_2	$\mathcal{O}_6$	1.9 GeV
$\frac{1}{2}$	1	h_3, λ_3	$\mathcal{O}_1$	6.3 TeV
$\frac{1}{2}$	1	h_4, λ_3	$\mathcal{O}_9$	6.4 GeV
$\frac{1}{2}$	1	h_3, λ_4	$\mathcal{O}_8$	180 GeV
$\frac{1}{2}$	1	h_4, λ_4	$\mathcal{O}_4$	135 GeV
$\frac{1}{2}$	0*	l_1	$\mathcal{O}_1$	7.1 TeV
$\frac{1}{2}$	0*	l_2	$\mathcal{O}_1$	5.5 TeV
$\frac{1}{2}$	1*	d_1	$\mathcal{O}_1$	5.9 TeV
$\frac{1}{2}$	1*	d_2	$\mathcal{O}_1$	6.7 TeV
1	0	h_1, b_1	$\mathcal{O}_1$	13 TeV
1	0	h_2, b_1	$\mathcal{O}_{10}$	10 GeV
1	1	h_4, b_5	$\mathcal{O}_{10}$	5.1 GeV
1	1	$h_3, b_6^{\mathrm{Re}}(b_6^{\mathrm{Im}})$	$\mathcal{O}_5(\mathcal{O}_{17})$	5.5 GeV(23 GeV)
1	1	$h_4, b_6^{\mathrm{Re}}(b_6^{\mathrm{Im}})$	$\mathcal{O}_9(\mathcal{O}_{18})$	3 GeV(4.6 GeV)
1	1	$h_3, b_7^{\mathrm{Re}}(b_7^{\mathrm{Im}})$	$\mathcal{O}_{11}(\mathcal{O}_8)$	186 GeV(228 GeV)
1	1	$h_4, b_7^{\mathrm{Re}}(b_7^{\mathrm{Im}})$	$\mathcal{O}_4(\mathcal{O}_4)$	78 MeV (172 GeV)
1	$\frac{1}{2}^*$	y_3	$\mathcal{O}_1$	3.2 PeV
1	$\frac{1}{2}^*$	y_4	$\mathcal{O}_1$	3.2 PeV
1	$\frac{1}{2}^*$	y_3, y_4	$\mathcal{O}_{11}$	120 TeV

Table 3.6: List of scenarios with leading operators colored by which are distinguishable via the ratio $\frac{dR_{Xe}}{dE}/\frac{dR_{Ge}}{dE}$, * indicates the imaginary part of that coupling.

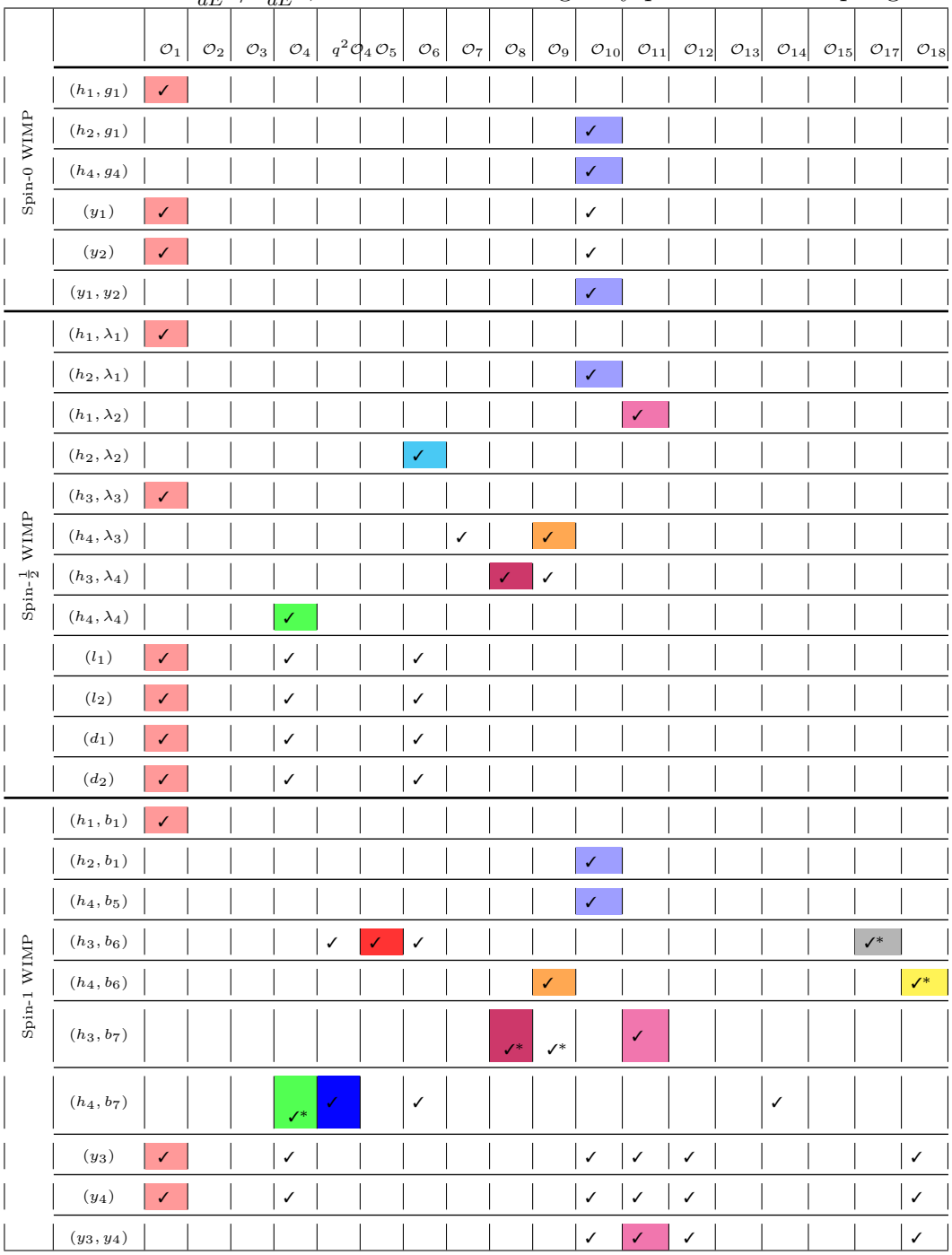

Chapter 4

SIMPLIFIED MODEL RECONSTRUCTIONS

4.1 Introduction

In the previous chapter it was established that direct detection experiments have some discriminating power in determining the NR-EFT operator responsible for the scattering. In this chapter we will quantify how well various experimental setups can distinguish operators under realistic circumstances. Similar works have been performed in [127, 126], the analysis here will improve upon them in a few ways. In [126] the primary concern was placed upon parameter estimation, and the parameter space considered included the full complement of NR operators. Whereas here the emphasis will be upon model selection and will be restricted to a subset of relevant operators found in the previous chapter. In [127], the models considered were somewhat arbitrary and only cover a subset of well motivated NR operators, and then carries out a Bayesian model selection analysis. However, applying Bayesian methods in this case weakens their interpretation in terms of probabilities because they do not have a complete parameter space. Instead they are able to show with what frequency they obtain the correct model, making this a hybrid frequentist-Bayesian approach. In this chapter only the operators generated from the simplified models considered in the previous chapter will be considered. As a proof of concept, only the spin-$\frac{1}{2}$ WIMP model will be treated and the remainder left to future work. Model selection will be carried out using the Bayes factor as laid out in the proceding section.

4.2 Statistical Framework

Bayesian statistics provides a method for model selection with a clear probablistic interpretation. This is in contrast to frequentist based tests which have a purely frequency based interpretation. For example in a discovery test, which attempts to reject the null hypothesis in favor of the signal hypothesis. With this method one can claim to reject the null hypothesis at 5σ, meaning that fewer than 1 in a million such experiments would produce a statistical fluctuation great enough to mimic the observation. When performing model selection with Bayesian statistics the figure of merit considered is called the Bayes factor. Introduced by Jeffreys in 1935, the Bayes factor, K, is constructed from the model evidence (the denominator of Bayes theorem Eq. 2.25),

$$K = \frac{\epsilon(D, M_1)}{\epsilon(D, M_2)}. \tag{4.1}$$

Since Bayes theorem gives a normalized probability distribution, it is possible to determine the evidence via an integral over the model parameter space, θ_1,

$$\epsilon(D, M_1) = \int \mathcal{L}(D|\theta_1, M_1)\pi(\theta_1, M_1)d\theta_1. \tag{4.2}$$

The likelihood function will take the same binned poisson form as given in Eq. 2.24 and log priors will be assumed. Jeffreys considered a $K > 10$ to be in strong favor of M_1 and $K > 100$ as decisive evidence for M_1 [128]. These thresholds will be used to quantify the ability for direct detection experiments to discern models in the following simulations.

An alternative method for model selection can be obtained through marginalization. If one has a complete set of competing models, $\mathcal{M} = \{M_1, M_2, ...\}$, then they form a larger parameter space of discrete hypotheses, $\Theta = \{\theta_1, \theta_2, ...\}$. Marginalizing

over the sub-parameter space of a model will give the total posterior probability of that model:

$$P(M_1|D) = \int_{\theta_1} \frac{\mathcal{L}(D|\Theta, \mathcal{M})\pi(\Theta, \mathcal{M})}{\epsilon(D, \mathcal{M})} d\Theta. \tag{4.3}$$

This method is more computationally intensive and thus will be explored in a future work.

4.3 The Models

In this analysis we identify a model, M_i, as a WIMP scattering via a single NR operator $\mathcal{O}_i$. The parameters of each model are the WIMP mass and operator coefficient: $\theta_i = \{m_\chi, c_i\}$. Starting with the spin-$\frac{1}{2}$ case, the full model parameter space and priors are given in table 4.1. In addition, the astrophysical uncertainties can be marginalized over to better account for our ignorance of their true values.

4.4 Model Comparison

Each model was simulated to produce 20, 200 and 2000 events in both a xenon and germanium detector. For this analysis a WIMP mass of 50GeV was used for every model. The exposure was abitrarily scaled to achieve the desired number of events within the energy ranges 0.1-40keV and 1-40keV for germanium and xenon respectively. Both detectors were assumed to be background free and no detector resolution effects were included. To sample the posterior probability distribution and calculate the model evidence, the MultiNest program will be used [74]. For each simulation scaled Bayes factors, $2\ln(K_{ij})$, are calculated for each model vs. the simulated model, the results for 20, 200 and 2000 events are given in tables 4.2, 4.3 and 4.4 respectively. Using the criteria of $2\ln(K_{ij}) < -4$ as decisive evidence in favor of model i, these

Table 4.1: Parameter space for spin-$\frac{1}{2}$ WIMP

Parameter	Range	Prior
m_χ	$1 - 10^3$ GeV	log
c_1	$10^{-10} - 10^4$ GeV^{-2}	log
c_4	$10^{-10} - 10^4$ GeV^{-2}	log
c_5	$10^{-10} - 10^4$ GeV^{-2}	log
c_6	$10^{-10} - 10^4$ GeV^{-2}	log
c_8	$10^{-10} - 10^4$ GeV^{-2}	log
c_9	$10^{-10} - 10^4$ GeV^{-2}	log
c_{10}	$10^{-10} - 10^4$ GeV^{-2}	log
c_{11}	$10^{-10} - 10^4$ GeV^{-2}	log
ρ_χ	0.3 ± 0.1GeV/cm^3	gaussian
v_0	220 ± 20km/s	gaussian
v_{esc}	544 ± 40km/s	gaussian

results indicate that after even 20 events some models are strongly disfavored. At 200 events it can be seen that some degeneracy still exists. It is not until 2000 events have been recorded that all models can be diserned from each other (except when simulating $\mathcal{O}_8$, which can still be confused with $\mathcal{O}_1$).

Table 4.2: Bayes factors for 20 events

Sim	$K_{i,1}$	$K_{i,4}$	$K_{i,5}$	$K_{i,6}$	$K_{i,8}$	$K_{i,9}$	$K_{i,10}$	$K_{i,11}$
$\mathcal{M}_1$	0	0.0298	-8.21	-29.	-0.285	-7.17	-9.54	-8.35
$\mathcal{M}_4$	-0.515	0	-9.81	-32.8	-0.797	-8.55	-10.7	-10.1
$\mathcal{M}_5$	-17.5	-19.9	0	-9.37	-15.0	-3.28	-4.0	0.0803
$\mathcal{M}_6$	-70.4	-72.4	-19.6	0	-66.3	-45.2	-7.53	-20.6
$\mathcal{M}_8$	0.301	0.0341	-7.85	-27.4	0	-6.42	-9.65	-8.18
$\mathcal{M}_9$	-7.59	-9.84	-2.83	-14.7	-6.19	0	-7.59	-3.04
$\mathcal{M}_{10}$	-29.4	-30.9	-3.35	-5.43	-26.9	-14.2	0	-2.91
$\mathcal{M}_{11}$	-16.2	-18.5	-0.196	-8.65	-14.1	-3.25	-3.68	0

Table 4.3: Bayes factors for 200 events

Sim	$K_{i,1}$	$K_{i,4}$	$K_{i,5}$	$K_{i,6}$	$K_{i,8}$	$K_{i,9}$	$K_{i,10}$	$K_{i,11}$
$\mathcal{M}_1$	0	-2.12	-72.1	-241.	-1.32	-73.	-80.8	-77.4
$\mathcal{M}_4$	-3.51	0	-95.5	-281.	-4.44	-95.5	-99.5	-102.
$\mathcal{M}_5$	-172.	-195.	0	-49.2	-150.	-29.6	-25.9	0.68
$\mathcal{M}_6$	-702.	-720.	-194.	0	-665.	-454.	-72.5	-205.
$\mathcal{M}_8$	0.686	-1.3	-68.4	-230.	0	-67.2	-80.9	-74.3
$\mathcal{M}_9$	-78.1	-101.	-11.5	-80.	-65.6	0	-46.7	-16.5
$\mathcal{M}_{10}$	-289.	-305.	-31.3	-22.3	-267.	-139.	0	-26.2
$\mathcal{M}_{11}$	-160.	-184.	-1.55	-40.4	-141.	-29.6	-18.6	0

Table 4.4: Bayes factors for 2000 events

Sim	$K_{i,1}$	$K_{i,4}$	$K_{i,5}$	$K_{i,6}$	$K_{i,8}$	$K_{i,9}$	$K_{i,10}$	$K_{i,11}$
$\mathcal{M}_1$	0	-27.7	-742.	-2,130	-4.26	-765.	-800.	-800.
$\mathcal{M}_4$	-29.2	0	-977.	-1.99×10^5	-31.	-991.	-998.	-1050
$\mathcal{M}_5$	-1.99×10^5	-1.99×10^5	0	-371.	-1510	-301.	-186.	-4.04
$\mathcal{M}_6$	-6820	-1.99×10^5	-1900	0	-6640	-4510	-705.	-2040
$\mathcal{M}_8$	-2.29	-28.7	-714.	-1.99×10^5	0	-724.	-799.	-773.
$\mathcal{M}_9$	-748.	-963.	-71.	-588.	-665.	0	-333.	-99.4
$\mathcal{M}_{10}$	-910.	-2940	-225.	-170.	-2670	-1380	0	-237.
$\mathcal{M}_{11}$	-1520	-483.	-6.36	-220.	-1420	-298.	-302.	0

Chapter 5

EFFECTIVE FIELD THEORY TREATMEANT OF THE NEUTRINO FLOOR

5.1 Introduction

For over two decades, direct dark matter detection experiments have made great progress in searching for dark matter in the form of Weakly Interacting Massive Particles (WIMPs). The most stringent bounds now constrain the spin-independent and spin dependent WIMP-nucleon direct detection cross sections to be less than $\sim 10^{-46}$ cm^2 [13] and $\sim 10^{-39}$ cm^2 [129] respectively. Larger scale detectors in development are expected to further improve the cross section bounds by 2-3 orders of magnitude [130, 131]. From a theoretical perspective, experiments are now probing dark matter that interacts with nucleons through tree-level Higgs exchange.

A theoretical interpretation of the experimental limits depends on a detailed modeling of the WIMP-nucleus interaction. The WIMP-nucleus interaction is traditionally approximated by multiplying the cross section at zero-momentum transfer, i.e. the point nucleus model, by the form factor, which represents the extended structure of the nucleus and encodes the momentum dependence of the interaction [12, 132]. The WIMP-nucleon interaction is approximated as a sum of a spin-independent (SI) and spin-dependent (SD) cross section. The SI interaction is coherent on the nucleus, leading to an enhanced sensitivity, so that current experimental limits on the SI interaction are much stronger than on the SD interaction.

In a series of recent papers, this standard theoretical formalism has been generalized within a non-relativistic effective field theory (EFT) model for the nucleus, in which the WIMP interacts with a nucleon via a larger sample of operators [18, 121].

Additional nuclear responses were identified that augment the standard SI and SD responses. Though these operators induce nuclear recoil energy spectra that differ from the traditional SI/SD models [120], the upper limits on the WIMP-nucleon cross section are not strongly affected, except for experiments with relatively high recoil energy thresholds, greater than tens of keV [123]. The non-relativistic EFT formalism also provides unique signatures in direct detection experiments with directional sensitivity [133, 134].

Larger volume, next generation direct dark matter searches that detect WIMPs only via the energy deposition from the WIMP to the nucleus will be affected by a background from neutrinos produced in the Sun, atmosphere, and diffuse supernovae [135, 136, 30]. Neutrinos from these sources will interact primarily with nuclei through the coherent scattering process, which is induced by neutrinos with energies of tens of MeV. Considering the nuclear recoil energy spectrum alone, within the traditional SI/SD formalism Solar neutrinos mimic a WIMP with mass ~ 6 GeV, while atmospheric neutrinos mimic a WIMP with mass ~ 100 GeV [30, 137].

Identifying and reducing the neutrino backgrounds presents a significant challenge for direct detection experiments, in particular those which strive to reach the ton scale and beyond. Several recent studies have discussed methods to distinguish WIMPs from neutrinos in next generation detectors. Ruppin et al. discussed the prospects for exploiting the complementarity between detectors that use different nuclear targets to detect energy deposition, considering both SI and SD interactions [137]. Davis [138] considered the difference between time variation of the WIMP signal, due to the well-known annual modulation [139] from the rotation of the Earth around the Sun, and the Solar neutrino signal, which is due to the small but non-zero eccentricity of the Earth's orbit around the Sun. These time variations generate a phase difference between the Solar neutrino and the WIMP signal. Grothaus [140] and O'Hare et

al. [141] discussed the prospects for exploiting the difference in the direction of the nuclear recoil energy induced by the WIMPs and Solar neutrinos. For these timing and directional-based techniques, an exposure on the scale of 100 tonne years is required to distinguish the Solar neutrino background from a WIMP signal.

In this paper, we calculate the expected WIMP signal in future detectors using the non-relativistic EFT formalism of [18], and compare to the predictions of the astrophysical neutrino backgrounds. For each of the operators that describe the WIMP coupling to the nucleons within EFT, and for a wide range of WIMP masses, we compare the nuclear recoil energy spectrum to the neutrino backgrounds. Using the nuclear recoil energy spectrum, we categorize the operators that both can and cannot be distinguished from the neutrino backgrounds. We find that the majority of the operators can in fact be distinguished from the neutrino backgrounds over the entire WIMP mass range. For the few operators that cannot be distinguished, we identify the specific WIMP mass that best matches the neutrino background, and highlight the scatter in this best matching mass between the operators. Our results imply, for detectors with good nuclear recoil energy resolution, that signals are more easily distinguished from the neutrino background in some cases of non-standard WIMP scattering (not SI/SD scattering).

This paper is organized as follows. In Section 5.2 we briefly review both the physics of non-relativistic EFT and of neutrino coherent scattering. In Section 5.3 we calculate the nuclear recoil spectra for EFT operators, and identify the operators that induce nuclear recoils that mimic the neutrino backgrounds. In Section 5.4 we calculate the discovery limit for each operator in light of the neutrino background, and show that many of the operators can in fact be distinguished from the neutrino background over a wide range of masses. In Section 5.5, we present our summary and conclusions.

5.2 WIMP and Neutrino Scattering with Nuclei

In this section we review the WIMP-nucleus and the neutrino-nucleus scattering formalism that is required for our analysis. For WIMP-nucleus scattering, we describe the necessary ingredients of non-relativistic EFT, while for neutrino-nucleus scattering we describe the cross section that is predicted in the Standard Model.

5.2.1 Non-relativistic EFT WIMP-nucleus Scattering

Dark matter-nucleus scattering is expected to occur due to the presence of a dark matter distribution in our galaxy, with the interaction rate being sensitive to both the local dark matter density (for reviews of observations and theoretical models of the local density see for example [142, 143]) and the velocity distribution of the dark matter, as well as the nuclear properties of the target material. The precise form of the velocity distribution is unknown, but can be modeled using N-body simulations [144, 145]. The speed of the dark matter is predicted to be in the $\mathcal{O}$(few 100km/s) region, with an upper limit corresponding to the galactic escape velocity (the RAVE survey gave a value of 533^{+54}_{-41} km/s at 90% confidence [146]). Standard momentum exchanged in such collisions is in the MeV range, which lends direct detection interactions to a non-relativistic effective field theory treatment for mediator particles with masses above this value, which is the case for a large variety of dark matter models.

Traditionally WIMP-nucleus scattering has been formulated as an incident dark matter particle scattering off a nucleus through either SI or SD interactions. However, as theoretical investigations into the particle nature of dark matter have broadened in scope to include a more general set of interactions, including a variety of velocity and momentum dependence, it has been recognized that the SI/SD interaction categorization insufficiently captures the range of the possible relevant interaction properties.

Importantly, not including the full array of interactions and nuclear responses could lead to a misinterpretation of any future direct detection observations if carried out within the conventional framework [147].

Following standard semi-leptonic electroweak treatments of the nuclear physics involved in the WIMP-nucleus scattering, it has been shown [18, 121] that the SI and SD interactions are only a portion of a larger set of nuclear responses which must be considered for a proper consideration of direct detection studies. In addition to responses giving rise to SI (the vector charge nuclear operator) and SD interactions (which is a sum of two responses: the axial and longitudinal spin-dependent responses), there are also nuclear responses sensitive to orbital angular momentum and spin-orbit coupling. Different WIMP-nucleus scattering models will correspond to different nuclear responses, which often include a sum of responses contributing, and can also lead to interference terms between the responses [18, 148, 149]. A study of a variety of spin-1/2 dark matter UV complete models whose responses are described by these non-standard responses was given in [123], and a general survey of simplified models of spin-0, spin-1/2, and spin-1 dark matter models was carried out in [19]. There exist additional nuclear responses beyond these five, but are typically not considered due to P and CP properties of the nuclear ground state and an assumption of CP conservation of the interaction.

Within this general EFT framework, the WIMP-nucleus interaction is written as a sum over the individual WIMP-nucleon interactions [18], whose Lagrangian is of the form

$$\mathcal{L} = \sum_{\tau=0,1} \sum_{i=1}^{15} c_i^\tau \mathcal{O}_i t^\tau \tag{5.1}$$

where t^0 is the identity matrix, thus giving the isoscalar interaction, and t^1 is the third Pauli matrix giving the isovector interaction. It can be seen in general treatments

that interference effects can arise not only between operators giving rise to different nuclear responses but also between the same operators characterized by different c_i^τ and $c_i^{\tau'}$ [148, 149]. The coefficients c_i^τ can be related to the familiar neutron and proton couplings by

$$c_i^n = \frac{c_i^0 - c_i^1}{2} \quad ; \quad c_i^p = \frac{c_i^0 + c_i^1}{2} \tag{5.2}$$

The nucleon-level interactions arise from WIMP-quark interactions (either at the Lagrangian level including mediator particles, which are subsequently integrated out, or by directly writing down bi-linear terms suppressed by some high mass scale) where quarks are then embedded into the nucleons through standard techniques [150, 151, 152, 153], and all operators are treated non-relativistically.

We consider the operators in Table 5.1, with the exception of $\mathcal{O}_2$ which cannot be generated at leading order from Lorentz invariant relativistic operators [121]. There are two additional operators which need to be included if the WIMP under consideration has spin-1 [19], but for this work we are assuming a spin-1/2 dark matter particle. Assuming Galilean invariance (for a treatment which includes operators which are constrained by Lorentz invariance rather than Galilean invariance see Ref. [152]), time-reversal symmetry, and Hermiticity, these operators only depend on four quantities: the exchanged momentum, $\vec{q}$, in the dimension-less, Hermitian form $i\vec{q}/m_N$, the velocity $\vec{v}^\perp = \vec{v} + \vec{q}/2\mu_N$, where $\vec{v}$ is the WIMP velocity in the target nucleon rest frame and μ_N is the WIMP-nucleon reduced mass, the WIMP spin S_χ, and the nuclear spin S_N.

Although we retain the remaining 14 operators, it should be kept in mind that not all of these non-relativistic operators arise at leading order from simple UV models [19], and therefore may not be relevant when a complete Lagrangian picture of dark matter is formulated. Additionally the recoil response of the operators can vary

by many orders of magnitude on a given target material, and operator responses can vary greatly between various detector materials, which demonstrates the premium placed on target complementarity [18, 137, 17, 127].

Table 5.1: List of NR effective operators described in [121]

$\mathcal{O}_1$	$1_\chi 1_N$
$\mathcal{O}_2$	$(\vec{v}^\perp)^2$
$\mathcal{O}_3$	$i\vec{S}_N \cdot (\frac{\vec{q}}{m_N} \times \vec{v}^\perp)$
$\mathcal{O}_4$	$\vec{S}_\chi \cdot \vec{S}_N$
$\mathcal{O}_5$	$i\vec{S}_\chi \cdot (\frac{\vec{q}}{m_N} \times \vec{v}^\perp)$
$\mathcal{O}_6$	$(\frac{\vec{q}}{m_N} \cdot \vec{S}_N)(\frac{\vec{q}}{m_N} \cdot \vec{S}_\chi)$
$\mathcal{O}_7$	$\vec{S}_N \cdot \vec{v}^\perp$
$\mathcal{O}_8$	$\vec{S}_\chi \cdot \vec{v}^\perp$
$\mathcal{O}_9$	$i\vec{S}_\chi \cdot (\vec{S}_N \times \frac{\vec{q}}{m_N})$
$\mathcal{O}_{10}$	$i\frac{\vec{q}}{m_N} \cdot \vec{S}_N$
$\mathcal{O}_{11}$	$i\frac{\vec{q}}{m_N} \cdot \vec{S}_\chi$
$\mathcal{O}_{12}$	$\vec{S}_\chi \cdot (\vec{S}_N \times \vec{v}^\perp)$
$\mathcal{O}_{13}$	$i(\vec{S}_\chi \cdot \vec{v}^\perp)(\frac{\vec{q}}{m_N} \cdot \vec{S}_N)$
$\mathcal{O}_{14}$	$i(\vec{S}_N \cdot \vec{v}^\perp)(\frac{\vec{q}}{m_N} \cdot \vec{S}_\chi)$
$\mathcal{O}_{15}$	$-(\vec{S}_\chi \cdot \frac{\vec{q}}{m_N}) \left((\vec{S}_N \times \vec{v}^\perp) \cdot \frac{\vec{q}}{m_N}\right)$

5.2.2 Neutrino-nucleus Scattering

The theoretical prediction for neutrino interaction with the nucleus is much more simple than the WIMP interaction described above. Neutrino-nucleus coherent scattering is a straightforward prediction of the Standard Model, and has been theoreti-

cally studied for many years [154, 11]. The coherent cross section is

$$\frac{\mathrm{d}\sigma}{\mathrm{d}E_r}(E_r, E_\nu) = \frac{G_F^2}{4\pi} Q_W^2 m_N \left(1 - \frac{m_N E_r}{2E_\nu^2}\right) F^2(E_r)\,, \tag{5.3}$$

where $Q_W = \mathcal{N} - (1 - 4\sin^2\theta_W)\mathcal{Z}$ is the weak nuclear hypercharge of a nucleus with $\mathcal{N}$ neutrons and $\mathcal{Z}$ protons, G_F is the Fermi coupling constant, θ_W is the weak mixing angle and m_N is the target nucleus mass. There are few percent corrections to Equation 5.3 for non isoscalar nuclei ($\mathcal{N} \neq \mathcal{Z}$) arising from axial couplings [155]. In addition there is an angular dependence in the recoil direction of the nucleus which we do not consider in this paper.

5.3 Matching the WIMP and Neutrino Recoil Spectra

In this section we analyze the nuclear recoil spectrum that is induced by WIMPs within the non-relativistic EFT of [18], and by neutrinos through coherent scattering. We identify operators which admit recoil spectra that are degenerate with the neutrino backgrounds, and for these operators we find the corresponding WIMP masses that provide the "best-fit" which is defined below. We classify operators into groups based on their induced recoil spectra, and compare to the neutrino-induced spectra.

5.3.1 Best Fit Rates

We begin by matching the nuclear recoil spectra from the various WIMP-nucleon operators described above to the predicted Solar and atmospheric neutrino-induced recoil energy spectrum. For the Solar neutrinos, we consider the ^{8}B component. The predicted recoil energy spectra in dark matter detectors due to these neutrinos are taken from Refs. [136, 30]. To find the "best-fit" WIMP masses for a given operator we maximize the Poisson likelihood,

$$\mathcal{L}_{Poisson} = \prod_{i=1}^{b} \frac{\nu_i^{n_i} e^{\nu_i}}{n_i!} \tag{5.4}$$

where b is the number of nuclear recoil energy bins, n_i is the expected number of WIMP events and ν_i is the expected number of neutrino events in the bin. We consider several detector targets, which are indicated in Table 5.2 along with the corresponding nuclear energy recoil range. The recoil range is split into a low and high region, where the solar and non-solar neutrino backgrounds respectively dominate. For our likelihood analysis we choose an exposure such that we obtain 200 neutrino events for each target [30], binned into 16 energy bins.

Table 5.2: List of detector targets considered in this work

	low region (keV)	high region (keV)
xenon	0.003 - 3	4.0 - 100
germanium	0.0053 - 7	7.9 - 120
silicon	0.014 - 18	20 - 300
flourine	0.033 - 25	28 - 500

Figure 5.1 shows a sample of the best fitting WIMP-induced recoil energy spectra when comparing to the predicted ^{8}B spectrum, and Figure 5.2 shows a sample when comparing to the predicted atmospheric-induced recoil spectrum. In both figures we have used one operator representative from each group where the groups are defined in Table 5.3. As is shown for several operators, in particular $\mathcal{O}_1$, we find a good match to both the ^{8}B Solar and atmospheric spectra. This is quantified by the $\Delta\chi^2$ indicated in Figure 5.1 and 5.2, which is calculated as the negative log likelihood in Equation 5.4. Note that $\mathcal{O}_1$ ($\mathcal{O}_4$) from group 1 is the SI (SD) response used in the standard analyses, and our result agrees with previous results [30, 137].

On the other hand, the nuclear recoil spectra from many WIMP-nucleon operators are clearly distinct from the ^{8}B and atmospheric-induced neutrino spectra, even when taken at the best-fit WIMP masses. For example, as is indicated in Figures 5.1 and 5.2,

the $\mathcal{O}_6$ (belongs to group 3) and $\mathcal{O}_{10}$ (belongs to group 2) best fit WIMP mass gives a poor $\Delta\chi^2$ relative to the neutrino backgrounds. This indicates that for essentially all WIMP masses and cross sections, $\mathcal{O}_6$ and $\mathcal{O}_{10}$ can be distinguished from the neutrino backgrounds. We return to this point below when we discuss the evolution of the discovery limit.

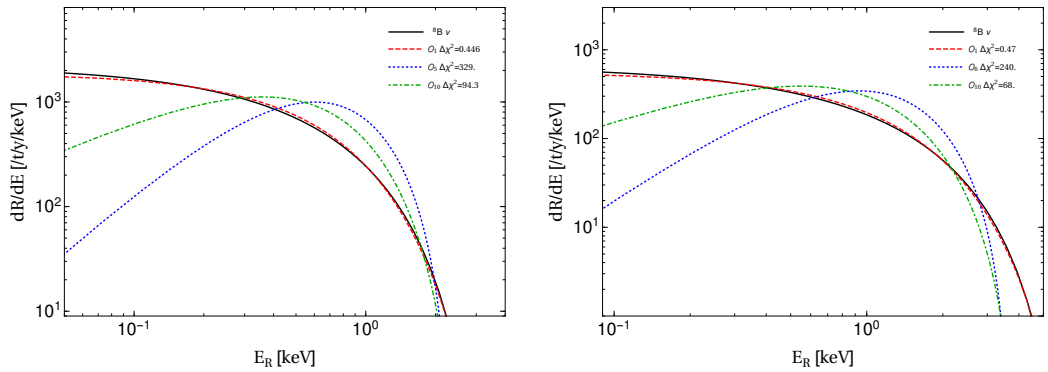

Figure 5.1: Sample maximum likelihood fits to the ^{8}B Solar neutrino-induced nuclear recoil event rate spectrum in Xenon (left) and Germanium (right). Three different operators are shown, one operator from each of the groupings in Table 5.3.

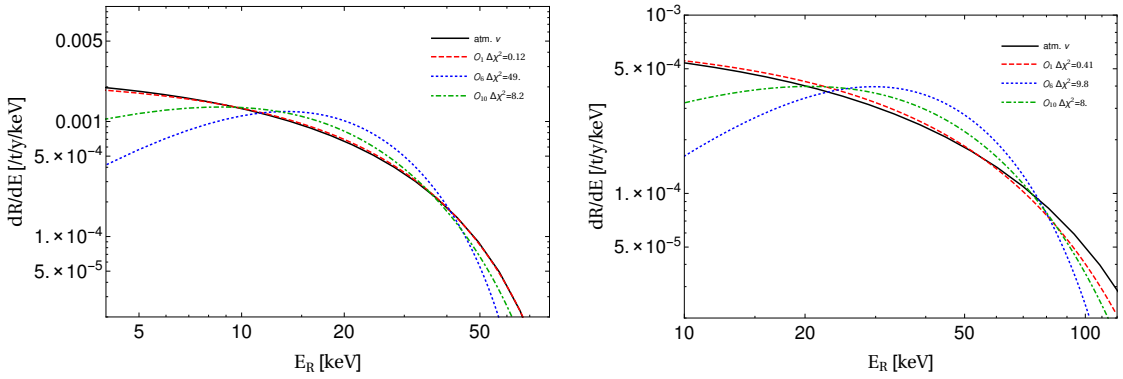

Figure 5.2: Sample maximum likelihood fits to the atmospheric neutrino-induced nuclear recoil event rate spectrum in xenon (left) and germanium (right). The same operators are used here as in Figure 5.1.

The WIMP masses that provide the best fit to the ^{8}B recoil spectrum for the operators $\mathcal{O}_1$, $\mathcal{O}_6$, $\mathcal{O}_{10}$ are shown in Figure 5.3. As discussed above we assume an exposure to produce 200 neutrino events for each target. Each point in Figure 5.3

represents either the proton or neutron coupling as defined in Equation 5.2. In Figure 5.3 we have scaled the coupling by a factor $m_v = 246$ GeV, so that the resulting quantity $c_i m_v^2$ is dimensionless (the c_i's as defined in Ref. [121] have dimensions of inverse mass-squared). Also shown are the corresponding WIMP-nucleon cross sections calculated as $\sigma_i = \frac{c_i^2 \mu^2}{m_v^4}$. For Si, Ge, and Xe, the excess spin in the nucleus is carried by the neutron, so that for a fixed number of neutrino events the neutron coupling corresponds to a lower cross section. For flourine the excess spin is carried by the proton, so in this case for a fixed number of neutrino events the proton coupling corresponds to a lower cross section. Note here that the $\mathcal{O}_1$ operator corresponds to the standard SI interaction and is in agreement with previous studies [30, 137].

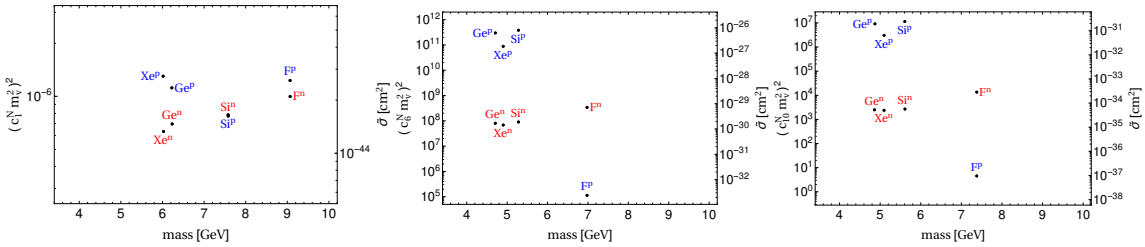

Figure 5.3: Best fit WIMP mass to the ^8B Solar neutrino induced nuclear recoil spectrum for Xe, Ge, Si, and F targets. For each target and each operator, we show the best fitting WIMP mass for neutron and proton couplings, defined as in Equation 5.2. The quantity on the vertical axis of the left-hand side in each figure is dimensionless, since the c_i's as defined in Ref. [121] have dimensions of inverse mass-squared. An exposure is assumed to produce 200 neutrino events for each target.

5.3.2 Grouping of Operators

Although we consider 15 operators, each of which coupling to protons and neutrons, the nuclear recoil energy spectra that is induced by many of these operators are similar. This is evident from their best fitting WIMP masses shown Figure 5.3 and in Figure D.1 in Appendix A, which shows the best fitting masses for the operators that are not shown in Figure 5.3. These figures motivate a grouping of operators based on their best fit WIMP mass, which are shown in Table 5.3. Operators $\mathcal{O}_{1,4,7,8}$,

$\mathcal{O}_{5,9,10,11,12,14}$ and $\mathcal{O}_{3,6,13,15}$ form group 1, 2 and 3 respectively (this is a similar grouping to that found in [133], although $\mathcal{O}_{13}$ is in our third group along with $\mathcal{O}_{15}$, rather than in a fourth). For the entries in this table we have assumed a Xe target, though we have checked that these results do not strongly depend on the nature of the target. We again emphasize that for many operators, the χ^2 is large when comparing the neutrino-induced spectra to the WIMP spectra, so that even these "worst case" scenarios should be easily distinguishable from the neutrino backgrounds, provided an experiment can obtain a robust measurement of the recoil energy spectrum.

Table 5.3: List of NR effective operators categorized by the best fit mass to ^{8}B Solar neutrinos in Xenon (the other targets follow suit). The third column gives the exposure to reach saturation due to the neutrino background, as defined in Section 5.4.

	Operator	Mass (GeV)	Exp. (t.y)
Group 1	$\mathcal{O}_1$	6	2.9
	$\mathcal{O}_4$	6	3.5
	$\mathcal{O}_7$	6.2	4.3
	$\mathcal{O}_8$	6.3	3.6
	q^2 and $q^2 v_T^2$		
Group 2	$\mathcal{O}_5$	4.8	0.43
	$\mathcal{O}_9$	4.6	0.34
	$\mathcal{O}_{10}$	4.6	0.36
	$\mathcal{O}_{11}$	4.6	0.40
	$\mathcal{O}_{12}$	4.6	0.44
	$\mathcal{O}_{14}$	4.8	0.43
	$q^2 v_T^2$, q^4 and $q^4 v_T^2$		
Group 3	$\mathcal{O}_3$	4.2	0.27
	$\mathcal{O}_6$	4.2	0.29
	$\mathcal{O}_{13}$	4.2	0.27
	$\mathcal{O}_{15}$	4.1	0.21

5.4 Discovery Bounds

With the nuclear recoil spectrum in non-relativistic EFT understood, we now move on to determine the bounds on the discovery of WIMPs in the presence of the neutrino background. We determine the exposure at which each operator is maximally affected by the neutrino background. As above we distinguish between those operators that are most and least affected by the neutrino background.

5.4.1 Formalism

The statistical formalism that we employ follows that of Ref. [30]. Here we review the relevant aspects for our analysis. The discovery potential of an experiment is defined as the smallest WIMP-nucleon cross section which produces a 3σ fluctuation above the background 90% of the time. To calculate this limit we use the following test statistic for the null hypothesis and try to reject it,

$$q_0 = \begin{cases} -2\log\frac{\mathcal{L}(\sigma=0,\hat{\theta})}{\mathcal{L}(\hat{\sigma},\hat{\hat{\theta}})} & \sigma \geq \hat{\sigma} \\ 0 & \sigma < \hat{\sigma} \end{cases} \tag{5.5}$$

where σ is the WIMP-nucleon cross section, θ represents the nuisance parameters (neutrino fluxes), and the hatted parameters are maximized. By Wilks' theorem, under background only experiments, q_0 is chi-square distributed and the equivalent gaussian significance is simply $\sqrt{q_0}$ [70]. To include the uncertainty of the neutrino flux normalization the likelihood function is modified to include a gaussian term [30]:

$$\mathcal{L} = \mathcal{L}_{Poisson} \prod_j e^{-\frac{1}{2}(1-N_j)^2\left(\frac{\phi_j}{\sigma_j}\right)^2} \tag{5.6}$$

where N_j is the flux normalization and ϕ_j and σ_j are the fluxes and their uncertainties given in Table 5.4. The Poisson likelihood $\mathcal{L}_{Poisson}$ is defined as in Equation 5.4.

We calculate the evolution of the discovery potential for all operators using a Xe based experiment, in the low and high recoil energy regions as defined above. The

Table 5.4: Neutrino flux components and their respective uncertainties in the flux normalizations. For the Solar components we utilize the high metallicity Solar model as outlined in Ref. [156].

component	ν flux ($\mathrm{cm}^{-2}\mathrm{s}^{-1}$)
PP	$5.98(1 \pm 0.006) \times 10^{10}$
^{7}Be	$5.00(1 \pm 0.07) \times 10^{9}$
^{8}B	$5.58(1 \pm 0.14) \times 10^{6}$
pep	$1.44(1 \pm 0.012) \times 10^{8}$
DSNB	85.5 ± 42.7
Atmospheric	10.5 ± 2.1

WIMP mass considered for each operator was taken from Table 5.1 as this is the worst case scenario where the WIMP spectrum most closely resembles the neutrino background. Note that while in the low region the best fit WIMP mass is very similar for the neutron and proton scattering rates, this is not the case in the high region. Thus in the low region the discovery potential curves remain parallel, but this is not necessarily the case for the high region. The discovery evolution for three of the operators from three groups is shown in Figure 5.4 and the remaining operators can be found in the Appendix. For operators which are sufficiently neutrino like (group 1), the evolution exhibits saturation when the systematic uncertainty in the neutrino flux becomes relevant. Note that this saturation is achieved at a smaller cross section than in previous studies [137], because the analysis in this paper separates proton and neutron couplings, thereby reducing the coherence factor and providing a less stringent limit. This saturation is then broken when the exposure becomes large enough that small differences in the WIMP and neutrino-induced recoil spectra become distinguishable [137].

For the other operators with recoil spectra that are sufficiently different than the neutrino-induced recoil spectra (group 2 and 3), no significant saturation is observed. For these cases a weak inflection point defines the exposure at which the saturation is a maximum. The corresponding saturations are listed for each operator in Table 5.3. From this table we see that operators in the same category reach the inflection point at very similar exposures. The operators that reach the inflection point at the lowest exposures are those that are most easily distinguishable from the neutrino backgrounds. These operators then return quickly to a $1/\sqrt{MT}$ evolution as the exposure is increased.

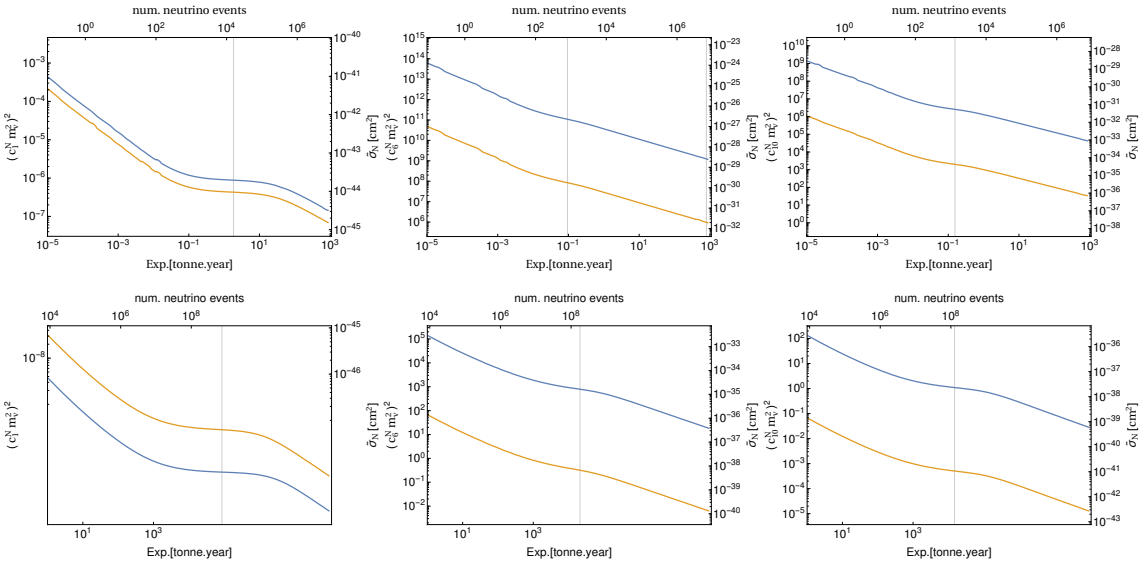

Figure 5.4: Discovery evolution of $\mathcal{O}_1$ (left), $\mathcal{O}_6$ (middle), $\mathcal{O}_{10}$ (right) operators, for the low region (top) and high region (bottom). The blue and yellow curves show the limits for proton and neutron scattering respectively

5.4.2 Discovery Limits and Exclusion Regions

We now move on to find the 3σ discovery limit across the entire WIMP mass range. We calculate the discovery limits for all operators using a single exposure which saturates $\mathcal{O}_1 \sim 10^4 (\sim 10^3)$ neutrino events in the low (high) region. The motivation for this choice is primarily a simplification of the analysis, noting that the discovery evolution of group 2 and 3 operators do not experience saturation as strongly as group 1 operators. The exposures for the different targets are given in Table 5.5.

Table 5.5: List of exposures used to calculate the neutrino floor

Target	exposure^{low} (t.y)	exposure^{high} (kt.y)
xenon	1.76	58
germanium	3.26	87
silicon	10.4	206
flourine	16.3	278

In addition to the discovery limits we also determine the 90% exclusion regions from the most recent LUX results [13]. To calculate exclusion limits we use the profile likelihood method with test statistic,

$$q_\sigma = \begin{cases} -2\log\frac{\mathcal{L}(\sigma,\hat{\theta})}{\mathcal{L}(\hat{\sigma},\hat{\hat{\theta}})} & \sigma \geq \hat{\sigma} \\ 0 & \sigma < \hat{\sigma} \end{cases}$$

where we now use a likelihood which includes gaussian terms for the astrophysical errors: $\rho_\chi = 0.3 \pm 0.1\text{GeV/cm}^3$, $v_0 = 220 \pm 20\text{km/s}$ and $v_{esc} = 544 \pm 40\text{km/s}$. Under repeated background-only experiments q_σ is half-chi-square distributed and the significance is $\sqrt{q_\sigma}$.

For each of the operators, we calculate 90% confidence limits for the inner 18cm fiducial volume (117kg) over the 95 day LUX run, which resulted in a 30.5 kg day

exposure. For simplicity we will assume that the background prediction is uniform throughout the fiducial volume. While this is actually likely not the case, it is a conservative estimate given the background is lower within the inner fiducial volume. After the 99.6% electronic recoil discrimination efficiency, 1.9 events were expected in the nuclear recoil region, and 2 were actually observed. The energy dependent detector efficiency was taken from LUXcalc [157], which takes into account detector resolution and threshold effects. While this efficiency curve is based on the 2013 LUX analysis, we have reduced the threshold to 1.1keV in line with the more recent analysis. The results we obtained are in good agreement with the official exclusion curves, as illustrated in Fig. 5.5. A summary of the experimental specifications are given in Table 5.6.

Table 5.6: Experimental specifications used to generate exclusion curves

Name	Target	Exp. (kg.y)	ROI	efficiency	background	observed
LUX	Xe	30.5	1.1-41 keV	0.5	1.9	2

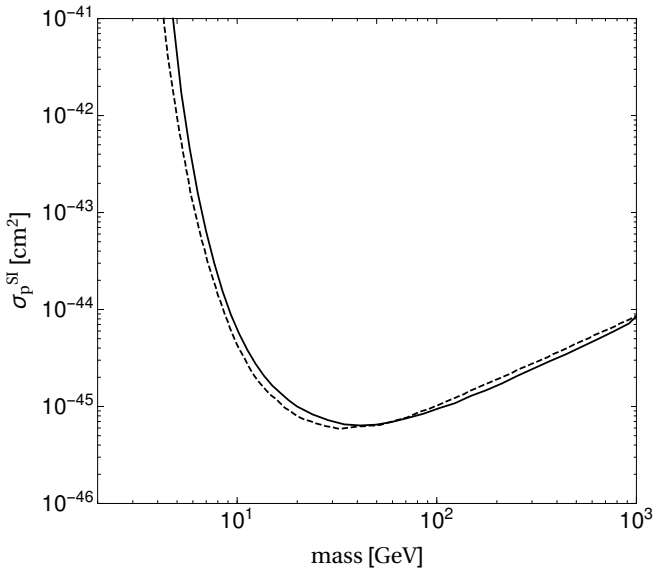

Figure 5.5: Comparison of our exclusion limits (solid) with the official LUX result (dashed)

Figure 5.6 shows the discovery limits and exclusion curves for $\mathcal{O}_1$ (top), $\mathcal{O}_6$ (middle), $\mathcal{O}_{10}$. The corresponding discovery limits and exclusion curves for the remaining operators are shown in the Appendix. For several operators, for example $\mathcal{O}_6$ coupling to neutrons, we find that the calculated limits (grey shaded regions) are overlapping with the discovery limits curves for low mass where the discovery limit is dominated by Solar neutrinos. This does not imply a contradiction, as the exclusion curves, which only apply to xenon targets, do not overlap the xenon discovery limits. The proximity of the exclusion curves to the discovery limits (which have vastly larger exposures) is a reflection of the different statistical procedures used to generate the two sets of curves. In particular, the calculated discovery limits are a more statistically demanding criteria than an exclusion limit at 90% confidence, so for a given WIMP mass and cross section a larger exposure would be required to claim a 3σ fluctuation. In future larger scale detectors for which the neutrino signal will be non-negligible, it will be necessary to include neutrinos into the statistical model that determines exclusion regions.

5.5 Discussion and Conclusion

In order to continue to improve bounds on the WIMP-nucleon cross section, future larger scale detectors must become effective at distinguishing a WIMP interaction from a neutrino interaction. In this paper we considered this issue within the well-motivated EFT framework. Within this framework, the standard SI and SD interactions represent only a portion of a larger set of nuclear responses which must be considered in direct dark matter detection. We specifically focus on the set of EFT operators that respect Galilean invariance, time-reversal symmetry, and Hermiticity.

We have shown that for 10 of the 14 operators, the energy spectrum induced by WIMPs is distinct from that induced by neutrinos. For these operators, we show that

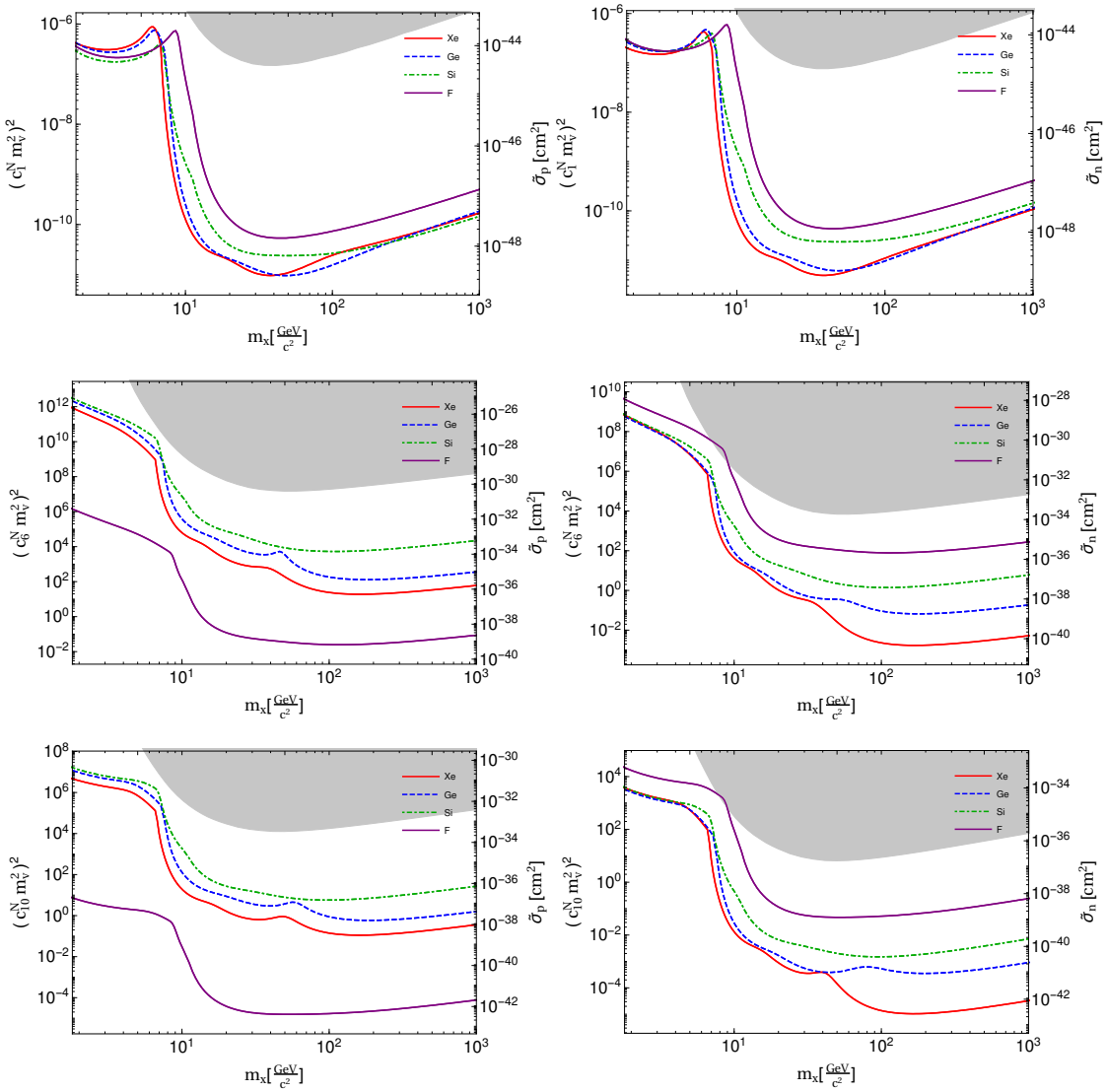

Figure 5.6: Discovery limits for $\mathcal{O}_1$ (top), $\mathcal{O}_6$ (middle), $\mathcal{O}_{10}$ (bottom), for protons (left) and neutrons (right). The shaded region shows the 90% confidence limits for a 30.5 kg day exposure at LUX.

a clean statistical separation between WIMPs and neutrinos will be possible. For only 4 of the 14 WIMP-nucleon operators that we consider do we find that the WIMP and neutrino spectrum can be highly degenerate. For these 4 operators (which belong to group 1) we specifically calculate the "worst-case scenario" WIMP mass which most closely matches the neutrino spectra. Our results show that an experiment with good spectral energy resolution and exposure near the ton scale should have little trouble

distinguishing certain WIMP interactions from neutrino-induced nuclear recoil events. The group 2 and 3 operators would require an exposure of about 0.5 tonne years to be distinguished from the neutrino background for a low mass WIMP (as can be surmised from the linear region of Figure 5.4 beyond the saturation region/inflection point). The group 1 operators can be distinguished from the neutrino backgrounds for a sufficiently large exposure, $\sim 10^3$ tonne years.

Relative to previous results that considered energy deposition, our theoretical framework is more complete and encompasses a wider range of possible nuclear responses. In its most general form, the WIMP nucleon cross section is a superposition of all of the operators that we have discussed, with the observable being a superposition of the corresponding nuclear recoil spectrum for each operator. The limiting case that we have studied here in which a single operator dominates the cross section will provide guidance and intuition for future more detailed studies that consider more complicated superpositions of operators. In order to extract information about the particle properties of dark matter from a detection of events, the challenge that future detectors will face not only lies in reducing the neutrino backgrounds, but also in understanding the degeneracies that are incurred when attempting to map the detected energy spectrum onto a particular superposition of operators [127].

Chapter 6

CONCLUSION

It has been four decades since dark matter halos were discovered, three decades since direct detection was proposed and two decades since the first experiment was demonstrated. Now, with the maturation of detector technology, recent years have seen renewed interest in the phenomenology of direct detection experiments. Studies have found that long held assumptions greatly affect the interpretation of the data. This dissertation has evaluated key assumptions that must not be taken for granted if one is to obtain a robust interpretation of putative signals. In particular, the dark matter halo parameters, inelastic scattering and isospin violation, each affect the ability to correctly estimate WIMP parameters. Additionally, the underlying assumption of SI/SD scattering rather than non-standard operator scattering can lead to a radical misinterpretation of results. Thus additional operators that cannot be ruled out by other means must be considered. With a much larger parameter space than originally assumed, parameter estimation becomes more difficult. It has been demonstrated that the best method for improving parameter estimation in this case is making use of detector complementarity. Thus it is important that future detectors are made from a variety of target materials. Fortunately, Xenon1t (xenon), SuperCDMS (germanium and silicon) and DarkSide (argon) are all poised to operate large scale detectors in the coming years.

In chapter 4 it was demonstrated that at least 2000 (background free) events are required to distinguish between operators. Dark matter has yet to be discovered and the neutrino floor lies around three orders of magnitude below current experimental sensitivity. Thus it is unlikely that 2000 WIMP events can be observed without back-

ground neutrino events. This will be problematic if dark matter does not interact through one of the operators which can be distinguished clearly from coherent scattering.

To be able to confidently discriminate models based on direct detection data, further work needs to be carried out. To fully address the question of discernability, one needs to start from a UV model of dark matter, integrate out the mediator and run the resulting theory down to the electroweak breaking scale. From there, one can match Wilson coefficients with the Standard Model and run the coefficients down to the nuclear scale. The running of coefficients down from the UV scale may induce operator mixing, a very important effect to include when it comes to discerning the UV physics. Given that the relative strength of operators differs by many orders of magnitude, it is possible that some of the more unique operators could be completely washed out by even a small mixing with spin independent operators. This would introduce huge degeneracies and spell disaster for the goals of trying to discern UV physics with direct detection experiments. Thus it is vital to the interpretation of direct detection data to understand and apply these effects, and only then can WIMP models be evaluated correctly.

REFERENCES

[1] Lawrence M. Krauss and Michael S. Turner. The Cosmological constant is back. *Gen. Rel. Grav.*, 27:1137–1144, 1995.

[2] A. G. Riess, A. V. Filippenko, P. Challis, A. Clocchiatti, A. Diercks, P. M. Garnavich, R. L. Gilliland, C. J. Hogan, S. Jha, R. P. Kirshner, B. Leibundgut, M. M. Phillips, D. Reiss, B. P. Schmidt, R. A. Schommer, R. C. Smith, J. Spyromilio, C. Stubbs, N. B. Suntzeff, and J. Tonry. Observational Evidence from Supernovae for an Accelerating Universe and a Cosmological Constant. *The Astrophysical Journal*, 116:1009–1038, September 1998.

[3] S. Perlmutter et al. Measurements of Omega and Lambda from 42 high redshift supernovae. *Astrophys. J.*, 517:565–586, 1999.

[4] P. A. R. Ade et al. Planck 2015 results. XIII. Cosmological parameters. 2015.

[5] F. Zwicky. On the masses of nebulae and of clusters of nebulae. *Astrophys. J.*, 86:217, 1937.

[6] K. C. Freeman. On the Disks of Spiral and so Galaxies. *ApJ*, 160:811, June 1970.

[7] V. C. Rubin and W. K. Ford, Jr. Rotation of the Andromeda Nebula from a Spectroscopic Survey of Emission Regions. *ApJ*, 159:379, February 1970.

[8] Douglas Clowe, Marusa Bradac, Anthony H. Gonzalez, Maxim Markevitch, Scott W. Randall, Christine Jones, and Dennis Zaritsky. A direct empirical proof of the existence of dark matter. *Astrophys. J.*, 648:L109–L113, 2006.

[9] *see http://www.mergingclustercollaboration.org/merging-clusters.html.*

[10] Signe Riemer-Sorensen, David Parkinson, and Tamara M. Davis. Combining Planck data with large scale structure information gives a strong neutrino mass constraint. *Phys. Rev.*, D89:103505, 2014.

[11] Blas Cabrera, Lawrence M. Krauss, and Frank Wilczek. Bolometric Detection of Neutrinos. *Phys. Rev. Lett.*, 55:25, 1985.

[12] Mark W. Goodman and Edward Witten. Detectability of Certain Dark Matter Candidates. *Phys. Rev.*, D31:3059, 1985.

[13] D. S. Akerib et al. Improved WIMP scattering limits from the LUX experiment. 2015.

[14] R. Agnese et al. Search for Low-Mass Weakly Interacting Massive Particles with SuperCDMS. *Phys. Rev. Lett.*, 112(24):241302, 2014.

[15] E. Aprile et al. Lowering the radioactivity of the photomultiplier tubes for the XENON1T dark matter experiment. *Eur. Phys. J.*, C75(11):546, 2015.

[16] J. B. R. Battat et al. First background-free limit from a directional dark matter experiment: results from a fully fiducialised DRIFT detector. *Phys. Dark Univ.*, 9-10:1–7, 2014.

[17] Jayden L. Newstead, Thomas D. Jacques, Lawrence M. Krauss, James B. Dent, and Francesc Ferrer. Scientific reach of multiton-scale dark matter direct detection experiments. *Phys. Rev.*, D88(7):076011, 2013.

[18] A. Liam Fitzpatrick, Wick Haxton, Emanuel Katz, Nicholas Lubbers, and Yiming Xu. The Effective Field Theory of Dark Matter Direct Detection. *JCAP*, 1302:004, 2013.

[19] James B. Dent, Lawrence M. Krauss, Jayden L. Newstead, and Subir Sabharwal. General analysis of direct dark matter detection: From microphysics to observational signatures. *Phys. Rev.*, D92(6):063515, 2015.

[20] James B. Dent, Bhaskar Dutta, Jayden L. Newstead, and Louis E. Strigari. No ν floors: Effective field theory treatment of the neutrino background in direct dark matter detection experiments. *Phys. Rev. (accepted)*, 2016.

[21] Yashar Akrami, Christopher Savage, Pat Scott, Jan Conrad, and Joakim Edsjo. How well will ton-scale dark matter direct detection experiments constrain minimal supersymmetry? *JCAP*, 1104:012, 2011.

[22] Miguel Pato, Laura Baudis, Gianfranco Bertone, Roberto Ruiz de Austri, Louis E. Strigari, et al. Complementarity of Dark Matter Direct Detection Targets. *Phys.Rev.*, D83:083505, 2011.

[23] Chung-Lin Shan. Estimating the Spin-Independent WIMP-Nucleon Coupling from Direct Dark Matter Detection Data. 2011.

[24] Chung-Lin Shan. Determining Ratios of WIMP-Nucleon Cross Sections from Direct Dark Matter Detection Data. *JCAP*, 1107:005, 2011.

[25] Miguel Pato. What can(not) be measured with ton-scale dark matter direct detection experiments. *JCAP*, 1110:035, 2011.

[26] Charlotte Strege, Roberto Trotta, Gianfranco Bertone, Annika H.G. Peter, and Pat Scott. Fundamental statistical limitations of future dark matter direct detection experiments. *Phys.Rev.*, D86:023507, 2012.

[27] Laura Baudis. Direct dark matter detection: the next decade. *Phys.Dark Univ.*, 1:94–108, 2012.

[28] D.G. Cerdeño, C. Cuesta, M. Fornasa, E. García, C. Ginestra, et al. Complementarity of dark matter direct detection: the role of bolometric targets. *JCAP*, 1307:028, 2013.

[29] Chiara Arina, Gianfranco Bertone, and Hamish Silverwood. Complementarity of direct and indirect Dark Matter detection experiments. *Phys.Rev.*, D88:013002, 2013.

[30] J. Billard, L. Strigari, and E. Figueroa-Feliciano. Implication of neutrino backgrounds on the reach of next generation dark matter direct detection experiments. *Phys. Rev.*, D89(2):023524, 2014.

[31] E. Aprile et al. Dark Matter Results from 225 Live Days of XENON100 Data. *Phys.Rev.Lett.*, 109:181301, 2012.

[32] P. Benetti, R. Acciarri, F. Adamo, B. Baibussinov, M. Baldo-Ceolin, et al. First results from a Dark Matter search with liquid Argon at 87 K in the Gran Sasso Underground Laboratory. *Astropart.Phys.*, 28:495–507, 2008.

[33] Laura Baudis. DARWIN: dark matter WIMP search with noble liquids. *PoS*, IDM2010:122, 2011.

[34] Marc Schumann. DARWIN. In *Proceedings, 7th Patras Workshop on Axions, WIMPs and WISPs (AXION-WIMP 2011)*, pages 23–26, 2011.

[35] Laura Baudis. DARWIN: dark matter WIMP search with noble liquids. *J.Phys.Conf.Ser.*, 375:012028, 2012.

[36] J. Engel and P. Vogel. Spin dependent cross-sections of weakly interacting massive particles on nuclei. *Phys.Rev.*, D40:3132–3135, 1989.

[37] Francesco Iachello, Lawrence M. Krauss, and Giuseppe Maino. SPIN DEPENDENT SCATTERING OF WEAKLY INTERACTING MASSIVE PARTICLES IN HEAVY NUCLEI. *Phys.Lett.*, B254:220–224, 1991.

[38] J. Engel. Nuclear form-factors for the scattering of weakly interacting massive particles. *Phys.Lett.*, B264:114–119, 1991.

[39] Marc Kamionkowski, Lawrence M. Krauss, and M. Ted Ressell. Implications of recent nucleon spin structure measurements for neutralino dark matter detection. 1994.

[40] Gerard Jungman, Marc Kamionkowski, and Kim Griest. Supersymmetric dark matter. *Phys. Rep.*, 267(5-6):195 – 373, 1996.

[41] David Tucker-Smith and Neal Weiner. Inelastic dark matter. *Phys.Rev.*, D64:043502, 2001.

[42] Jonathan Engel. Nuclear form factors for the scattering of neutralinos. *Nuclear Physics B - Proceedings Supplements*, 28(1):310 – 313, 1992.

[43] J.D. Lewin and P.F. Smith. Review of mathematics, numerical factors, and corrections for dark matter experiments based on elastic nuclear recoil. *Astroparticle Physics*, 6(1):87 – 112, 1996.

[44] Ya-Zheng Chen, Jun-Mou Chen, Yan-An Luo, Hong Shen, and Xue-Qian Li. Effects of nuclear deformation on the form factor for direct dark matter detection. *Chin.Phys.*, C36:505–512, 2012.

[45] D.G. Cerdeno, M. Fornasa, J.H. Huh, and M. Peiro. Nuclear uncertainties in the spin-dependent structure functions for direct dark matter detection. *Phys.Rev.*, D87:023512, 2013.

[46] G. Fricke, C. Bernhardt, K. Heilig, L.A. Schaller, L. Schellenberg, E.B. Shera, and C.W. Dejager. Nuclear ground state charge radii from electromagnetic interactions. *Atomic Data and Nuclear Data Tables*, 60(2):177 – 285, 1995.

[47] Gintaras Duda, Ann Kemper, and Paolo Gondolo. Model Independent Form Factors for Spin Independent Neutralino-Nucleon Scattering from Elastic Electron Scattering Data. *JCAP*, 0704:012, 2007.

[48] L. Lapikás. Xenon charge distribution. *HERMES Internal Report*, pages 04–041, 2004.

[49] Michael Kuhlen, Neal Weiner, Jurg Diemand, Piero Madau, Ben Moore, et al. Dark Matter Direct Detection with Non-Maxwellian Velocity Structure. *JCAP*, 1002:030, 2010.

[50] Louis E. Strigari and Roberto Trotta. Reconstructing WIMP Properties in Direct Detection Experiments Including Galactic Dark Matter Distribution Uncertainties. *JCAP*, 0911:019, 2009.

[51] Riccardo Catena and Piero Ullio. The local dark matter phase-space density and impact on WIMP direct detection. *JCAP*, 1205:005, 2012.

[52] Malcolm Fairbairn, Tom Douce, and Jace Swift. Quantifying Astrophysical Uncertainties on Dark Matter Direct Detection Results. *Astropart. Phys.*, 47:45–53, 2013.

[53] Miguel Pato, Louis E. Strigari, Roberto Trotta, and Gianfranco Bertone. Taming astrophysical bias in direct dark matter searches. *JCAP*, 1302:041, 2013.

[54] Walter Dehnen and James Binney. Local stellar kinematics from hipparcos data. *Mon.Not.Roy.Astron.Soc.*, 298:387–394, 1998.

[55] Christopher McCabe. The Astrophysical Uncertainties Of Dark Matter Direct Detection Experiments. *Phys.Rev.*, D82:023530, 2010.

[56] Lars Hernquist. AN ANALYTICAL MODEL FOR SPHERICAL GALAXIES AND BULGES. *Astrophys.J.*, 356:359, 1990.

[57] Julio F. Navarro, Carlos S. Frenk, and Simon D. M. White. The Structure of Cold Dark Matter Halos. *Astrophys. J.*, 462:563–575, 1996.

[58] A. Burkert. The Structure of dark matter halos in dwarf galaxies. *IAU Symp.*, 171:175, 1996.

[59] Jaan Einasto. Dark Matter. In *Astronomy and Astrophysics 2010, [Eds. Oddbjorn Engvold, Rolf Stabell, Bozena Czerny, John Lattanzio], in Encyclopedia of Life Support Systems (EOLSS), Developed under the Auspices of the UNESCO, Eolss Publishers, Oxford ,UK*, 2009.

[60] Alister W. Graham, David Merritt, Ben Moore, Juerg Diemand, and Balsa Terzic. Empirical models for Dark Matter Halos. I. Nonparametric Construction of Density Profiles and Comparison with Parametric Models. *Astron. J.*, 132:2685–2700, 2006.

[61] J. Binney and S. Tremaine. *Galactic Dynamics*. Princeton Series in Astrophysics. Princeton University Press, second edition, 2008.

[62] Michael Kuhlen, Annalisa Pillepich, Javiera Guedes, and Piero Madau. The Distribution of Dark Matter in the Milky Way's Disk. *Astrophys. J.*, 784:161, 2014.

[63] Mark J. Reid and A. Brunthaler. The Proper motion of Sgr A*. 2. The Mass of Sgr A*. *Astrophys.J.*, 616:872–884, 2004.

[64] Aurel Schneider, Lawrence Krauss, and Ben Moore. Impact of Dark Matter Microhalos on Signatures for Direct and Indirect Detection. *Phys.Rev.*, D82:063525, 2010.

[65] Anne M. Green. Astrophysical uncertainties on direct detection experiments. *Mod. Phys. Lett.*, A27:1230004, 2012.

[66] Paul J. McMillan and James J. Binney. The uncertainty in Galactic parameters. *Mon. Not. Roy. Astron. Soc.*, 402:934, 2010.

[67] P. Salucci, F. Nesti, G. Gentile, and C.F. Martins. The dark matter density at the Sun's location. *Astron.Astrophys.*, 523:A83, 2010.

[68] Henning O. Back, Frank Calaprice, Christopher Condon, Ernst de Haas, Richard Ford, et al. First Large Scale Production of Low Radioactivity Argon From Underground Sources. 2012.

[69] E. Aprile et al. Likelihood Approach to the First Dark Matter Results from XENON100. *Phys.Rev.*, D84:052003, 2011.

[70] Glen Cowan, Kyle Cranmer, Eilam Gross, and Ofer Vitells. Asymptotic formulae for likelihood-based tests of new physics. *Eur. Phys. J.*, C71:1554, 2011. [Erratum: Eur. Phys. J.C73,2501(2013)].

[71] DarkSide Collaboration. *Snowmass 2013, Darkside Whitepaper*, 2013.

[72] Elena Aprile. The XENON1T Dark Matter Search Experiment. *Springer Proc. Phys.*, 148:93–96, 2013.

[73] Craig J. Copi and Lawrence M. Krauss. Comparing WIMP interaction rate detectors with annual modulation detectors. *Phys.Rev.*, D67:103507, 2003.

[74] F. Feroz, M. P. Hobson, and M. Bridges. MultiNest: an efficient and robust Bayesian inference tool for cosmology and particle physics. 2008. arXiv:astro-ph/0809.3437.

[75] Sergey E. Koposov, Walter Rix, and David W. Hogg. Constraining the milky way potential with a six-dimensional phase-space map of the gd-1 stellar stream. *The Astrophysical Journal*, 712:260, 2010.

[76] A. Siebert. Status and results from the RAVE survey. 2012.

[77] Markus Weber and Wim de Boer. Determination of the Local Dark Matter Density in our Galaxy. *Astron.Astrophys.*, 509:A25, 2010.

[78] Yoshiaki Sofue and Vera Rubin. Rotation curves of spiral galaxies. *Ann. Rev. Astron. Astrophys.*, 39:137–174, 2001.

[79] Shaun Cole et al. The 2dF Galaxy Redshift Survey: Power-spectrum analysis of the final dataset and cosmological implications. *Mon. Not. Roy. Astron. Soc.*, 362:505–534, 2005.

[80] Florian Beutler, Chris Blake, Matthew Colless, D. Heath Jones, Lister Staveley-Smith, Lachlan Campbell, Quentin Parker, Will Saunders, and Fred Watson. The 6dF Galaxy Survey: Baryon Acoustic Oscillations and the Local Hubble Constant. *Mon. Not. Roy. Astron. Soc.*, 416:3017–3032, 2011.

[81] Lauren Anderson et al. The clustering of galaxies in the SDSS-III Baryon Oscillation Spectroscopic Survey: Baryon Acoustic Oscillations in the Data Release 9 Spectroscopic Galaxy Sample. *Mon. Not. Roy. Astron. Soc.*, 427(4):3435–3467, 2013.

[82] A. Vikhlinin et al. Chandra Cluster Cosmology Project III: Cosmological Parameter Constraints. *Astrophys. J.*, 692:1060–1074, 2009.

[83] L. Fu et al. Very weak lensing in the CFHTLS Wide: Cosmology from cosmic shear in the linear regime. *Astron. Astrophys.*, 479:9–25, 2008.

[84] Richard Massey et al. COSMOS: 3D weak lensing and the growth of structure. *Astrophys. J. Suppl.*, 172:239–253, 2007.

[85] P. A. R. Ade et al. Planck 2013 results. XVI. Cosmological parameters. *Astron. Astrophys.*, 571:A16, 2014.

[86] Oscar Adriani et al. An anomalous positron abundance in cosmic rays with energies 1.5-100 GeV. *Nature*, 458:607–609, 2009.

[87] Meng Su, Tracy R. Slatyer, and Douglas P. Finkbeiner. Giant Gamma-ray Bubbles from Fermi-LAT: AGN Activity or Bipolar Galactic Wind? *Astrophys. J.*, 724:1044–1082, 2010.

[88] Dan Hooper and Lisa Goodenough. Dark Matter Annihilation in The Galactic Center As Seen by the Fermi Gamma Ray Space Telescope. *Phys. Lett.*, B697:412–428, 2011.

[89] Christoph Weniger. A Tentative Gamma-Ray Line from Dark Matter Annihilation at the Fermi Large Area Telescope. *JCAP*, 1208:007, 2012.

[90] Esra Bulbul, Maxim Markevitch, Adam Foster, Randall K. Smith, Michael Loewenstein, and Scott W. Randall. Detection of An Unidentified Emission Line in the Stacked X-ray spectrum of Galaxy Clusters. *Astrophys. J.*, 789:13, 2014.

[91] Georges Aad et al. Search for dark matter in events with a Z boson and missing transverse momentum in pp collisions at $\sqrt{s}$=8 TeV with the ATLAS detector. *Phys. Rev.*, D90(1):012004, 2014.

[92] Georges Aad et al. Search for dark matter in events with heavy quarks and missing transverse momentum in *pp* collisions with the ATLAS detector. *Eur. Phys. J.*, C75(2):92, 2015.

[93] Georges Aad et al. Search for new phenomena in final states with an energetic jet and large missing transverse momentum in pp collisions at $\sqrt{s}$ =8 TeV with the ATLAS detector. *Eur. Phys. J.*, C75(7):299, 2015. [Erratum: Eur. Phys. J.C75,no.9,408(2015)].

[94] Georges Aad et al. Search for dark matter in events with a hadronically decaying W or Z boson and missing transverse momentum in *pp* collisions at $\sqrt{s} = 8$ TeV with the ATLAS detector. *Phys. Rev. Lett.*, 112(4):041802, 2014.

[95] Steven Lowette. Search for Dark Matter at CMS. 2014.

[96] D. S. Akerib et al. First results from the LUX dark matter experiment at the Sanford Underground Research Facility. *Phys. Rev. Lett.*, 112:091303, 2014.

[97] Z. Ahmed et al. Results from a Low-Energy Analysis of the CDMS II Germanium Data. *Phys. Rev. Lett.*, 106:131302, 2011.

[98] R. Agnese et al. Silicon Detector Dark Matter Results from the Final Exposure of CDMS II. *Phys. Rev. Lett.*, 111(25):251301, 2013.

[99] R. Bernabei et al. First results from DAMA/LIBRA and the combined results with DAMA/NaI. *Eur. Phys. J.*, C56:333–355, 2008.

[100] C. E. Aalseth et al. CoGeNT: A Search for Low-Mass Dark Matter using p-type Point Contact Germanium Detectors. *Phys. Rev.*, D88:012002, 2013.

[101] G. Angloher et al. Results from 730 kg days of the CRESST-II Dark Matter Search. *Eur. Phys. J.*, C72:1971, 2012.

[102] J. Sander et al. SuperCDMS status from Soudan and plans for SNOLab. *AIP Conf. Proc.*, 1534:129–135, 2012.

[103] R. Agnese et al. Search for Low-Mass Weakly Interacting Massive Particles Using Voltage-Assisted Calorimetric Ionization Detection in the SuperCDMS Experiment. *Phys. Rev. Lett.*, 112(4):041302, 2014.

[104] Spencer Chang, Graham D. Kribs, David Tucker-Smith, and Neal Weiner. Inelastic Dark Matter in Light of DAMA/LIBRA. *Phys. Rev.*, D79:043513, 2009.

[105] Brian Feldstein, A. Liam Fitzpatrick, and Emanuel Katz. Form Factor Dark Matter. *JCAP*, 1001:020, 2010.

[106] Spencer Chang, Aaron Pierce, and Neal Weiner. Momentum Dependent Dark Matter Scattering. *JCAP*, 1001:006, 2010.

[107] Vernon Barger, Wai-Yee Keung, and Danny Marfatia. Electromagnetic properties of dark matter: Dipole moments and charge form factor. *Phys. Lett.*, B696:74–78, 2011.

[108] Tom Banks, Jean-Francois Fortin, and Scott Thomas. Direct Detection of Dark Matter Electromagnetic Dipole Moments. 2010.

[109] R. Foot. A comprehensive analysis of the dark matter direct detection experiments in the mirror dark matter framework. *Phys. Rev.*, D82:095001, 2010.

[110] Chiu Man Ho and Robert J. Scherrer. Anapole Dark Matter. *Phys. Lett.*, B722:341–346, 2013.

[111] Jessica Goodman, Masahiro Ibe, Arvind Rajaraman, William Shepherd, Tim M. P. Tait, and Hai-Bo Yu. Constraints on Dark Matter from Colliders. *Phys. Rev.*, D82:116010, 2010.

[112] Yang Bai, Patrick J. Fox, and Roni Harnik. The Tevatron at the Frontier of Dark Matter Direct Detection. *JHEP*, 12:048, 2010.

[113] Csaba Balázs, Tong Li, and Jayden L. Newstead. Thermal dark matter implies new physics not far above the weak scale. *JHEP*, 08:061, 2014.

[114] Giorgio Busoni, Andrea De Simone, Enrico Morgante, and Antonio Riotto. On the Validity of the Effective Field Theory for Dark Matter Searches at the LHC. *Phys. Lett.*, B728:412–421, 2014.

[115] Daniele Alves. Simplified Models for LHC New Physics Searches. *J. Phys.*, G39:105005, 2012.

[116] Arvind Rajaraman, William Shepherd, Tim M. P. Tait, and Alexander M. Wijangco. LHC Bounds on Interactions of Dark Matter. *Phys. Rev.*, D84:095013, 2011.

[117] O. Buchmueller, Matthew J. Dolan, and Christopher McCabe. Beyond Effective Field Theory for Dark Matter Searches at the LHC. *JHEP*, 01:025, 2014.

[118] Asher Berlin, Dan Hooper, and Samuel D. McDermott. Simplified Dark Matter Models for the Galactic Center Gamma-Ray Excess. *Phys. Rev.*, D89(11):115022, 2014.

[119] Csaba Balázs and Tong Li. Simplified Dark Matter Models Confront the Gamma Ray Excess. *Phys. Rev.*, D90(5):055026, 2014.

[120] JiJi Fan, Matthew Reece, and Lian-Tao Wang. Non-relativistic effective theory of dark matter direct detection. *JCAP*, 1011:042, 2010.

[121] Nikhil Anand, A. Liam Fitzpatrick, and W. C. Haxton. Weakly interacting massive particle-nucleus elastic scattering response. *Phys. Rev.*, C89(6):065501, 2014.

[122] Nikhil Anand, A. Liam Fitzpatrick, and W. C. Haxton. Model-independent Analyses of Dark-Matter Particle Interactions. *Phys. Procedia*, 61:97–106, 2015.

[123] Moira I. Gresham and Kathryn M. Zurek. Effect of nuclear response functions in dark matter direct detection. *Phys. Rev.*, D89(12):123521, 2014.

[124] Junji Hisano, Koji Ishiwata, Natsumi Nagata, and Masato Yamanaka. Direct Detection of Vector Dark Matter. *Prog. Theor. Phys.*, 126:435–456, 2011.

[125] Jonathan L. Feng and Jason Kumar. The WIMPless Miracle: Dark-Matter Particles without Weak-Scale Masses or Weak Interactions. *Phys. Rev. Lett.*, 101:231301, 2008.

[126] Riccardo Catena and Paolo Gondolo. Global fits of the dark matter-nucleon effective interactions. *JCAP*, 1409(09):045, 2014.

[127] Vera Gluscevic, Moira I. Gresham, Samuel D. McDermott, Annika H. G. Peter, and Kathryn M. Zurek. Identifying the Theory of Dark Matter with Direct Detection. *JCAP*, 1512(12):057, 2015.

[128] H. Jeffreys. *Theory of Probability*. Oxford University Press, 1939.

[129] C. Amole et al. Dark Matter Search Results from the PICO-2L C_3F_8 Bubble Chamber. *Phys. Rev. Lett.*, 114(23):231302, 2015.

[130] E. Aprile et al. Physics reach of the XENON1T dark matter experiment. *Submitted to: JCAP*, 2015.

[131] D. S. Akerib et al. LUX-ZEPLIN (LZ) Conceptual Design Report. 2015.

[132] J. D. Lewin and P. F. Smith. Review of mathematics, numerical factors, and corrections for dark matter experiments based on elastic nuclear recoil. *Astropart. Phys.*, 6:87–112, 1996.

[133] Riccardo Catena. Dark matter directional detection in non-relativistic effective theories. *JCAP*, 1507(07):026, 2015.

[134] Bradley J. Kavanagh. New directional signatures from the nonrelativistic effective field theory of dark matter. *Phys. Rev.*, D92(2):023513, 2015.

[135] Jocelyn Monroe and Peter Fisher. Neutrino Backgrounds to Dark Matter Searches. *Phys. Rev.*, D76:033007, 2007.

[136] Louis E. Strigari. Neutrino Coherent Scattering Rates at Direct Dark Matter Detectors. *New J. Phys.*, 11:105011, 2009.

[137] F. Ruppin, J. Billard, E. Figueroa-Feliciano, and L. Strigari. Complementarity of dark matter detectors in light of the neutrino background. *Phys. Rev.*, D90(8):083510, 2014.

[138] Jonathan H. Davis. Dark Matter vs. Neutrinos: The effect of astrophysical uncertainties and timing information on the neutrino floor. *JCAP*, 1503:012, 2015.

[139] Katherine Freese, Mariangela Lisanti, and Christopher Savage. Colloquium: Annual modulation of dark matter. *Rev. Mod. Phys.*, 85:1561–1581, 2013.

[140] Philipp Grothaus, Malcolm Fairbairn, and Jocelyn Monroe. Directional Dark Matter Detection Beyond the Neutrino Bound. *Phys. Rev.*, D90(5):055018, 2014.

[141] Ciaran A. J. O'Hare, Anne M. Green, Julien Billard, Enectali Figueroa-Feliciano, and Louis E. Strigari. Readout strategies for directional dark matter detection beyond the neutrino background. *Phys. Rev.*, D92(6):063518, 2015.

[142] J. I. Read. The Local Dark Matter Density. *J. Phys.*, G41:063101, 2014.

[143] Louis E. Strigari. Galactic Searches for Dark Matter. *Phys. Rept.*, 531:1–88, 2013.

[144] Yao-Yuan Mao, Louis E. Strigari, Risa H. Wechsler, Hao-Yi Wu, and Oliver Hahn. Halo-to-Halo Similarity and Scatter in the Velocity Distribution of Dark Matter. *Astrophys. J.*, 764:35, 2013.

[145] Yao-Yuan Mao, Louis E. Strigari, and Risa H. Wechsler. Connecting Direct Dark Matter Detection Experiments to Cosmologically Motivated Halo Models. *Phys. Rev.*, D89(6):063513, 2014.

[146] Til Piffl et al. The RAVE survey: the Galactic escape speed and the mass of the Milky Way. *Astron. Astrophys.*, 562:A91, 2014.

[147] Riccardo Catena. Analysis of the theoretical bias in dark matter direct detection. *JCAP*, 1409(09):049, 2014.

[148] Riccardo Catena and Paolo Gondolo. Global limits and interference patterns in dark matter direct detection. *JCAP*, 1508(08):022, 2015.

[149] K. Schneck et al. Dark matter effective field theory scattering in direct detection experiments. *Phys. Rev.*, D91(9):092004, 2015.

[150] Prateek Agrawal, Zackaria Chacko, Can Kilic, and Rashmish K. Mishra. A Classification of Dark Matter Candidates with Primarily Spin-Dependent Interactions with Matter. 2010.

[151] Keith R. Dienes, Jason Kumar, Brooks Thomas, and David Yaylali. Overcoming Velocity Suppression in Dark-Matter Direct-Detection Experiments. *Phys. Rev.*, D90(1):015012, 2014.

[152] Richard J. Hill and Mikhail P. Solon. Standard Model anatomy of WIMP dark matter direct detection II: QCD analysis and hadronic matrix elements. *Phys. Rev.*, D91:043505, 2015.

[153] Martin Hoferichter, Philipp Klos, and Achim Schwenk. Chiral power counting of one- and two-body currents in direct detection of dark matter. *Phys. Lett.*, B746:410–416, 2015.

[154] Daniel Z. Freedman. Coherent neutrino nucleus scattering as a probe of the weak neutral current. *Phys. Rev.*, D9:1389–1392, 1974.

[155] Bhaskar Dutta, Rupak Mahapatra, Louis E. Strigari, and Joel W. Walker. Sensitivity to Z-prime and nonstandard neutrino interactions from ultralow threshold neutrino-nucleus coherent scattering. *Phys. Rev.*, D93(1):013015, 2016.

[156] W. C. Haxton, R. G. Hamish Robertson, and Aldo M. Serenelli. Solar Neutrinos: Status and Prospects. *Ann. Rev. Astron. Astrophys.*, 51:21–61, 2013.

[157] Christopher Savage, Andre Scaffidi, Martin White, and Anthony G. Williams. LUX likelihood and limits on spin-independent and spin-dependent WIMP couplings with LUXCalc. *Phys. Rev.*, D92(10):103519, 2015.

[158] Keith R. Dienes, Jason Kumar, Brooks Thomas, and David Yaylali. Overcoming Velocity Suppression in Dark-Matter Direct-Detection Experiments. *Phys. Rev.*, D90(1):015012, 2014.

[159] Jonathan L. Feng, Jason Kumar, and David Sanford. Xenophobic Dark Matter. *Phys. Rev.*, D88(1):015021, 2013.

APPENDIX A

VECTOR DARK MATTER EFT

If the WIMP has spin 1, we find two extra operators that haven't been considered previously. Specifically, the operators depend on the symmetric combination of polarization vectors, $S_{ij} = \frac{1}{2}\left(\epsilon_i^\dagger \epsilon_j + \epsilon_j^\dagger \epsilon_i\right)$. This necessitates a modification to the WIMP response functions by first modifying the ℓ coefficients given in Eq. 3.13. Based on our non-relativistic reduction for vector dark matter, the Lagrangian for vector dark matter and the nucleus, interacting via an uncharged scalar or vector mediator can be written in general as:

$$\begin{aligned}\mathcal{L}_{vector} &= c_1\mathcal{O}_1 + c_4\mathcal{O}_4 + c_5\mathcal{O}_5 + c_8\mathcal{O}_8 + c_9\mathcal{O}_9 + c_{10}\mathcal{O}_{10} + c_{11}\mathcal{O}_{11} \\ &\quad + c_{14}\mathcal{O}_{14} + c_{17}\mathcal{O}_{17} + c_{18}\mathcal{O}_{18}\end{aligned} \tag{A.1}$$

where we've defined $\mathcal{O}_{17} \equiv \frac{i\vec{q}}{m_N}\cdot\mathcal{S}\cdot\vec{v}_\perp$ and $\mathcal{O}_{18} \equiv \frac{i\vec{q}}{m_N}\cdot\mathcal{S}\cdot\vec{S}_N$ and the c_i's are given in table 3.4. To decompose these new operators we replace $\vec{v}^\perp$ with the target velocity and the internucleon velocities and sum over nucleons. $\mathcal{O}_{17}$ can then be put into the form

$$\mathcal{O}_{17} \to \frac{i\vec{q}}{m_N}.\mathcal{S}.\left[\vec{v}_T^\perp e^{-i\vec{q}.\vec{x}_i} - \sum_{i=1}^{A}\frac{1}{2M}\left(-\frac{1}{i}\overleftarrow{\nabla}_i e^{-i\vec{q}\cdot\vec{x}_i} + e^{-i\vec{q}\cdot\vec{x}_i}\frac{1}{i}\overrightarrow{\nabla}_i\right)_{int}\right]. \tag{A.2}$$

$\mathcal{O}_{18}$ can be expanded as

$$\mathcal{O}_{18} \to \frac{1}{2}\frac{i\vec{q}}{m_N}\cdot\mathcal{S}\cdot\vec{\sigma} \tag{A.3}$$

Together, all the terms of $\mathcal{L}_{vector}$ give rise to the following ℓ factors from Eq. 3.13,

$$\begin{aligned}
\ell_0^\tau &= c_1^\tau + i\left(\tfrac{\vec{q}}{m_N}\times\vec{v}_T^\perp\right)\cdot\vec{S}_\chi c_5^\tau + (\vec{v}_T^\perp\cdot\vec{S}_\chi)c_8^\tau + i\left(\tfrac{\vec{q}}{m_N}\cdot\vec{S}_\chi\right)c_{11}^\tau + i\left(\tfrac{\vec{q}}{m_N}\cdot\mathcal{S}\cdot\vec{v}_\perp^T\right)c_{17}^\tau \\
l_0^{A\tau} &= -i\left(\frac{\vec{q}}{2m_N}\cdot\vec{S}_\chi\right)c_{14}^\tau \\
\vec{l}_E^\tau &= 0 \\
\vec{l}_M^\tau &= i\left(\frac{\vec{q}}{m_N}\times\vec{S}_\chi\right)c_5^\tau - \vec{S}_\chi c_8^\tau - i\left(\frac{\vec{q}}{m_N}\cdot\mathcal{S}\right)c_{17}^\tau \\
\vec{l}_5^\tau &= \tfrac{1}{2}\vec{S}_\chi c_4^\tau + i\left(\tfrac{\vec{q}}{m_N}\times\vec{S}_\chi\right)c_9^\tau + \tfrac{1}{2}\left(i\tfrac{\vec{q}}{m_N}\right)c_{10}^\tau + \tfrac{1}{2}\vec{v}_T^\perp\left(\tfrac{\vec{q}}{2m_N}\cdot\vec{S}_\chi\right)c_{14}^\tau + \tfrac{1}{2}\left(i\tfrac{\vec{q}}{m_N}\cdot\mathcal{S}\right)c_{18}^\tau
\end{aligned} \tag{A.4}$$

Based on the ℓ's above, the coefficients of the various nuclear responses are found by squaring the amplitude and then summing over spins. To simplify calculations, we choose a convenient basis for polarization vectors, $\epsilon_i^s = \delta_i^s$. Recall that the spin can then be written as the anti-symmetric combination $iS_k = \epsilon_{ijk}\epsilon_i^\dagger\epsilon_j$. The WIMP

responses unique to the vector case are then given by:

$$
\begin{aligned}
R_M^{\tau\tau'} &= c_1^\tau c_1^{\tau'} + \frac{2}{3}\left(\frac{\vec{q}^2}{m_N^2} v_T^{\perp 2} c_5^\tau c_5^{\tau'} + v_T^{\perp 2} c_8^\tau c_8^{\tau'} + \frac{q^2}{m_N^2} c_{11}^\tau c_{11}^{\tau'} + \frac{q^2 v_T^{\perp 2}}{4m_N^2} c_{17}^\tau c_{17}^{\tau'}\right) \\
R_{\Phi''}^{\tau\tau'} &= 0 \\
R_{\Phi'' M}^{\tau\tau'} &= 0 \\
R_{\tilde{\Phi}'}^{\tau\tau'} &= 0 \\
R_{\Sigma''}^{\tau\tau'} &= \frac{1}{6} c_4^\tau c_4^{\tau'} + \frac{q^2}{4m_N^2} c_{10}^\tau c_{10}^{\tau'} + \frac{q^2}{12m_N^2} c_{18}^\tau c_{18}^{\tau'} \\
R_{\Sigma'}^{\tau\tau'} &= \frac{1}{6} c_4^\tau c_4^{\tau'} + \frac{q^2}{6m_N^2} c_9^\tau c_9^{\tau'} + \frac{q^2 v_T^{\perp 2}}{2m_N^2} c_{14}^\tau c_{14}^{\tau'} + \frac{q^2}{24m_N^2} c_{18}^\tau c_{18}^{\tau'} \\
R_{\Delta}^{\tau\tau'} &= \frac{2}{3}\left(\frac{\vec{q}^2}{m_N^2} c_5^\tau c_5^{\tau'} + c_8^\tau c_8^{\tau'}\right) + \frac{q^2}{6m_N^2} c_{17}^\tau c_{17}^{\tau'} \\
R_{\Delta\Sigma'}^{\tau\tau'} &= \frac{2}{3}\left(c_5^\tau c_4^{\tau'} - c_8^\tau c_9^{\tau'}\right). \qquad \text{(A.5)}
\end{aligned}
$$

APPENDIX B

NON-RELATIVISTIC REDUCTIONS

We find effective relativistic interaction Lagrangians by integrating out heavy mediators. We only keep the leading order interactions (suppressed by m or m^2). To the right of each operator is their non-relativistic reduction expressed in terms of the operators in table 5.1 with the coefficient derived from the Lagrangian parameters along with the relevant nucleon form factor. As multiple operators can have the same non-relativistic limit, it is important to include the nucleon form factor at the relativistic level. If this is not performed, erroneous cancellations can occur.

For free spinors we use the Bjorken and Drell normalization and γ matrix conventions. In the non-relativistic limit we make the following replacements:

$$\begin{aligned} S &\rightarrow \frac{1_S}{\sqrt{m_S}} \\ X_\mu &\rightarrow \frac{\epsilon^s_\mu}{\sqrt{m_X}} \\ \chi &\rightarrow \sqrt{\frac{E+m_\chi}{2m_\chi}} \begin{pmatrix} \xi \\ \frac{\vec{\sigma}\cdot\vec{p}}{E+m_\chi}\xi \end{pmatrix} \end{aligned} \tag{B.1}$$

where $s = 1, 2, 3$ are the different polarization states of the vector. $\xi = (1\ 0)^T$ is the left handed Weyl spinor. The following Fierz transformation and gamma matrix identites were useful in the charged mediator cases, (a sign difference was found in the final identity when compared with [150]):

$$\begin{aligned} (\bar{q}\chi)(\bar{\chi}q) = & -\tfrac{1}{4}\left[\bar{q}q\bar{\chi}\chi+\bar{q}\gamma^\mu q\bar{\chi}\gamma_\mu\chi+\tfrac{1}{2}\bar{q}\sigma^{\mu\nu}q\bar{\chi}\sigma_{\mu\nu}\chi-\bar{q}\gamma^\mu\gamma^5 q\bar{\chi}\gamma_\mu\gamma^5\chi+\bar{q}\gamma^5 q\bar{\chi}\gamma^5\chi\right] \\ (\bar{q}\gamma^5\chi)(\bar{\chi}\gamma^5 q) = & -\tfrac{1}{4}\left[\bar{q}q\bar{\chi}\chi+\bar{q}\gamma^5 q\bar{\chi}\gamma^5\chi-\bar{q}\gamma^\mu q\bar{\chi}\gamma_\mu\chi+\bar{q}\gamma^\mu\gamma^5 q\bar{\chi}\gamma_\mu\gamma^5\chi+\tfrac{1}{2}\bar{q}\sigma^{\mu\nu}q\bar{\chi}\sigma_{\mu\nu}\chi\right] \\ (\bar{q}\chi)(\bar{\chi}\gamma^5 q) = & -\tfrac{1}{4}\left[\bar{q}q\bar{\chi}\gamma^5\chi+\bar{q}\gamma^5 q\bar{\chi}\chi-\bar{q}\gamma^\mu q\bar{\chi}\gamma_\mu\gamma^5\chi+\bar{q}\gamma^\mu\gamma^5 q\bar{\chi}\gamma_\mu\chi+i\epsilon_{\mu\nu\alpha\beta}\bar{q}\sigma^{\mu\nu}q\bar{\chi}\sigma^{\alpha\beta}\chi\right] \\ (\bar{q}\gamma_\mu\chi)(\bar{\chi}\gamma^\mu q) = & -\left[\bar{q}q\bar{\chi}\chi-\bar{q}\gamma^5 q\bar{\chi}\gamma^5\chi-\tfrac{1}{2}\bar{q}\gamma^\mu q\bar{\chi}\gamma_\mu\chi-\tfrac{1}{2}\bar{q}\gamma^\mu\gamma^5 q\bar{\chi}\gamma_\mu\gamma^5\chi\right] \\ (\bar{q}\gamma_\mu\gamma^5\chi)(\bar{\chi}\gamma^\mu\gamma^5 q) = & -\left[-\bar{q}q\bar{\chi}\chi+\bar{q}\gamma^5 q\bar{\chi}\gamma^5\chi-\tfrac{1}{2}\bar{q}\gamma^\mu q\bar{\chi}\gamma_\mu\chi-\tfrac{1}{2}\bar{q}\gamma^\mu\gamma^5 q\bar{\chi}\gamma_\mu\gamma^5\chi\right] \\ (\bar{q}\gamma_\mu\chi)(\bar{\chi}\gamma^\mu\gamma^5 q) = & -\left[\bar{q}q\bar{\chi}\gamma^5\chi-\bar{q}\gamma^5 q\bar{\chi}\chi+\tfrac{1}{2}\bar{q}\gamma^\mu q\bar{\chi}\gamma_\mu\gamma^5\chi+\tfrac{1}{2}\bar{q}\gamma^\mu\gamma^5 q\bar{\chi}\gamma_\mu\chi\right] \end{aligned} \tag{B.2}$$

$$\sigma^\mu\nu\gamma^5 = \frac{i}{2}\epsilon^{\mu\nu\rho\sigma}\sigma_{\rho\sigma} \tag{B.3}$$

All of the following operators are collected in terms of the coefficients of the NR operators, c_i, in tables 3.2,3.3 and 3.4.

Table B.1: Non-relativistic reduction of operators for a spin-0 WIMP

Scalar Mediator		
$(S^\dagger S)(\bar{q}q)$	$\longrightarrow$	$\left(\frac{h_1^N g_1}{m_\phi^2}\right)\mathcal{O}_1$
$(S^\dagger S)(\bar{q}\gamma^5 q)$	$\longrightarrow$	$\left(\frac{h_2^N g_1}{m_\phi^2}\right)\mathcal{O}_{10}$
Vector Mediator		
$i(S^\dagger\partial_\mu S - \partial_\mu S^\dagger S)(\bar{q}\gamma^\mu q)$	$\longrightarrow$	0
$i(S^\dagger\partial_\mu S - \partial_\mu S^\dagger S)(\bar{q}\gamma^\mu\gamma^5 q)$	$\longrightarrow$	$\left(\frac{2ig_4 h_4^N}{m_G^2}\frac{m_N}{m_S}\right)\mathcal{O}_{10}$
Charged Spinor Mediator		
$(S^\dagger S)(\bar{q}q)$	$\longrightarrow$	$\frac{y_1^\dagger y_1 - y_2^\dagger y_2}{m_Q m_S} f_T^N \mathcal{O}_1$
$(S^\dagger S)(\bar{q}\gamma^5 q)$	$\longrightarrow$	$i\frac{y_2^\dagger y_1 - y_1^\dagger y_2}{m_Q m_S}\tilde{\Delta}^N\mathcal{O}_{10}$

Table B.2: Operators for a spin-$\frac{1}{2}$ WIMP via a neutral mediator

Scalar Mediator		
$\bar{\chi}\chi\bar{q}q$	$\longrightarrow$	$\left(\frac{h_1^N\lambda_1}{m_\phi^2}\right)\mathcal{O}_1$
$\bar{\chi}\chi\bar{q}\gamma^5 q$	$\longrightarrow$	$\left(\frac{h_2^N\lambda_1}{m_\phi^2}\right)\mathcal{O}_{10}$
$\bar{\chi}\gamma^5\chi\bar{q}q$	$\longrightarrow$	$\left(-\frac{h_1^N\lambda_2 m_N}{m_\phi^2 m_\chi}\right)\mathcal{O}_{11}$
$\bar{\chi}\gamma^5\chi\bar{q}\gamma^5 q$	$\longrightarrow$	$\left(\frac{h_2^N\lambda_2 m_N}{m_\phi^2 m_\chi}\right)\mathcal{O}_6$
Vector Mediator		
$\bar{\chi}\gamma^\mu\chi\bar{q}\gamma_\mu q$	$\longrightarrow$	$\left(-\frac{h_3^N\lambda_3}{m_G^2}\right)\mathcal{O}_1$
$\bar{\chi}\gamma^\mu\chi\bar{q}\gamma_\mu\gamma^5 q$	$\longrightarrow$	$\left(-\frac{2h_4^N\lambda_3}{m_G^2}\right)\left(-\mathcal{O}_7 + \frac{m_N}{m_\chi}\mathcal{O}_9\right)$
$\bar{\chi}\gamma^\mu\gamma^5\chi\bar{q}\gamma_\mu q$	$\longrightarrow$	$\left(-\frac{2h_3^N\lambda_4}{m_G^2}\right)(\mathcal{O}_8 + \mathcal{O}_9)$
$\bar{\chi}\gamma^\mu\gamma^5\chi\bar{q}\gamma_\mu\gamma^5 q$	$\longrightarrow$	$\left(\frac{4h_4^N\lambda_4}{m_G^2}\right)\mathcal{O}_4$

Table B.3: Non-relativistic reduction of operators for a spin-$\frac{1}{2}$ WIMP via a charged mediator (after using Fierz identities)

Charged Scalar Mediator		
$\bar{\chi}\chi\bar{q}q$	$\longrightarrow$	$\frac{l_2^\dagger l_2 - l_1^\dagger l_1}{4m_\Phi^2} f_{Tq}^N \mathcal{O}_1$
$\bar{\chi}\chi\bar{q}\gamma^5 q$	$\longrightarrow$	$i\frac{l_1^\dagger l_2 - l_2^\dagger l_1}{4m_\Phi^2} \Delta\tilde{q}^N \mathcal{O}_{10}$
$\bar{\chi}\gamma^5\chi\bar{q}q$	$\longrightarrow$	$i\frac{l_2^\dagger l_1 - l_1^\dagger l_2}{4m_\Phi^2} \frac{m_N}{m_\chi} f_{Tq}^N \mathcal{O}_{11}$
$\bar{\chi}\gamma^5\chi\bar{q}\gamma^5 q$	$\longrightarrow$	$\frac{l_1^\dagger l_1 - l_2^\dagger l_2}{4m_\Phi^2} \frac{m_N}{m_\chi} \Delta\tilde{q}^N \mathcal{O}_6$
$\bar{\chi}\gamma^\mu\chi\bar{q}\gamma_\mu q$	$\longrightarrow$	$-\frac{l_1^\dagger l_1 + l_2^\dagger l_2}{4m_\Phi^2} \mathcal{N}_q^N \mathcal{O}_1$
$\bar{\chi}\gamma^\mu\gamma^5\chi\bar{q}\gamma_\mu q$	$\longrightarrow$	$\frac{l_1^\dagger l_2 + l_2^\dagger l_1}{2m_\Phi^2} \mathcal{N}_q^N (\mathcal{O}_8 + \mathcal{O}_9)$
$\bar{\chi}\gamma^\mu\chi\bar{q}\gamma_\mu\gamma^5 q$	$\longrightarrow$	$\frac{l_1^\dagger l_2 + l_2^\dagger l_1}{2m_\Phi^2} \Delta_q^N (\mathcal{O}_7 - \frac{m_N}{m_\chi}\mathcal{O}_9)$
$\bar{\chi}\gamma^\mu\gamma^5\chi\bar{q}\gamma_\mu\gamma^5 q$	$\longrightarrow$	$-\frac{l_1^\dagger l_1 + l_2^\dagger l_2}{m_\Phi^2} \Delta_q^N \mathcal{O}_4$
$\bar{\chi}\sigma^{\mu\nu}\chi\bar{q}\sigma_{\mu\nu}q$	$\longrightarrow$	$\frac{l_2^\dagger l_2 - l_1^\dagger l_1}{m_\Phi^2} \delta_q^N \mathcal{O}_4$
$\epsilon_{\mu\nu\alpha\beta}\bar{\chi}\sigma^{\mu\nu}\chi\bar{q}\sigma^{\alpha\beta}q$	$\longrightarrow$	$\frac{l_2^\dagger l_1 - l_1^\dagger l_2}{m_\Phi^2} \delta_q^N (i\mathcal{O}_{10} - i\frac{m_N}{m_\chi}\mathcal{O}_{11} + 4\mathcal{O}_{12})$
Charged Vector Mediator		
$\bar{\chi}\chi\bar{q}q$	$\longrightarrow$	$\frac{d_2^\dagger d_2 - d_1^\dagger d_1}{4m_V^2} f_{Tq}^N \mathcal{O}_1$
$\bar{\chi}\chi\bar{q}\gamma^5 q$	$\longrightarrow$	$i\frac{d_2^\dagger d_1 - d_1^\dagger d_2}{4m_V^2} \Delta\tilde{q}^N \mathcal{O}_{10}$
$\bar{\chi}\gamma^5\chi\bar{q}q$	$\longrightarrow$	$i\frac{d_2^\dagger d_1 - d_1^\dagger d_2}{4m_V^2} \frac{m_N}{m_\chi} f_{Tq}^N \mathcal{O}_{11}$
$\bar{\chi}\gamma^5\chi\bar{q}\gamma^5 q$	$\longrightarrow$	$\frac{d_2^\dagger d_2 - d_1^\dagger d_1}{4m_V^2} \frac{m_N}{m_\chi} \Delta\tilde{q}^N \mathcal{O}_6$
$\bar{\chi}\gamma^\mu\chi\bar{q}\gamma_\mu q$	$\longrightarrow$	$\frac{d_2^\dagger d_2 + d_1^\dagger d_1}{8m_V^2} \mathcal{N}_q^N \mathcal{O}_1$
$\bar{\chi}\gamma^\mu\gamma^5\chi\bar{q}\gamma_\mu q$	$\longrightarrow$	$-\frac{d_2^\dagger d_1 + d_1^\dagger d_2}{4m_V^2} \mathcal{N}_q^N (\mathcal{O}_8 + \mathcal{O}_9)$
$\bar{\chi}\gamma^\mu\chi\bar{q}\gamma_\mu\gamma^5 q$	$\longrightarrow$	$\frac{d_2^\dagger d_1 + d_1^\dagger d_2}{4m_V^2} \Delta_q^N (\mathcal{O}_7 - \frac{m_N}{m_\chi}\mathcal{O}_9)$
$\bar{\chi}\gamma^\mu\gamma^5\chi\bar{q}\gamma_\mu\gamma^5 q$	$\longrightarrow$	$-\frac{d_2^\dagger d_2 + d_1^\dagger d_1}{2m_V^2} \Delta_q^N \mathcal{O}_4$

Table B.4: Non-relativistic reduction of operators for a spin-1 WIMP

Scalar Mediator		
$X_\mu^\dagger X^\mu \bar{q} q$	$\longrightarrow$	$\left(\frac{b_1 h_1^N}{m_\phi^2}\right) \mathcal{O}_1$
$X_\mu^\dagger X^\mu \bar{q}\gamma^5 q$	$\longrightarrow$	$\left(\frac{b_1 h_2^N}{m_\phi^2}\right) \mathcal{O}_{10}$
Vector Mediator		
$(X_\nu^\dagger \partial_\mu X^\nu - \partial_\mu X_\nu^\dagger X^\nu)(\bar{q}\gamma^\mu q)$	$\longrightarrow$	0
$(X_\nu^\dagger \partial_\mu X^\nu - \partial_\mu X_\nu^\dagger X^\nu)(\bar{q}\gamma^\mu\gamma^5 q)$	$\longrightarrow$	$\left(\frac{-3b_5 h_4^N}{m_G^2}\frac{m_N}{m_X}\right) \mathcal{O}_{10}$
$\partial_\nu(X^{\nu\dagger} X_\mu + X_\mu^\dagger X^\nu)(\bar{q}\gamma^\mu q)$	$\longrightarrow$	$\left(\frac{\mathrm{Re}(b_6) h_3^N}{m_G^2}\frac{m_N}{m_X}\right) (\mathcal{O}_5 + \mathcal{O}_6 - \frac{q^2}{m_N^2}\mathcal{O}_4)$
$\partial_\nu(X^{\nu\dagger} X_\mu + X_\mu^\dagger X^\nu)(\bar{q}\gamma^\mu\gamma^5 q)$	$\longrightarrow$	$\left(-\frac{2\mathrm{Re}(b_6) h_4^N}{m_G^2}\frac{m_N}{m_X}\right) \mathcal{O}_9$
$\partial_\nu(X^{\nu\dagger} X_\mu - X_\mu^\dagger X^\nu)(\bar{q}\gamma^\mu q)$	$\longrightarrow$	$\left(-\frac{4\mathrm{Im}(b_6) h_3^N}{m_G^2}\frac{m_N}{m_X}\right) \mathcal{O}_{17}$
$\partial_\nu(X^{\nu\dagger} X_\mu - X_\mu^\dagger X^\nu)(\bar{q}\gamma^\mu\gamma^5 q)$	$\longrightarrow$	$\left(\frac{4\mathrm{Im}(b_6) h_4^N}{m_G^2}\frac{m_N}{m_X}\right) \mathcal{O}_{18}$
$\epsilon_{\mu\nu\rho\sigma}\left(X^{\nu\dagger}\partial^\rho X^\sigma + X^\nu \partial^\rho X^{\sigma\dagger}\right)(\bar{q}\gamma^\mu q)$	$\longrightarrow$	$\left(\frac{\mathrm{Re}(b_7) h_3^N}{m_G^2}\frac{m_N}{m_X}\right) \mathcal{O}_{11}$
$\epsilon_{\mu\nu\rho\sigma}\left(X^{\nu\dagger}\partial^\rho X^\sigma + X^\nu \partial^\rho X^{\sigma\dagger}\right)(\bar{q}\gamma^\mu\gamma^5 q)$	$\longrightarrow$	$\left(\frac{\mathrm{Re}(b_7) h_4^N}{m_G^2}\frac{m_N}{m_X}\right) (i\frac{q^2}{m_X m_N}\mathcal{O}_4 - i\frac{m_N}{m_X}\mathcal{O}_6 - 2\mathcal{O}_{14})$
$\epsilon_{\mu\nu\rho\sigma}\left(X^{\nu\dagger}\partial^\rho X^\sigma - X^\nu \partial^\rho X^{\sigma\dagger}\right)(\bar{q}\gamma^\mu q)$	$\longrightarrow$	$\left(\frac{2\mathrm{Im}(b_7) h_3^N}{m_G^2}\right) (\mathcal{O}_8 + \mathcal{O}_9)$
$\epsilon_{\mu\nu\rho\sigma}\left(X^{\nu\dagger}\partial^\rho X^\sigma - X^\nu \partial^\rho X^{\sigma\dagger}\right)(\bar{q}\gamma^\mu\gamma^5 q)$	$\longrightarrow$	$\left(\frac{4\mathrm{Im}(b_7) h_4^N}{m_G^2}\right) \mathcal{O}_4$
Charged Spinor Mediator		
$(X_\mu^\dagger X_\nu)(\bar{q}\gamma^\mu\gamma^\nu q)$	$\longrightarrow$	$\left(\frac{y_3^\dagger y_3 - y_4^\dagger y_4}{m_Q m_X}\right) \left(f_{Tq}^N \mathcal{O}_1 + 2\delta_q^N \mathcal{O}_4\right)$
$(X_\mu^\dagger X_\nu)(\bar{q}\gamma^\mu\gamma^\nu\gamma^5 q)$	$\longrightarrow$	$\left(\frac{y_4^\dagger y_3 - y_3^\dagger y_4}{m_Q m_X}\right) (i\Delta_{\tilde{q}}^N \mathcal{O}_{10} + i\delta_q^N \mathcal{O}_{11} - 2i\delta_q^N \mathcal{O}_{12} - 2i\delta_q^N \mathcal{O}_{18})$

APPENDIX C

QUARKS TO NUCLEONS

To go from the fundamental interactions of WIMPs with quarks to scattering from point-like nucleons, one must evaluate the quark (parton) bilinears in the nucleons. For a full discussion see the appendix of [150] and [158]. We write the nucleon couplings in terms of the quark couplings times a form factor (in the limit of zero momentum transfer): The scalar bilinear for light quarks can be evaluated from

$$\begin{array}{lcl} \langle N_o|\, m_q\bar{q}q\,|N_i\rangle & \longrightarrow & f_{Tq}^N \bar{N}N \\ \langle N_o|\, \bar{q}\gamma^5 q\,|N_i\rangle & \longrightarrow & \Delta\tilde{q}^N \bar{N}\gamma^5 N \\ \langle N_o|\, \bar{q}\gamma^\mu q\,|N_i\rangle & \longrightarrow & \mathcal{N}_q^N \bar{N}\gamma^\mu N \\ \langle N_o|\, \bar{q}\gamma^\mu\gamma^5 q\,|N_i\rangle & \longrightarrow & \Delta_q^N \bar{N}\gamma^\mu\gamma^5 N \\ \langle N_o|\, \bar{q}\sigma^{\mu\nu} q\,|N_i\rangle & \longrightarrow & \delta_q^N \bar{N}\sigma^{\mu\nu} N \end{array}$$

$$\langle N|\, m_q\bar{q}q\,|N\rangle = m_N f_{Tq}^N \tag{C.1}$$

while for the heavy quarks

$$\langle N|\, m_q\bar{q}q\,|N\rangle = \frac{2}{27} m_N F_{TG}^N = \frac{2}{27} m_N \left(1 - \sum_{q=u,d,s} f_{Tq}^N\right). \tag{C.2}$$

Summing over all the quarks one finds

$$h_1^N = \sum_{q=u,d,s} h_1^q \frac{m_N}{m_q} f_{Tq}^N + \frac{2}{27} f_{TG}^N \sum_{q=c,b,t} h_1^q \frac{m_N}{m_q} \tag{C.3}$$

The psuedo-scalar bilinear was recently revisited in [158]:

$$h_2^N = \sum_{q=u,d,s} h_2^q \Delta\tilde{q}^N - \Delta\tilde{G}^N \sum_{q=c,b,t} \frac{h_2^q}{m_q} \tag{C.4}$$

The vector bilinear essentially gives the number operator:

$$h_3^N = \begin{cases} 2h_3^u + h_3^d & N = p \\ h_3^u + 2h_3^d & N = u \end{cases} \tag{C.5}$$

The psuedo-vector bilinear counts the contributions of spin to the nucleon (note that sometimes this coupling has a G_F factored out to make it dimensionless)

$$h_4^N = \sum_{q=u,d,s} h_4^q \Delta_q^N \tag{C.6}$$

Throughout this paper the following values are used (it should be noted that there

are large uncertainties in these values) [150, 158]:

$$\begin{aligned}
f^n_{Tu} = &\quad 0.014 & f^p_{Tu} = 0.02 \\
f^n_{Td} = &\quad 0.036 & f^p_{Td} = 0.026 \\
f^n_{Ts} = &\quad 0.118 & f^p_{Ts} = 0.118 \\
\Delta^n_u = &\quad -0.427 & \Delta^p_u = 0.842 \\
\Delta^n_d = &\quad 0.842 & \Delta^p_d = -0.427 \\
\Delta^n_s = &\quad -0.085 & \Delta^p_s = -0.085 \\
\Delta\tilde{u}^n = &\quad -108.03 & \Delta\tilde{u}^p = 110.55 \\
\Delta\tilde{d}^n = &\quad 108.60 & \Delta\tilde{d}^p = -107.17 \\
\Delta\tilde{s}^n = &\quad -0.57 & \Delta\tilde{s}^p = -3.37 \\
\Delta\tilde{G}^n = &\quad 35.7\text{MeV} & \Delta\tilde{G}^p = 395.2\text{MeV}
\end{aligned} \tag{C.7}$$

Assuming a universal coupling of the mediators to all quarks, the nucleon level couplings are can be written as,

$$\begin{aligned}
h^N_1 = &\quad f^N_T h_1 \\
h^N_2 = &\quad \tilde{\Delta}^N h_2 \\
h^N_3 = &\quad \mathcal{N}^N h_3 \\
h^N_4 = &\quad \Delta^N h_4
\end{aligned} \tag{C.8}$$

where we have defined,

$$\begin{aligned}
f^n_T = &\quad 11.93 & f^p_T = 12.31 \\
\tilde{\Delta}^n = &\quad -0.07 & \tilde{\Delta}^p = -0.28 \\
\mathcal{N}^n = &\quad 3 & \mathcal{N}^p = 3 \\
\Delta^n = &\quad 0.33 & \Delta^p = 0.33 \\
\delta^n = &\quad 0.564 & \delta^p = 0.564 \\
&\quad . &
\end{aligned} \tag{C.9}$$

This introduces a small amount of isospin violation, and it is known that relaxing the assumption of universal couplings to quarks can lead to interesting isospin violating effects [158, 159].

APPENDIX D

NEUTRINO FLOOR ANALYSIS FOR ALL OPERATORS

In this appendix, we show best fitting masses and discovery limits for the operators that were not shown in the main text. These figures motivate the operator groupings that were presented above. Figure D.1 show the best fit masses to the ^{8}B neutrino rate for the four targets. Figure D.2 shows the discovery evolution for the low mass and high mass WIMP region for operators $\mathcal{O}_3 - \mathcal{O}_9$, and Figure D.2 shows the discovery evolution for the low mass and high mass WIMP region for operators $\mathcal{O}_{11} - \mathcal{O}_{15}$. Figure D.6 shows the discovery limits for group 2 operators interacting with protons, and Figure D.7 shows the discovery limits for group 2 operators interacting with neutrons. Finally, Figure D.8 shows the discovery limits for group 2 operators interacting with protons, and Figure D.9 shows the discovery limits for group 2 operators interacting with neutrons.

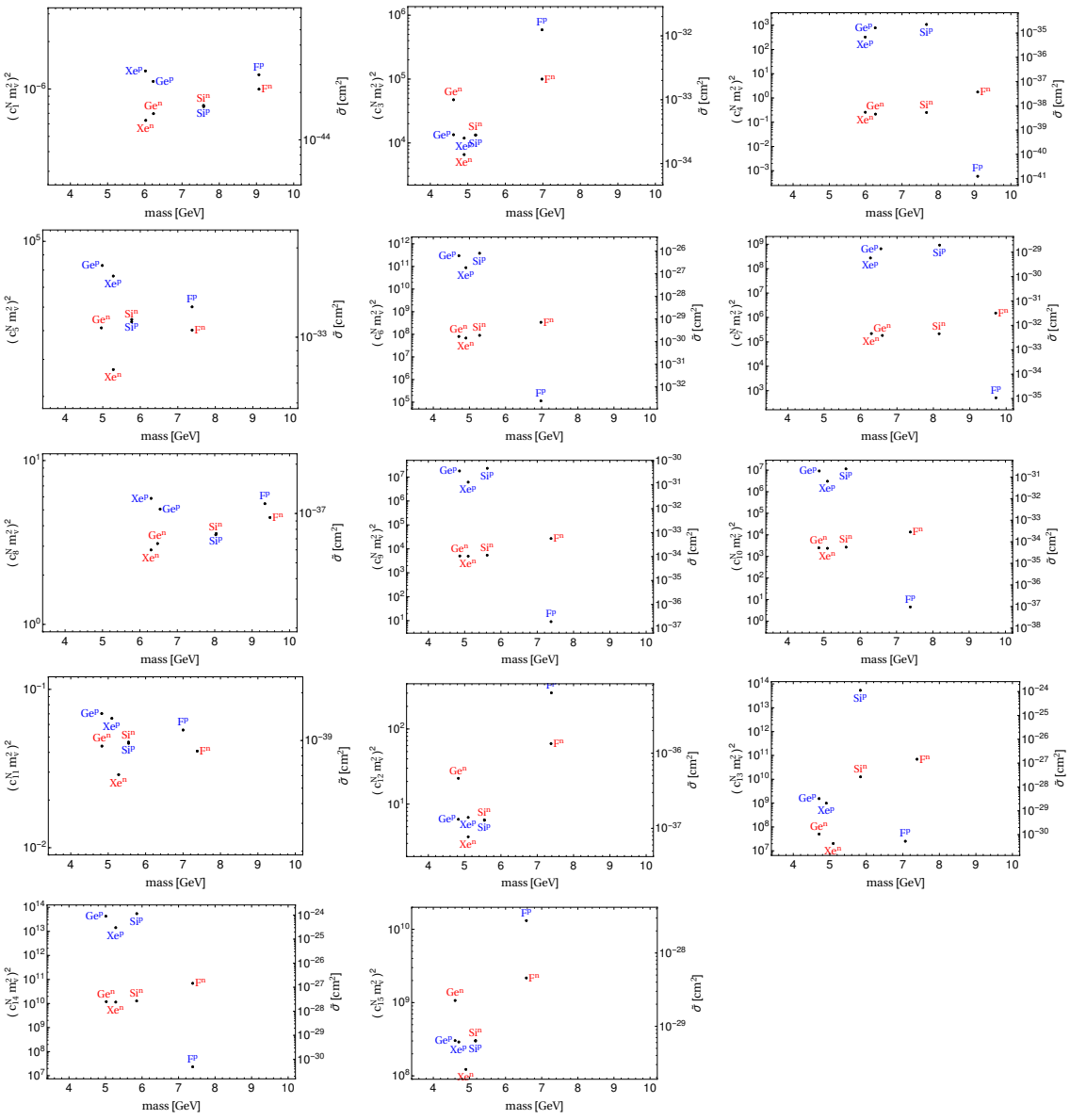

Figure D.1: Best fits of each operator to the ^{8}B Solar neutrino rate for the four targets

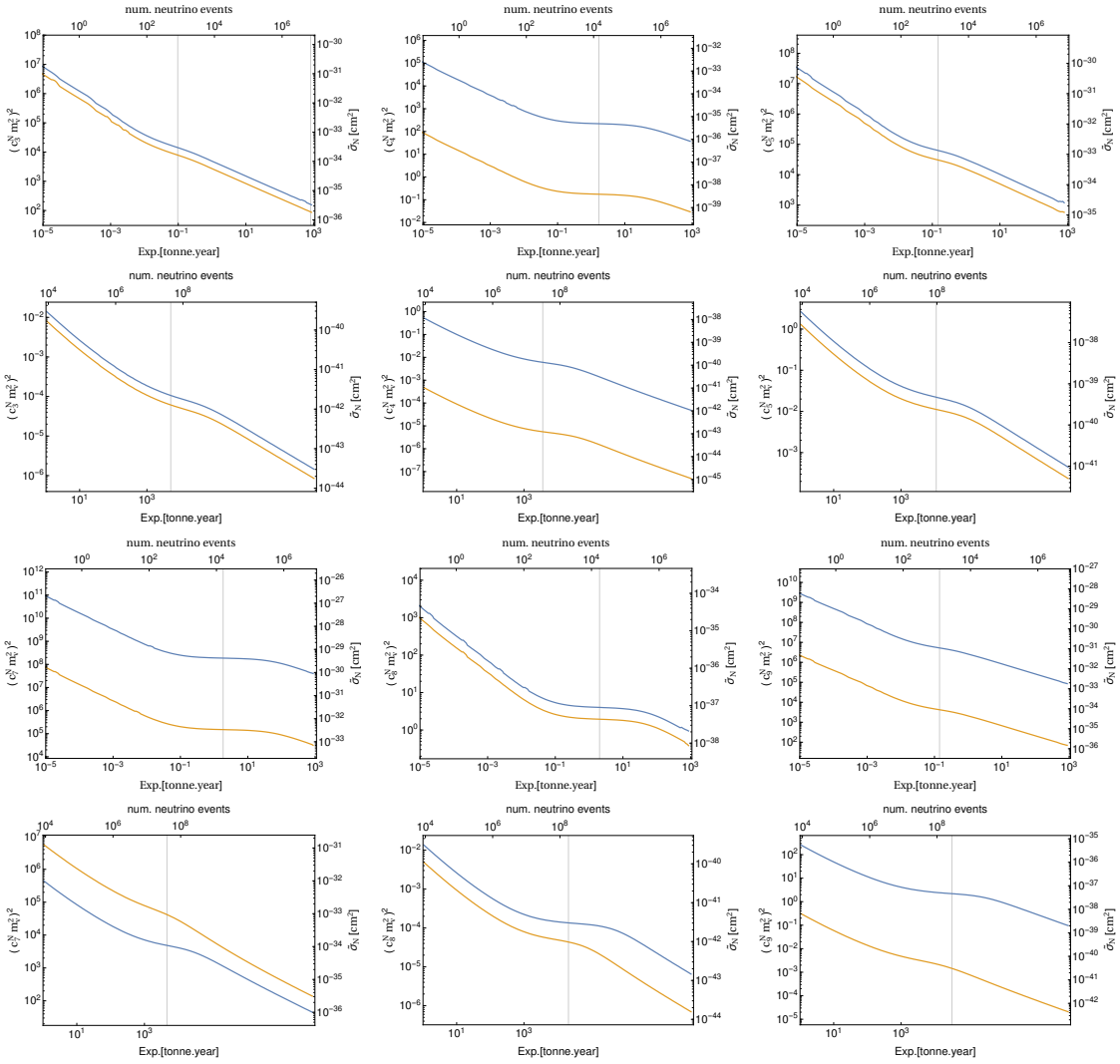

Figure D.2: Discovery evolution for the low mass region (first and third rows) and high mass region (second and fourth rows) for operators 3-9. The blue and yellow curves show the limits for proton and neutron scattering, respectively

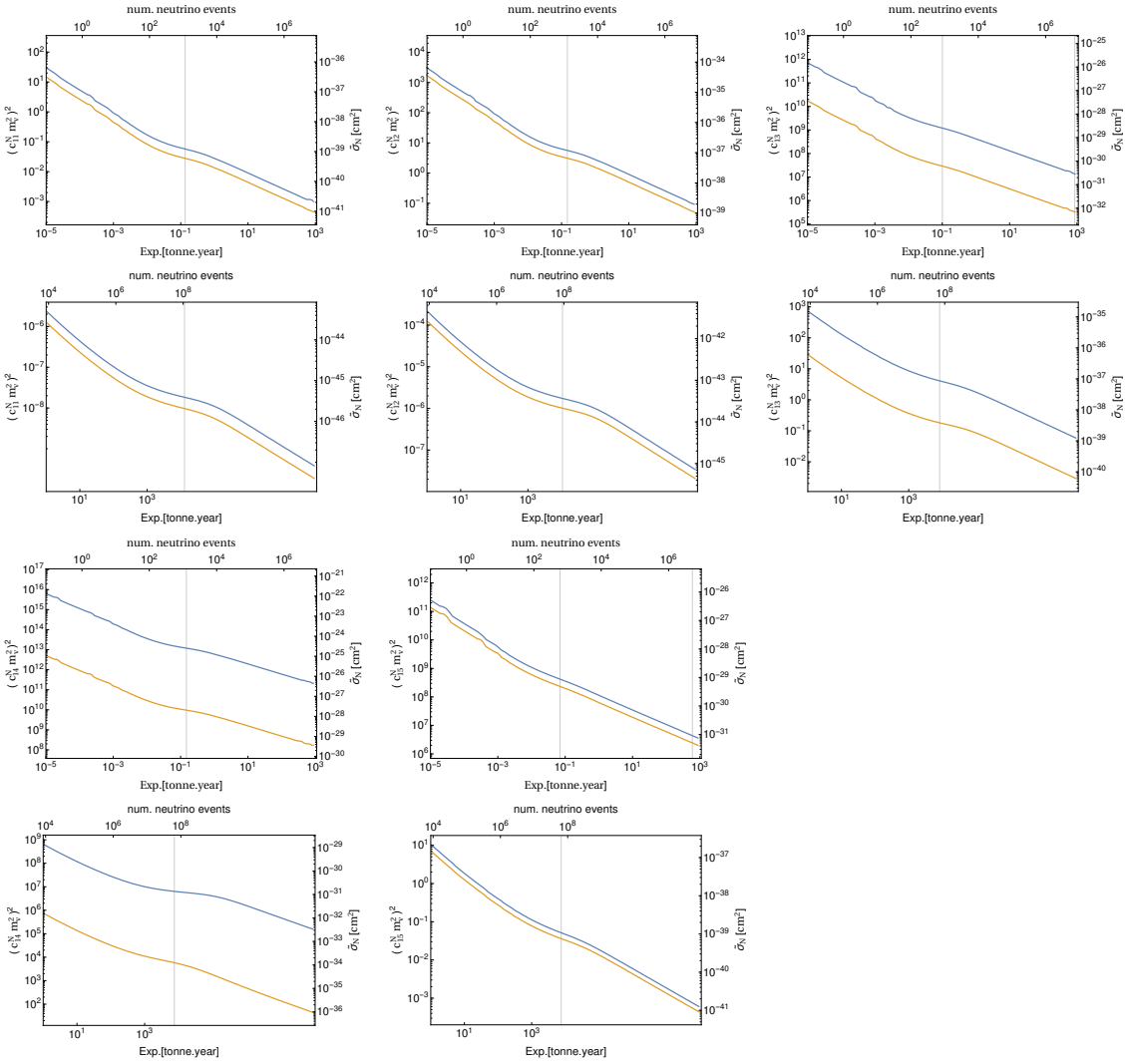

Figure D.3: Discovery evolution for the low mass region (first and third rows) and high mass region (second and fourth rows) for operators 11-15. The blue and yellow curves show the limits for proton and neutron scattering, respectively

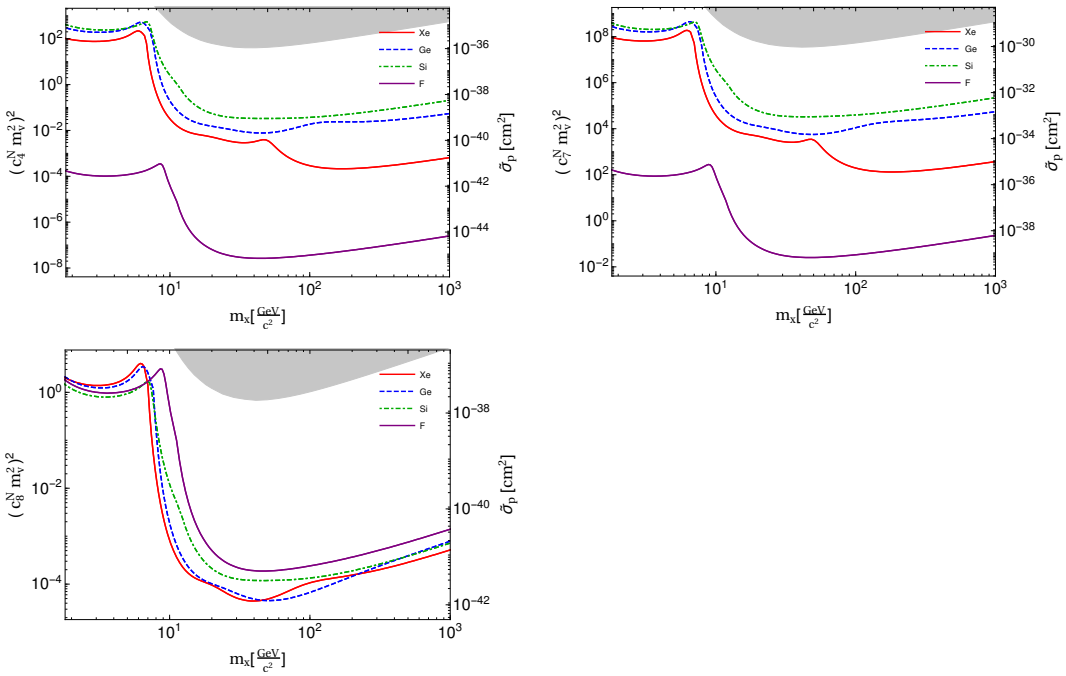

Figure D.4: Discovery limits for group 1 operators interacting with protons

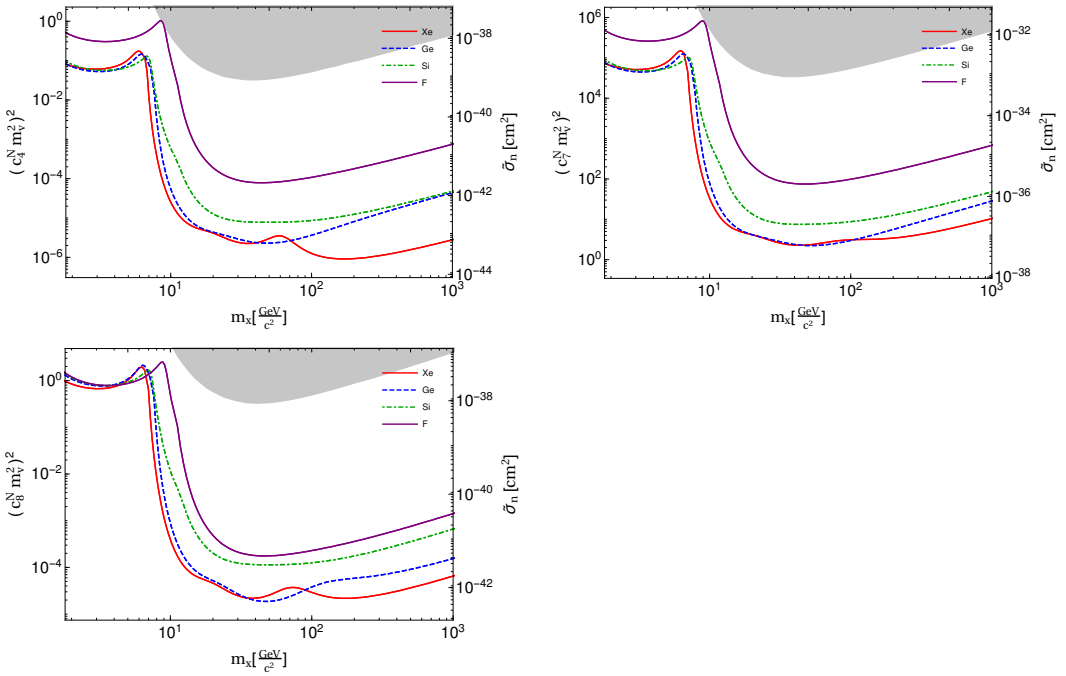

Figure D.5: Discovery limits for group 1 operators interacting with neutrons

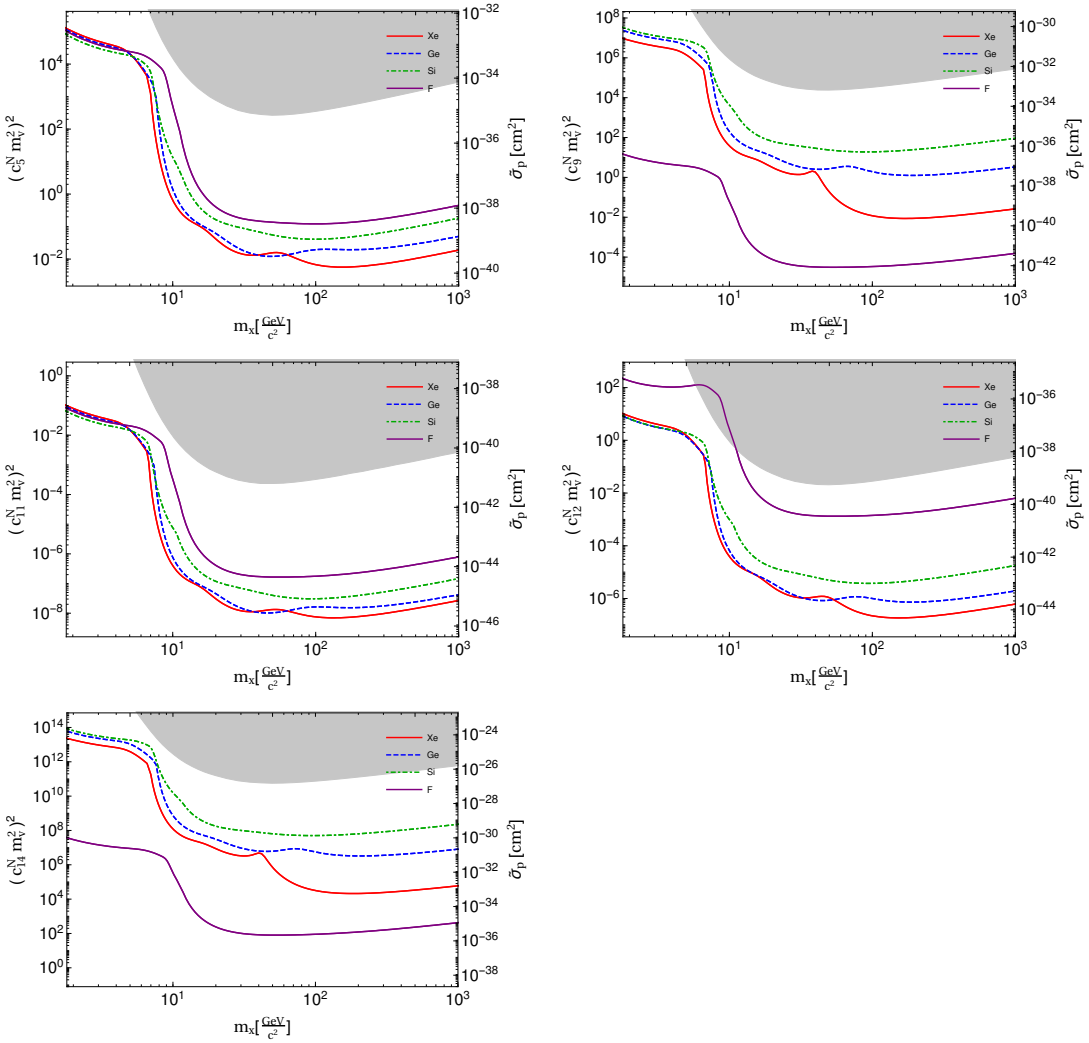

Figure D.6: Discovery limits for group 2 operators interacting with protons

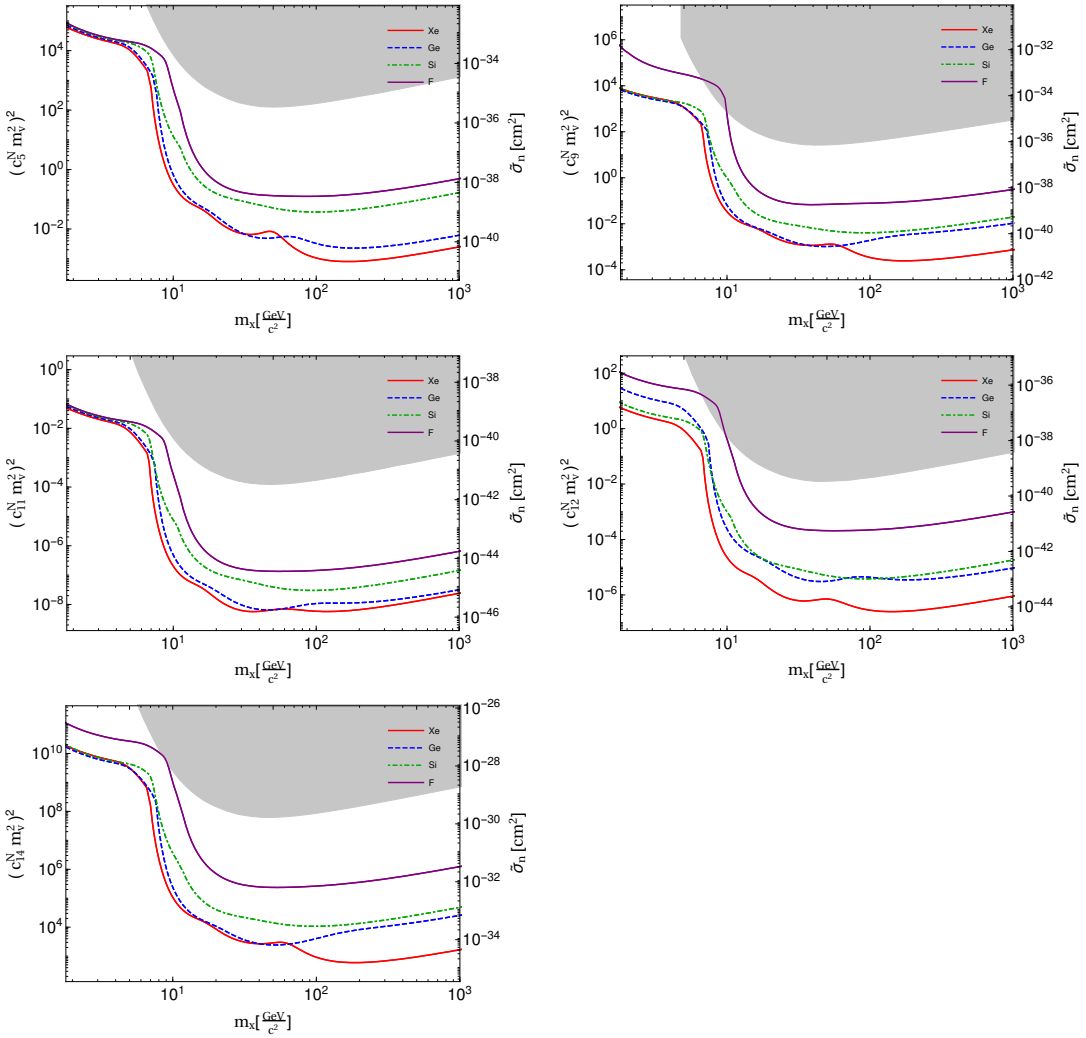

Figure D.7: Discovery limits for group 2 operators interacting with neutrons

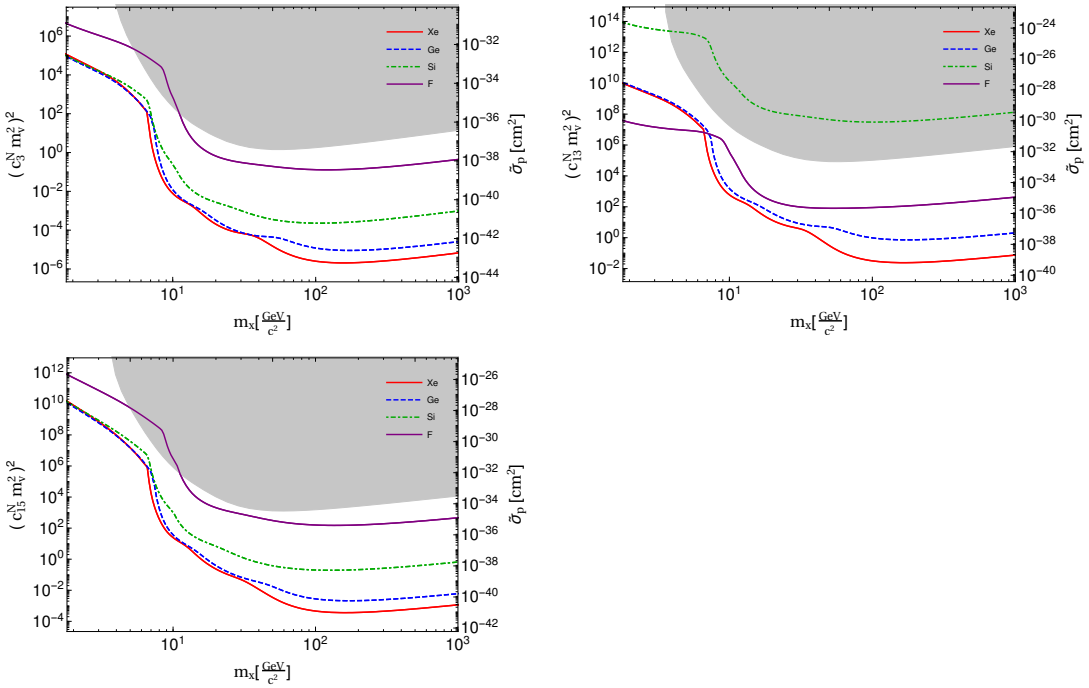

Figure D.8: Discovery limits for group 3 operators interacting with protons

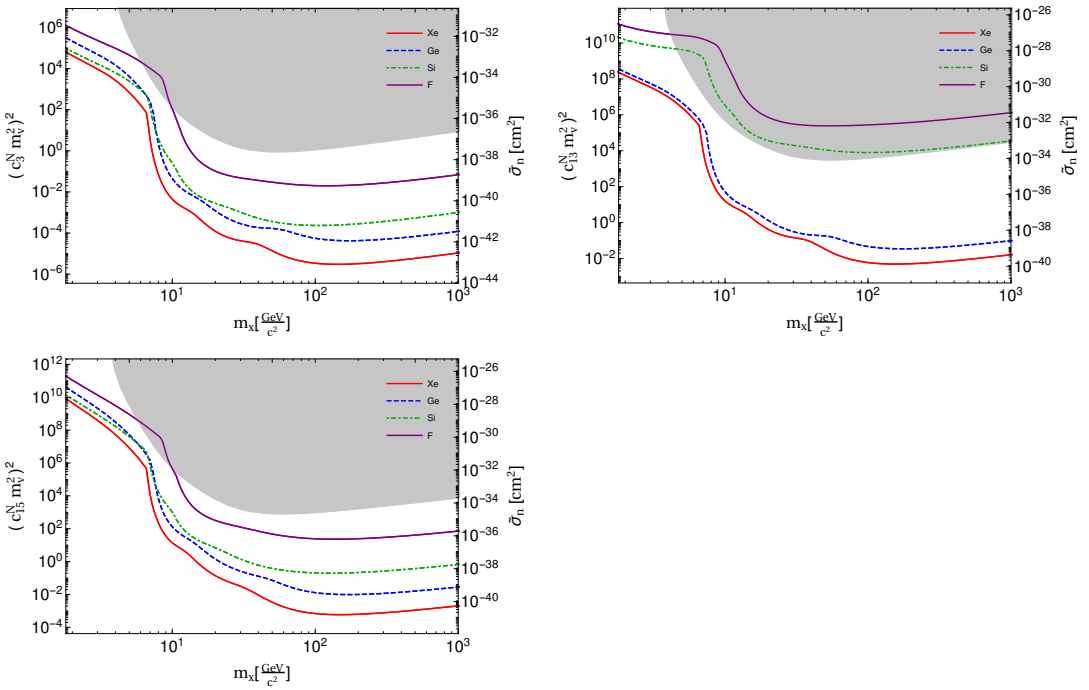

Figure D.9: Discovery limits for group 3 operators interacting with neutrons.

APPENDIX E

CO-AUTHOR PERMISSION STATEMENT

Chapters 2, 3 and 5 were based on the published works [17] [19] and [20], respectively. The listed co-authors each provided permission to include the works in this dissertation: L. M. Krauss, J. B. Dent, T. D. Jacques, F. Ferrer, S. Sabharwal, L. E. Strigari and B. Dutta.